# Design of Osteoinductive Bone Substitutes for Skeletal Site-Specific Healing

By

Lauren Boller Davis

Dissertation

Submitted to the Faculty of the

Graduate School of Vanderbilt University

in partial fulfillment of the requirements

for the degree of

DOCTOR OF PHILOSOPHY

in

Biomedical Engineering

May 14, 2021

Nashville, Tennessee

Approved:

Scott A. Guelcher, Ph.D.

Craig L. Duvall, Ph.D.

Cynthia Reinhart-King, Ph.D.

Jonathan G. Schoenecker, M.D., Ph.D.

Rachelle W. Johnson, Ph.D.

# DEDICATION

Dedicated to my husband, Blaine, who has always encouraged me to fearlessly go after my goals, no matter how crazy they may seem.

To my parents, Bob and Carol, who consistently demonstrated what hard work looked like and who managed to make life a whole lot of fun along the way.

To my dog, Jack, whose ability to turn a bad day into a good one and never-failing love are truly unmatched. There is no one I would rather spend the bulk of my graduate stipend on.

ACKNOWLEDGEMENTS

I do not have the words to properly thank my advisor, Dr. Scott Guelcher. His guidance, patience, and support throughout the past five years has been invaluable and have made me a better researcher, student, and person. I am grateful for all of our research discussions along with the opportunities that he afforded me including the opportunity to work on translational projects with industry collaborators and the opportunity to travel to both domestic and international conferences to share my research. Furthermore, I am grateful for his long-term support of my career goals outside of academia.

I would also like to thank my research committee, Dr. Cindy Reinhart-King, Dr. Craig Duvall, Dr. Rachelle Johnson, and Dr. Jonathan Schoenecker. I am grateful for all of your insight and guidance. Thank you for asking me the right questions and challenging me to think more critically.

I am so grateful for the members of the Guelcher lab that played an integral role in my time here at Vanderbilt. I would like to thank Katarzyna (Kasia) Zienkiewicz who made my time in the Guelcher lab run smoothly. Her guidance and assistance in material preparation and histology was invaluable. She served not only as a great mentor, but a great friend and role model. Her hard work and tenacity in solving problems consistently motivated me. Furthermore, her kindness and generosity towards myself and all of the students did not go unnoticed. Thank you to the Guelcher lab peers who completed their PhDs during my time in the Guelcher lab and helped me to problem solve and trouble shoot including Dr. Sichang Lu, Dr. Madison McGough, Dr. Joe Vanderburgh, and Dr. Tom Spoonmore. I am grateful for all of your guidance and friendship along the way. I would also like to thank the current students in the Guelcher lab including Greg Lowen, David Florian, and Taylor Scott for all of their help and support in and out of the lab. Thank you to the members of the Vanderbilt Center for Bone Biology who helped teach me new techniques and

offered valuable knowledge throughout my tenure, including Dr. Sun Peck, Sasi Uppuganti, Tony Vechii, Joshua Johnson, and Alyssa Merkel.

I would especially like to acknowledge Dr. Guelcher, Dr. Reinhart-King, Dr. Michael Savona, Kasia Zienkiewicz, Dr. Joe Vanderburgh, and David Florian for their support and assistance during my husband's Leukemia diagnosis. It is because of them that I was able to continue through with my research when I was not sure how I would be able to manage it. Their understanding, sympathy, and support was crucial to my success.

During my time at Vanderbilt, I had the opportunity to participate in the Vanderbilt Program for Molecular Medicine where I was able to focus on clinical and translational science related to my research work. Thank you to Dr. Matt Luther, Dr. Mark de Caestecker, and Faith Bishop for their work in coordinating and leading the program. Thank you to Dr. Jonathan Schoenecker for allowing me to shadow in his Pediatric Orthopaedic clinic. I learned so much about the complexities of clinical challenges and patient treatment.

Thank you to Dr. David Cochran and Dr. Archie Jones for their expertise and skills in performing our non-human primate oral maxillofacial surgeries. Thank you to Dr. Pablo Morales and the Mannheimer foundation for their hospitality and animal husbandry in our non-human primate study. Thank you to our collaborators at The United States Army Institute of Surgical Research (USAISR), Dr. Joseph Wenke and Dr. Stef Shiels for your knowledge and collaborations with our lab to carry out countless animal studies. I would also like to acknowledge Cheyenne Rhodes and Bre Jacobs at Medtronic for supporting part of this project.

I am grateful for the funding sources that supported me and this research work including the Integrated Training in Engineering and Diabetes (ITED) program (NIH T32 DK101003), the Department of Defense (Grant Nos. W81XWH-16-2-0052, W81XWH-115-0-0001), and the

Army, Navy, NIH, Air Force, VA and Health Affairs to support the AFIRM II effort (No. W81XWH-14-2-0004).

Finally, I would like to acknowledge and thank my husband, my parents, my sister, and my in-laws for all of their support and love. None of this would have been possible without them.

TABLE OF CONTENTS

LIST OF TABLES

Table Page

LIST OF FIGURES

Figure Caption Page

LIST OF ABBREVIATIONS

AG- autograft

rhBMP-2- recombinant human bone morphogenetic protein

PUR- polyurethane

nHA- nanocrystalline hydroxyapatite

PEUR- poly (ester urethane)

PTKUR- poly (thioketal urethane)

μCT- microcomputed tomography

PiT- phosphate transporter

hMSCs- human mesenchymal stem cells

MSCs- mesenchymal stem cells

VEGF- vascular endothelial growth factor

BMP- bone morphogenetic protein

HA- hydroxyapatite

PCL- poly (ϵ-caprolactone)

PLA- polylactide

PLGA- poly(lactide-co-glycolide)

PMMA- poly(methyl methacrylate)

CaP- calcium phosphate

β-TCP- Beta-tricalcium phosphate

LTI- lysine triisocyanate

FGF- fibroblast growth factor

IGF-1-insulin like growth factor

PDGF- platelet derived growth factorTGF-β – transforming growth factor -β

IHC- immunohistochemistry

BV/TV- bone volume/total volume

Tb.Th- trabecular thickening

Tb.Sp.- trabecular spacing

Tb.N.- trabecular number

CR- compression resistant

ACS- absorbable collagen sponge

PEG- polyethylene glycol

AOI- area of interest

IC- iliac crest

TK- thioketal

$LiAlH_4$- Lithium aluminum hydride

LTI-PEG- Lysine triisocyanate-polyethylene glycol NaPi- sodium phosphate

Erk1/2- extracellular regulated kinase

PCLUR- poly (ϵ-caprolactone urethane)

GAG- glycosaminoglycan

SLC20a1/PiT1- Sodium- dependent phosphate transporter 1

FGFR2- fibroblast growth factor 2

ROS- reactive oxygen species

FeAA- iron (III) acetylacetonate

Emcn- endomucin

MPO- myeloperoxidase

PTK- poly (thioketal)

ALP- alkaline phosphatase

nPPi- polyphosphate nanoparticles

# CHAPTER I

## CHAPTER 1: INTRODUCTION

Over 1.6 million bone grafting procedures are performed annually in the United States as a result of underlying illness or trauma.[1] Bone grafts are required when a defect is critical sized and is unable to spontaneously heal on its own.[2] Autograft (AG) has long been considered the gold standard for bone grafts as it is inherently osteoconductive, osteoinductive, and osteogenic.[3,4] However, complications associated with AG include donor site morbidity, limited quantity, poor vascularization, and potential failure to integrate with host bone.[5,6] Allograft, donor bone, is also frequently utilized for bone grafts, but its use is precluded by limited bioactivity and potential immune response.[7,8] To address the present shortcomings with both autograft and allograft, recombinant human bone morphogenetic protein -2 (rhBMP-2) has been utilized clinically as an osteoinductive agent to promote both the recruitment and subsequent differentiation of progenitor cells into osteoblasts. However, current rhBMP-2 delivery modalities utilize supra-physiological concentrations.[9] Additionally, FDA approval of rhBMP-2 is limited to specific anatomic sites and presents off-label side effects of swelling, ectopic bone formation, mineralization in muscle tissue, and carcinogenic risks.[10–15]

Biodegradable lysine-derived polyurethane (PUR) scaffolds have been extensively investigated for bone repair applications.[16–20] PURs breakdown through hydrolytic and cell-mediated oxidative degradation into non-toxic byproducts.[20,21] PUR scaffolds augmented with ceramic particles have shown improved mechanical properties and are osteoconductive, meaning they provide a platform for cells to proliferate and form new bone but do not directly guide osteogenesis.[8,22] However, large defects in less biologically active sites often require osteoinductive factors, factors that recruit progenitor cells and promote their differentiation into osteoblasts, which greatly limits available options.

Furthermore, bone regeneration after fracture occurs by two mechanisms: endochondral ossification and intramembranous ossification. Both of these processes begin with mesenchymal stem cells, but the process by which these cells transform into bone differs. In endochondral ossification, bone forms through a cartilage intermediate while intramembranous ossification takes place when bone forms through the direct differentiation of progenitor cells into osteoblasts. The method by which new bone forms is dependent both on anatomic site and additional factors including fracture site stability, strain, and vascularity. Additionally, bone substitutes must maintain the functionality of the specific bone in which they are used (i.e., weight bearing or non-weight bearing). These factors can vary drastically between fracture sites, thus contributing to the complexity of developing osteoinductive bone substitutes.

To overcome current limitations in available bone grafts, we developed PUR based bone substitutes that utilize various approaches to confer osteoinductivity including the incorporation of nano-ceramics like nanocrystalline hydroxyapatite (nHA) and AG. The development of and material properties of these substitutes have been extensively investigated in previous work[22–24], however little is understood about the mechanisms by which these materials promote cellular differentiation, bone formation, and remodeling. A fundamental understanding of these principles is necessary to develop bone substitutes that promote new bone formation specific to both anatomic site and application.

## 1.1 Specific Aims

The overarching goal of this research is to gain a better understanding of how osteoinductive bone substitutes affect cellular response, differentiation, and remodeling both *in vitro* and *in vivo*.

Aim I: Determine the optimal autograft extender composition to enhance bone formation and remodeling *in vivo.* AG is the gold standard of bone grafting but is limited in its availability, thus, AG extenders have been developed to increase the overall volume of AG while maintaining its osteogenic and osteoinductive properties. Poly (ester urethanes) (PEURs) and poly (thioketal urethanes) (PTKURs) have been previously utilized in bone regeneration applications, however, the effect of polymer composition on AG extenders ability to promote bone formation and remodeling has not been explored. It was hypothesized that hydrolytically degradable PEUR based AG extenders would degrade more rapidly and lead to increased bone remodeling when compare with cell degradable PTKUR AG extenders. In this aim, PEUR- and PTKUR- AG extenders were implanted into a rabbit radius model and outcomes of Microcomputed tomography (μCT), dynamic histomorphometry, and histology were analyzed at 12 weeks to evaluate bone formation and graft remodeling *in vivo*.

Aim II: Investigate the mechanistic role of nHA in promoting cellular differentiation *in vitro.* nHA composites have been extensively utilized to recapitulate the bone microenvironment in order to promote bone regeneration. Although it is widely accepted that nHA promotes osteogenic differentiation of osteoprogenitor cells, some studies have shown small amounts of nHA stimulate chondrogenic differentiation *in vitro*. Earlier work has suggested that nHA may act through phosphate transporter (PiT) activation. However, the mechanism by which cells interact with nHA dispersed in polymeric composites to determine a chondrogenic or osteogenic fate is not well understood. We hypothesized that polymer bound nHA would activate membrane-bound PiTs in a dose-dependent manner and lead to the activation of either chondrogenic or osteogenic differentiation dependent on nHA dose. *In vitro* studies evaluated the response of human mesenchymal stem cells (hMSCs) to nHA and identified a mechanism by which polymer

dispersed nHA promoted osteogenesis.

Aim III: Assess the relationship between nHA and the mechanism of bone formation *in vivo*. Recapitulating natural fracture healing *in vivo* remains a limitation in biomaterial-based bone regeneration strategies. Although fracture healing typically occurs through a combination of endochondral and intramembranous ossification, current approaches to bone regeneration typically promote intramembranous ossification through the use of osteoconductive and osteoinductive biomaterials and are not designed for the specific anatomic conditions or site at which they are being used. Little is understood about how material composition of bone substitutes influences the mechanisms by which new bone is formed *in vivo*. It was hypothesized that smaller concentrations of nHA would promote bone formation through endochondral ossification while larger concentrations of nHA would promote bone via intramembranous ossification. In this aim, nHA-PTKUR composite materials of varying nHA wt% were implanted in 2mm femoral diaphyseal and femoral metaphyseal defects in rats. μCT, histomorphometry, and immunohistochemistry were utilized to evaluate the role of nHA in bone formation *in vivo*.

## 2.2 Approach

**Chapter 1** of this work provides a brief introduction to osteoinductive polyurethanes for bone regeneration and provides justification for the undertaking of this project. **Chapter 2** provides an in-depth background on bone, its composition, and how fracture healing and remodeling occurs. An overview of bone grafts and synthetic bone substitutes is provided. A discussion on the use of polyurethanes in bone grafts and substitutes along with strategies to promote osteoinductivity in polyurethanes follows. Finally, an overview of methods used to evaluate *in vivo* outcomes of bone healing and remodeling is provided.

**Chapter 3** describes the continuation and completion of previous work in the lab and provides an assessment of clinically relevant compression resistant rhBMP-2 carriers. New bone formation and dose response was evaluated in a non-human primate mandibular model. Although this work was successful and proved that compression resistant rhBMP-2 carriers worked to promote new bone formation in a pre-clinical trial model, the challenges and nuances of gaining FDA approval for a new carrier of a biologic growth factor demonstrated the need to develop alternative osteoinductive bone substitutes and inspired the following work described in this dissertation.

To avoid the inherent risks and costs associated with a novel rhBMP-2 carrier FDA approval process, osteoinductive AG was combined with PTKUR and PEUR 'extenders' in **Chapter 4**. PTKUR-AG and PEUR-AG extenders were implanted in a rabbit radius model. µCT and histological outcomes evaluating bone formation and graft remodeling demonstrated that polymer composition did not have an effect on overall new bone formation. This chapter addresses the overall goal of determining the optimal AG extender composition for enhanced bone formation and remodeling as defined in **Aim I**.

Reduced osteoinductivity observed in polymer-embedded AG led to the use of the osteoinductive nanoceramic, nHA, for the remainder of this dissertation work. In **Chapter 5**, *in vitro* studies were performed to evaluate hMSC differentiation on nHA composites. Increasing the dose of nHA within the composites led to dose-dependent osteogenesis *in vitro*. Furthermore, the mechanism of action by which polymer-bound nHA promoted osteogenesis was confirmed thus addressing **Aim II**.

A better understanding of the role of nHA *in vitro* led to investigating the role of nHA on bone formation *in vivo*. In **Chapter 6**, nHA composites were implanted into two rat models *in*

*vivo:* the femoral diaphysis and the femoral metaphysis. The implanted scaffolds supported new bone formation in both anatomic sites. In the metaphysis, augmentation of scaffolds with nHA promoted an intramembranous healing response while nHA inhibited endochondral ossification in the diaphysis. These findings demonstrated that nHA had skeletal site-specific effects on fracture healing. In this chapter, **Aim III** of this dissertation is addressed.

**Chapter 7** summarizes the overall findings of this work while the future directions and next steps are outlined in **Chapter 8**.

References


1. O'Keefe, R. J. & Mao, J. Bone Tissue Engineering and Regeneration: From Discovery to the Clinic—An Overview. *Tissue Eng. Part B Rev.* **17**, 389–392 (2011).
2. Hollinger, J. & Kleinschmidt, J. The critical size defect as an experimental model to test bone repair materials. *J. Craniofac. Surg.* **1**, 60–68 (1990).
3. Albrektsson, T. & Johansson, C. Osteoinduction, osteoconduction and osseointegration. *Eur. Spine J.* **10**, S96–S101 (2001).
4. Shafiei, Z., Bigham, A. S., Dehghani, S. N. & Torabi Nezhad, S. Fresh cortical autograft versus fresh cortical allograft effects on experimental bone healing in rabbits: Radiological, Histopathological and Biomechanical evaluation. *Cell Tissue Bank.* **10**, 19–26 (2009).
5. Kalk, W. W. ., Raghoebar, G. M., Jansma, J. & Boering, G. Morbidity from iliac crest bone harvesting. *J. Oral Maxillofac. Surg.* **54**, 1424–1429 (1996).
6. Chim, H. & Gosain, A. K. Biomaterials in craniofacial surgery: experimental studies and clinical application. *J. Craniofac. Surg.* **20**, 29–33 (2009).
7. Aponte-Tinao, L. A., Ayerza, M. A., Muscolo, D. L. & Farfalli, G. L. What Are the Risk Factors and Management Options for Infection After Reconstruction With Massive Bone Allografts? *Clin. Orthop. Relat. Res.* (2016). doi:10.1007/s11999-015-4353-3
8. Yu, X., Tang, X., Gohil, S. V. & Laurencin, C. T. Biomaterials for Bone Regenerative Engineering. *Advanced Healthcare Materials* **4**, 1268–1285 (2015).
9. Vaibhav, B., Nilesh, P., Vikram, S. & Anshul, C. Bone morphogenic protein and its application in trauma cases: A current concept update. *Injury* (2007). doi:10.1016/j.injury.2006.12.012
10. Perri, B., Cooper, M., Lauryssen, C. & Anand, N. Adverse swelling associated with use of rh-BMP-2 in anterior cervical discectomy and fusion: a case study. *Spine J.* **7**, 235–239 (2007).
11. Tannoury, C. A. & An, H. S. Complications with the use of bone morphogenetic protein 2 (BMP-2) in spine surgery. *Spine Journal* (2014). doi:10.1016/j.spinee.2013.08.060
12. Wong, D. A., Kumar, A., Jatana, S., Ghiselli, G. & Wong, K. Neurologic impairment from ectopic bone in the lumbar canal: a potential complication of off-label PLIF/TLIF use of bone morphogenetic protein-2 (BMP-2). *Spine J.* **8**, 1011–1018 (2008).
13. Smucker, J. D., Petersen, E. B. & Fredericks, D. C. Assessment of MASTERGRAFT PUTTY as a graft extender in a rabbit posterolateral fusion model. *Spine (Phila. Pa. 1976).* (2012). doi:10.1097/BRS.0b013e31824444c4
14. Katagiri, T. *et al.* Bone morphogenetic protein-2 converts the differentiation pathway of C2C12 myoblasts into the osteoblast lineage. *J. Cell Biol.* (1994). doi:10.1083/jcb.127.6.1755
15. McKay, W. F., Peckham, S. M. & Badura, J. M. A comprehensive clinical review of recombinant human bone morphogenetic protein-2 (INFUSE® Bone Graft). *Int. Orthop.* **31**, 729–734 (2007).
16. Bonzani, I. C. *et al.* Synthesis of two-component injectable polyurethanes for bone tissue engineering. *Biomaterials* **28**, 423–433 (2007).
17. Dumas, J. E. *et al.* Synthesis, characterization, and remodeling of weight-bearing allograft bone/polyurethane composites in the rabbit. *Acta Biomater.* **6**, 2394–2406 (2010).
18. Dumas, J. E. *et al.* Balancing the rates of new bone formation and polymer degradation

enhances healing of weight-bearing allograft/polyurethane composites in rabbit femoral defects. *Tissue Eng. Part A* **20**, 115–29 (2014).
19. Page, J. M. *et al.* Biocompatibility and chemical reaction kinetics of injectable, settable polyurethane/allograft bone biocomposites. *Acta Biomater.* **8**, 4405–4416 (2012).
20. Hafeman, A. E. *et al.* Characterization of the degradation mechanisms of lysine-derived aliphatic poly(ester urethane) scaffolds. *Biomaterials* **32**, 419–429 (2011).
21. Zhang, J.-Y. *et al.* Synthesis, biodegradability, and biocompatibility of lysine diisocyanate-glucose polymers. *Tissue Eng.* **8**, 771–85 (2002).
22. McEnery, M. A. P. *et al.* Oxidatively degradable poly(thioketal urethane)/ceramic composite bone cements with bone-like strength. *RSC Adv.* **6**, 109414–109424 (2016).
23. Lu, S. *et al.* Settable polymer/ceramic composite bone grafts stabilize weight-bearing tibial plateau slot defects and integrate with host bone in an ovine model. *Biomaterials* **179**, 29–45 (2018).
24. McGough, M. A. P. *et al.* Nanocrystalline Hydroxyapatite-Poly(thioketal urethane) Nanocomposites Stimulate a Combined Intramembranous and Endochondral Ossification Response in Rabbits. *ACS Biomater. Sci. Eng.* **6**, 564–574 (2020).

CHAPTER II

# CHAPTER 2: BACKGROUND

## 2.1 Bone

Bone is a highly dynamic tissue which undergoes constant remodeling. It serves many functions within the body including structural support, protection of internal organs, maintenance of mineral homeostasis, hematopoiesis, and provides a reservoir for growth factors and cytokines.[1–3] There are two distinct types of bone: cortical and trabecular bone. Trabecular bone consists of a honey-comb structure of trabeculae within the bone marrow cavity whereas cortical bone is solid and dense found mainly in the shaft of long bones and surfaces of flat bones.[4,5] Due to the differences in porosity, the compressive strength of cortical bone and trabecular bone is roughly 100-180MPa and 2-12MPa, respectively.[6]

Bone extracellular matrix is comprised of roughly 30% organic material, 60% inorganic material, and 10% water.[7] The organic matrix of bone consists of predominantly of Type I collagen along with non-collagenous organic materials such as proteoglycans and glycoproteins, while the inorganic component is composed predominantly of calcium and phosphate in the form of hydroxyapatite crystals.[8,9]

There are four different cell types which make up bone: osteoblasts, bone lining cells, osteocytes, and osteoclasts.[10] Osteoblasts are cuboidal cells derived from mesenchymal stem cells (MSCs) responsible for bone formation. Osteoblasts make up 4 - 6% of the total bone forming cells.[11] The commitment of MSCs into osteoblasts consists of specific steps of gene expression including runt related transcription factor-2 and collagen II during differentiation, alkaline phosphatase during proliferation, and osterix and osteocalcin during transition to mature osteoblast.[3] The mature osteoblasts then form bone matrix through deposition and mineralization of the organic matrix.

As osteoblasts become entrapped within the secreted matrix, they become osteocytes. A subset of osteoblasts that do not undergo apoptosis or differentiate into osteocytes become bone lining cells.[12] These cells on the surface of bone are flat and non- bone forming, communicate closely with osteoclasts, and direct mineral uptake and release within bone. [13–15]

Osteocytes are the most abundant bone cells and make up 90-95% of the total bone forming cells.[16] Osteocytes are located within small cavities called lacunae and are surrounded by mineralized bone tissue.[17] While the osteocyte body is located in the lucana, they have cytoplasmic processes that extend through channels in the matrix called canaliculi. These processes allow the osteocytes to communicate with other osteocytes and receive nutrients.[17,18] Furthermore, the large network formed by osteocyte processes throughout the matrix is thought to contribute to their mechano-sensing ability.[18–20]

Osteoclasts are terminally differentiated multinucleated cells which originate from hematopoietic stem cell lineage.[13,21] These cells are responsible for the resorption and breakdown of bone. This process happens in 3 steps: osteoclast adhesion to the matrix, dissolution of the matrix via highly polarized osteoclasts with ruffled borders that secrete several organic acids, and finally, enzymatic digestion of the matrix.[21,22]

These different cells within bone work together to remodel bone. The cycle consists of five overlapping phases: activation, in which osteoclast precursors are recruited to the bone surface and activated; resorption, in which osteoclasts degrade old bone; reversal, when the switch from resorption to formation occurs; formation, when osteoblasts lay down new bone that replaces the previously resorbed bone; and termination, when the osteoblasts undergo either apoptosis, become embedded in matrix, or change into bone-lining cells.[23]

## 2.2 Fracture Remodeling

Due to the unique and dynamic nature of bone, small fractures can heal on their own in a temporally defined process.[24] Immediately following a fracture, both vascular supply and bone architecture are disrupted resulting in a loss of mechanical stability and a decrease in oxygen and nutrient supply. A fibrin-rich blood clot, known as the fracture hematoma, forms to resolve bleeding and achieve hemostasis.[25,26] Cytokines released by the clot cause an influx of neutrophils, B cells, T cells, and macrophages.[27–29] M1 macrophages play a pro-inflammatory role and work to debride the wound. The polarization of M1 macrophages to the anti-inflammatory M2 macrophage phenotype marks the shift from the inflammatory stage to the reparative stage.[30] This stage is defined by the recruitment of MSCs to the fracture site and vascular remodeling. This is followed by the bone formation stage where fracture healing occurs through two processes: primary (intramembranous) ossification and/or secondary (endochondral) ossification.

Endochondral ossification occurs when bone forms through an intermediate cartilaginous callus.[31,32] During this process, MSCs recruited to the fracture site differentiate into pre-hypertrophic chondrocytes and form an unmineralized cartilaginous callus to provide stabilization of the fracture.[24] Following stabilization, the chondrocytes begin to hypertrophy and release vascular endothelial growth factor (VEGF), bone morphogenetic protein (BMP), and hydroxyapatite (HA) to promote angiogenesis and ossification.[25,26,33] Hypertrophic chondrocytes within the callus contribute to new bone formation either by undergoing programmed cell death allowing for resorption, vascularization, and osteogenesis[34] or by transdifferentiating directly into osteoblasts and osteocytes.[35,36] Endochondral ossification often takes place in fractures with significant strain and can occur with limited initial vascularization.[26,37] This type of healing is most predominant in the diaphysis and long bones.[38,39]

Intramembranous ossification takes place when progenitor cells infiltrate the fracture site and undergo direct differentiation into osteoblasts followed by subsequent ossification and Haversian remodeling. This process occurs when the fracture gap is minimal and the defect site is both stable and sufficiently vascularized.[40,41] The metaphysis has been show to heal via intramembranous healing.[42]

Despite the two distinct processes by which bone forms, most fractures heal by a combination of both intramembranous and endochondral ossification due to the variable amounts of vascularity and strain in the fracture microenvironment.[24–26] When the fractures are small enough, the bone is able to carry these processes out on its own.[24] However, in instances where fractures are larger than critical size or patients have sustained significant trauma, intervention is required to support bone ingrowth.[43,44] Other comorbidities such as diabetes, age, and smoking present complications in bone healing and can require intervention. [45–47] Overall, roughly 5- 10% of all fractures result in delayed or non-union healing. [48] Thus, there is a significant need for bone grafts and bone substitutes to augment and guide bone healing.

## 2.3 Natural and Synthetic Bone Grafts and Substitutes

Bone grafting replaces missing bone with natural and synthetic substitutes to facilitate new bone formation and promote fracture healing. As natural bone grows into the graft or the substitute, it replaces the material over time leading to an integrated region of new and host bone.

*2.3.1 Natural bone grafts*. Autograft (AG), bone taken directly from the patient, has long been considered the 'gold standard' of bone grafting. It is osteoconductive, meaning it provides a platform that new bone can form on but does not directly guide osteogenesis.[49] Furthermore, autograft is osteoinductive, meaning it recruits progenitor cells to the fracture or defect site and actively induces new bone formation.[50–52] Beyond its osteogenic properties, autogenous bone is

advantageous due to its low material costs and its ability to mitigate the risk of disease transmission or immune rejection.[53,54] However, complications associated with AG include donor site morbidity, limited quantity, poor vascularization, and potential failure to integrate with host bone.[55,56]

Allograft, donor bone from human cadavers, is also frequently used for bone grafts. The advantages of allograft include its ease of use and ample availability.[57] However, the process of sterilizing and storing allograft affects not only its mechanical properties, but also its osteogenic and osteoinductive potential.[58,59] Furthermore allograft presents concerns with its potential immune response and high failure rates.[49,60] Due to these limitations with naturally occurring graft materials and the increasing need for bone grafts,[61] the development of synthetic bone substitutes has emerged as a promising strategy.

*2.3.2 Synthetic bone substitutes*. The ideal synthetic bone substitute is biocompatible, resorbable, osteoconductive, osteoinductive, porous, and mechanically similar to bone.[62] In order to meet these requirements, researchers have incorporated ceramics and polymers into substitute materials, utilizing the natural extracellular matrix of bone of bone as a guiding principle.

*Polymers.* Polymers are highly tunable and can be easily tailored to meet the needs of a bone substitute. Natural polymers derived from animal or plant tissues include proteins like collagen and silk fibroin along with polysaccharides such as chitosan, alginate, cellulose, and hyaluronic acid.[63–66] In general, these polymers are biocompatible and enhance cell adhesion and differentiation, but they lack the necessary mechanical strength for load bearing applications.[67,68] As mentioned in sectioned 2.1, collagen is the most abundant organic property in bone, thus it has been extensively studied as a bone substitute.[69] Collagen is advantageous in that it is biodegradable, promotes cell adhesion, and can be used in many forms including nanofibers,

scaffolds, sponges, and hydrogels.[70–72] The use of collagen is limited, however, by its rapid degradation and poor mechanical properties.[22,73,74]

To address the issues with immunogenicity with naturally occurring polymers and provide more tailored degradation, synthetic polymers are widely used in bone substitutes. In contrast to natural polymers, synthetic polymers exhibit reduced bioactivity and osteoconductivity.[79,80] Furthermore, their degradation products can be acidic and can cause inflammation.[81] Common synthetic polymers include poly (ϵ-caprolactone) (PCL), polylactide (PLA), poly(lactide-co-glycolide) (PLGA), and polyurethanes (PURs).[75–78]

PCL has been extensively studied as a bone substitute and is commonly used for long term implants due to its slower degradation rate.[76,82–85] PLA and PLGA degrade more rapidly than PCL, thus their use is more frequently employed for short-term applications such as non-load bearing defects and drug delivery via micro and nanoparticles. [86–88] Poly(methyl methacrylate) (PMMA) was extensively used as a bone cement, however, it is essentially non-degradable and exhibits poor mechanical properties.[89] PURs are easily synthesized under controlled conditions allowing for ideal and reproducible mechanical and biological properties that can be varied dependent on the specific applications. [71,90] PURs have been utilized in a wide range of applications including electrospun fibrous scaffolds, hydrogels, and foams.[91–94]

*Ceramics.* Ceramics are often utilized in bone substitutes. Ceramics are biocompatible and osteoconductive, however they possess brittle mechanical properties and resorb slowly.[41,95] Commonly used ceramics include calcium phosphates (CaPs) like calcium sulfate ($CaSO_4$), and β -tricalcium phosphate (β-TCP, Ca3(PO4)2), Hydroxyapatite (HA, $Ca_{10}(PO_4)_6(OH)_2$), and biphasic calcium phosphate comprised of a combination of HA and β-TCP.[96] The use of calcium sulfate was first reported in 1892.[97] Although it has been FDA approved since 1996, the resorption rate

of calcium sulfate is faster than that of bone deposition, thus it is not frequently used in early treatment.[98,99] Both β-TCP and HA are particularly interesting due to their similarity to the inorganic components of bone. β-TCP is frequently used in synthetic bone substitutes due to its porosity, safety profile, and resorption rate.[100,101] β – TCP resorbs slower than calcium sulfate but quicker than that of HA.[102,103] As previously mentioned in section 2.1, bone is made up of 60% mineral content consisting predominantly of HA. The similarity of synthetic HA, synthesized through the precipitation of calcium nitrate and ammonium dihydrogen phosphate, with that of naturally occurring HA has led to its wide use within synthetic bone substitutes.[104] HA maintains more optimal mechanical properties than that of β- TCP and integrates well with host bone.[104,105] However, HA resorbs slowly, persisting at least three years after implantation.[106] To achieve a more balanced rate of resorption, a combination of β -TCP and HA has been used. The use of β-TCP and HA together demonstrated faster and higher bone ingrowth when compared to HA alone and better mechanical properties when compared to β-TCP alone.[107,108]

*Composites.* To improve the properties of polymeric biomaterials, composites made from both synthetic and natural polymers and ceramics have been investigated extensively for bone replacements. Composite materials combine the osteoconductivity and osteogenic potential of the ceramic with the mechanical and degradation properties of polymers mimicking the ECM of bone.[109,110] Composite hydrogels, porous and fibrous scaffolds have all investigated for use in bone regeneration.[111–115] The addition of HA and β-TCP to PCL and PLGA demonstrated improved mechanical and bioactive properties.[116–119] Multiple studies have shown that HA increases osteogenesis,[120] thus HA has been incorporated in among a broad range of polymers including collagen, chitosan, PLGA, PCL, and PURs. [121–126]

## 2.4 Polyurethanes as Synthetic Bone Substitutes

PURs are increasingly used in bone regeneration due to their advantageous properties.[127–131] They are non-toxic, biocompatible, and highly tunable. Thus, the rate of degradation and the mechanical properties are easily altered through changes to the chemical composition and structure.[71] PUR based bone substitutes have demonstrated strengths ranging from 40 kPa for porous foams and up to 190 MPa for cements with moduli from the kPA to GPa range, and can thus be utilized for either cancellous or cortical bone substitutes.[132,133]

*2.4.1 Polyurethane synthesis.* PURs are synthesized by step growth polymerization using three basic components: polyols, polyisocyanates, and additives including catalysts and chain extenders.[134] Polyols are multi-functional alcohols that comprise a polyether, polyester, or polycarbonate backbone with a molecular weight ranging from 400-5,000g/mol.[128] The choice of polyol affects the rate of degradation of the resulting PUR. Polyisocyanates are characterized by their -N=C=O functionality and react with polyols and polyamines. Urethane linkages are formed by the reaction of isocyanates with hydroxyl groups while urea linkages are formed by the reaction of isocyanates with amines. [128,135] PURs used in bone substitutes are most frequently synthesized from either lysine-or hexamethylene-derived aliphatic polyisocyanates including lysine triisocyanate (LTI), lysine diisocyanate , and hexamethylene diisocyanate due to carcinogenic and toxicity concerns associated with conventional aromatic polyisocyanates such as methylene diisocyanate.[136,137]

The polymerization process can be either a one- or two-step process. In the one-step process, polyol, chain extender, water or other additives are mixed together with the polyisocyanate resulting in a rapid and exothermic reaction that occurs without an additional catalyst.[134] In the two-step process, a prepolymer, providing an additional degree of control over

the PUR structure, is utilized. In the first step, a prepolymer is synthesized by reacting polyol with an excess of isocyanates. The prepolymer is thus a mixture of oligomeric intermediates with isocyanate functionality.[128] Prepolymers are defined as having an NCO:OH ratio of 2:1, however quasi-prepolymers with a range of functionalities are often used.[135] In the second step, the prepolymer is reacted with polyol. The resulting reactive liquid mixture can be injected and hardens to a solid in the site of injection. To achieve the desired final PUR structure, the rates of the gelling 'polymerization' reaction and blowing reaction must be balanced. The blowing reaction, crucial for the synthesis of PUR porous foams, refers to the presence of water in the reaction. The presence of water leads to the formation of carbamic acid, an unstable compound that breaks down to an amine and carbon dioxide gas, resulting in porous structure.[128] The blowing reaction is catalyzed by tertiary amines.[138]

*2.4.2 Polyurethane degradation.* PURs are designed to undergo hydrolytic degradation *in vivo* in which ester linkages are hydrolyzed, yielding α-hydroxy acids, urethane and urea fragments.[128] The rate of PUR degradation is controlled not only by the type of polyol and polyisocyanates used, but also the degree of crosslinking and the structure of the PUR. [134] However, hydrolytic degradation can be unreliable and lead to rapid degradation.

More recently, novel poly (thioketal urethane) (PTKURs) scaffolds have been developed for bone regeneration applications.[139–141] PTKUR degrades in response to cell-secreted ROS from macrophages and other adherent inflammatory cells.[142,143] Thioketal bonds degrade to thiol decomposition products with low toxicity.[142] PTKUR is advantageous in that its degradation is more stable and controlled than that of PURs.[141] While PTKURs support cellular infiltration and degradation in subcutaneous sites, degradation of PTKUR based composites in bone has not been extensively evaluated.[142,144]

## 2.5 Promoting Osteoinductivity in Synthetic Bone Substitutes

As mentioned in section 2.3, osteoinductive scaffolds direct new bone formation through biological signals that stimulate proliferation and differentiation of MSCs.[145] While composite scaffolds are inherently osteoconductive, they generally lack the osteoinductivity needed to successfully promote regeneration. Thus, additional factors may be required to provide the osteoinductivity needed to promote bony union at defect sites.

*2.5.1 Growth factors.* In the natural bone healing cycle, growth factors are produced by bone marrow stromal cells, endothelial cells, fibroblasts, inflammatory cells, and osteoblasts.[146] The major growth factors involved in bone remodeling include BMP, VEGF, fibroblast growth factor (FGF), insulin-like growth factor (IGF-1), platelet-derived growth factor (PDGF), and transforming growth factor – β (TGF-β).[145]

As mentioned in section 2.2, blood supply must be restored after a fracture to promote the formation of new bone. VEGF is fundamental for angiogenesis in fracture healing. Multiple studies have shown exogenous VEGF to be effective in promoting fracture healing.[147–149] It has been postulated that VEGF contributes to bone maturation but does not enhance the amount of new bone formation.[150] Furthermore, PDGF upregulates VEGF and has shown to play a crucial role in regulating angiogenesis to correlate with the rate of bone formation.[151,152] FGFs, specifically FGF-2, are also implicated in angiogenesis and bone regeneration. Similarly, FGF-2 was also found to be effective in promoting fracture healing.[153,154] Although TGF-β plays a crucial role in bone healing, its key function is limited to the production of extracellular proteins for callus formation, and does not play a direct role in mineralization.[155] IGF-1 is localized at the fracture site and plays a critical role in fracture healing by promoting collagen I formation.[156,157] While the above growth

factors have all been investigated for the osteogenic potential,[147,158–162] BMPs have shown the greatest success.

BMPs, part of the TGF-β superfamily, were first discovered as osteoinductive growth factors by Urist and have shown significant success in bone regeneration.[163,164] There are over 20 BMPs, but BMP-2 and BMP-7 have been extensively investigated for bone-regeneration applications.[165] BMP-2 has been FDA approved for clinical use as INFUSE® bone graft (Medtronic), an absorbable collagen sponge rhBMP-2 carrier approved for the treatment of posterior-lateral spinal fusion, tibial fractures, sinus lift procedures, and extraction socket defects.[166] The bone induced INFUSE® remodels to assume the appropriate structure of host bone.[167] However, the carrier is unable to withstand compressive forces. Thus, a protective membrane is required to maintain space and protect the carrier from mechanical forces. Both resorbable and non-resorbable membranes are associated with problems including wound dehiscence, and healing complications.[168] Resorbable membranes commonly cause swelling and inflammation problems while non-resorbable membranes must be subsequently removed.[169] Additionally, off-label use and side effects associated with BMP-2 such as swelling, ectopic bone formation and carcinogenic risks do exist. [170–173] BMP-7 was approved under a Humanitarian Device Exemption for posterolateral lumbar fusion. However, it did not meet the stringent FDA requirements and the differences between patient data and historical controls was not significant.[174] It has yet to obtain complete FDA approval.

*2.5.2 Cell based strategies.* MSCs have the ability to differentiate into various tissue lineages, including bone, cartilage, muscle, and fat.[175] MSCs can be isolated from various tissues including adipose tissue, tendons and ligaments, bone marrow, and embryonic tissue,[176–180] and ex vivo processing and culture methods have been developed to obtain sufficient MSCs for

therapy.[181,182] Cell-based therapies to regenerate bone were initially based on the idea that transplanted MSCs would replace the role of endogenous cells within the fracture site and differentiate into new bone.[183] However, efforts towards clinical translation have been hindered by high costs related to good manufacturing practice guidelines and challenges in regulatory approval.[182] The combination of MSCs with engineered bone substitutes has also been investigated. Preclinical studies demonstrated that the survival of cells within scaffolds is limited after *in vivo* transplantation.[184–186] The scaffold must exhibit interconnected pores to allow for transport of cell nutrients and waste.

*2.5.3 Nano-structured ceramics.* As previously discussed in section 2.3.2, ceramics are advantageous due to their biocompatibility and osteoconductive properties. More recently, it has been demonstrated that cell adhesion, proliferation, and calcium deposition is greatly improved on nanophase ceramics, ceramics that are less than 100nm in either direction, compared to micron-sized conventional substrates. [188–190] Nano-structured ceramics are advantageous due to their high-cell surface interactions.[189,191,192] Furthermore, nano-ceramics exhibit improved mechanical properties including increased tensile strength, bending strength, impact energy and moduli closer to that of natural bone. [193,194] The optimal size for nano-ceramics is between 10-100nm as they are able to freely interact with various body receptors, and are able to cross the cell membrane.[195,196]

*2.5.4 Autograft.* Although rhBMP-2 holds great promise in promoting successful bone regeneration, complications of off-label use in the spine include paralysis, respiratory failure, inflammation of adjacent tissues, and even death.[197] AG alone presents complications, as outlined in section 2.3.1, however strategies to exploit the osteoinductivity of autograft have been investigated, specifically in spinal applications.[198] AG has been mixed with both ceramic and polymeric materials as bone extenders, meant to extend the life of AG at the defect site and increase

the volume of natural bone substitutes.[199–202] A recent study utilized PTKUR based AG extender in an intertransverse process in rabbits. While the PTKUR enhanced handling and mechanical properties of the AG, residual material due to limited degradation reduced cellular infiltration and new bone formation.[203] Thus, the ideal AG composition must be identified to allow for synergistic effects of material degradation and autograft bone extender.

## 2.6 Evaluating Outcomes in Bone Healing

*In vivo* studies are necessary to evaluate bone substitutes and bone regeneration. Of course, *in vitro* studies to evaluate biocompatibility, safety, and osteogenic potential must be performed prior to *in vivo* studies. However, the complex relationship between different cell types in the bone and the ongoing cycle of remodeling warrant *in vivo* studies to determine bone grafts and substitutes efficacy. Animals commonly used for bone regeneration studies include rats, canines (purpose-bred beagles and coon hounds), rabbits, sheep, and pigs.[204] The animal models are selected and utilized dependent upon intended applications, anatomic sites, and material selections.[204] For bone substitutes to achieve FDA approval, proof of efficacy must be reported in a minimum of one small animal and one large animal.[205] For bone substitutes that utilize biologics, such as rhBMP-2, the proper dose of the biologic must be demonstrated in a non-human primate model.[206]

*2.6.1 Histology and histomorphometry.* Histology is often performed to evaluate cellular activity and bone formation *in vivo*. It can be performed on paraffin embedded, plastic embedded, or frozen sections. Un-decalcified, plastic embedded ground sections are traditionally used for large, calcium-based implants.[207] These sections typically range from 50-150µm in thickness and yield poor cellular detail. These sections, however, can be utilized for stains such as Sanderson's Rapid Bone Stain, Stevenel's Blue and Massons trichome, which can differentiate various

connective tissue (i.e. bone, cartilage, muscle).[208] Additionally these sections can be utilized for von Kossa staining, performed to determine the degree of mineralization, and Safranin O staining, performed to detect cartilage. The above stains, however, do not demonstrate temporal changes.

Fluorochrome injections, including tetracyclines, Calcein green, and xylenol orange, offer a dynamic method to monitor mineralization temporarily in un-decalcified sections.[209] Fluorochromes are injected subcutaneously and bind selectively to actively mineralizing tissue during the time of circulation (around 24 hours). Mineralization can be monitored over time in the same subject by injecting fluorochromes with different emission wavelengths at various times.

For higher magnification histology, paraffin and frozen sections range from 4-6μm in thickness and allow for single-cell visualization. Paraffin sections must typically be decalcified. Decalcification can affect the immunohistochemical characteristics and integrity of the tissue, thus careful selection of decalcification agents is essential.[210] Additionally, the decalcification process can take multiple weeks to complete. In contrast to decalcified paraffin-embedded sections, frozen sections are flash frozen in liquid nitrogen and allow for rapid embedding and sectioning. However frozen sections present challenges in that samples cannot exceed the mold sizes for freezing and bone can be challenging to section, frequently damaging the blade. More recently, cryosectioning protocols have been developed to preserve the morphology of mineralized tissue.[211] These sections not only allow for the staining protocols mentioned previously, but also immunohistochemistry (IHC) and immunofluorescent analysis allowing for a better understanding of cellular behavior within scaffolds and bone substitutes.

Histomorphometry allows for quantitative evaluation of new bone formation and bone parameters.[212,213] Histomorphometry is performed by measuring the amount of fibrous, cartilage, and total osseous tissue within a region of interest in histological samples. Typically, stains such

as von Kossa, Stevenel's blue, and Safranin O where various tissue types can be clearly identified through the color of the stain are used for histomorphometry. Histomorphometry can be used to evaluate the progression of bone healing over several time points and can be used to determine the rate of healing or the efficacy of a bone substitute.[212] Values can be reported as either total or percentages of fibrous, cartilage, and total osseous tissue. Measurements of void areas or cellular infiltration can also be reported. Bone is, however, highly heterogenous and presents challenges in histomorphometric analysis. Thus, transverse sections provide the optimal conditions for long bone analysis. Additionally, histomorphometry measures areas within 2D sections and does not provide a 3D analysis of tissue within the entirety of a bone or defect site.

*2.6.2 µCT.* Micro-computed tomography (µCT) allows for high resolution quantitative 2D and 3D evaluation of bone *ex vivo*. Bone specimens and samples are isolated, fixed in formalin, organic alcohols, or acetone, and scanned using µCT with voxel sizes at the micron-level.[214] 3D images are obtained and reconstructed utilizing ScancoMedical software.[214] After reconstruction, the 3D image can be analyzed to calculate parameters including bone volume/total volume (BV/TV ), trabecular spacing (Tb. S.), trabecular thickness (Tb. Th.), and trabecular number (Tb. N.) over the entire bone or within a specific area of interest.[215] Careful use of thresholding must be applied in order to distinguish calcium phosphate ceramic particles from bone. *In vivo* µCT enables the evaluation of structural changes over time in the same animal to evaluate treatment efficacy. However, high radiation doses associated with *in vivo* µCT limits its use to preclinical studies.

References


1. Clarke, B. Normal bone anatomy and physiology. *Clin. J. Am. Soc. Nephrol.* (2008). doi:10.2215/CJN.04151206
2. Taichman, R. S. Blood and bone: Two tissues whose fates are intertwined to create the hematopoietic stem-cell niche. *Blood* (2005). doi:10.1182/blood-2004-06-2480
3. Florencio-Silva, R., Sasso, G. R. D. S., Sasso-Cerri, E., Simões, M. J. & Cerri, P. S. Biology of Bone Tissue: Structure, Function, and Factors That Influence Bone Cells. *BioMed Research International* (2015). doi:10.1155/2015/421746
4. Singh, I. The architecture of cancellous bone. *J. Anat.* (1978).
5. Osterhoff, G. *et al.* Bone mechanical properties and changes with osteoporosis. *Injury* (2016). doi:10.1016/S0020-1383(16)47003-8
6. Fu, Q., Saiz, E., Rahaman, M. N. & Tomsia, A. P. Bioactive glass scaffolds for bone tissue engineering: State of the art and future perspectives. *Materials Science and Engineering C* (2011). doi:10.1016/j.msec.2011.04.022
7. Athanasiou, K. A., Zhu, C. F., Lanctot, D. R., Agrawal, C. M. & Wang, X. Fundamentals of biomechanics in tissue engineering of bone. in *Tissue Engineering* (2000). doi:10.1089/107632700418083
8. Feng, X. Chemical and Biochemical Basis of Cell-Bone Matrix Interaction in Health and Disease. *Curr. Chem. Biol.* (2009). doi:10.2174/187231309788166398
9. Aszódi, A., Bateman, J. F., Gustafsson, E., Boot-Handford, R. & Fässler, R. Mammalian skeletogenesis and extracellular matrix: What can we learn from knockout mice? *Cell Struct. Funct.* (2000). doi:10.1247/csf.25.73
10. Buckwalter, J. A., Glimcher, M. J., Cooper, R. R. & Recker, R. Bone biology. I: Structure, blood supply, cells, matrix, and mineralization. *Instructional course lectures* (1996).
11. Capulli, M., Paone, R. & Rucci, N. Osteoblast and osteocyte: Games without frontiers. *Archives of Biochemistry and Biophysics* (2014). doi:10.1016/j.abb.2014.05.003
12. Karsdal, M. A. *et al.* Matrix metalloproteinase-dependent activation of latent transforming growth factor-β controls the conversion of osteoblasts into osteocytes by blocking osteoblast apoptosis. *J. Biol. Chem.* (2002). doi:10.1074/jbc.M207205200
13. Streicher, C. *et al.* Estrogen Regulates Bone Turnover by Targeting RANKL Expression in Bone Lining Cells. *Sci. Rep.* (2017). doi:10.1038/s41598-017-06614-0
14. Matsuo, K. & Irie, N. Osteoclast-osteoblast communication. *Archives of Biochemistry and Biophysics* (2008). doi:10.1016/j.abb.2008.03.027
15. Everts, V. *et al.* The bone lining cell: Its role in cleaning Howship's lacunae and initiating bone formation. *J. Bone Miner. Res.* (2002). doi:10.1359/jbmr.2002.17.1.77
16. Franz-Odendaal, T. A., Hall, B. K. & Witten, P. E. Buried alive: How osteoblasts become osteocytes. *Developmental Dynamics* (2006). doi:10.1002/dvdy.20603
17. Dallas, S. L., Prideaux, M. & Bonewald, L. F. The osteocyte: An endocrine cell . . . and more. *Endocrine Reviews* (2013). doi:10.1210/er.2012-1026
18. Schaffler, M. B., Cheung, W. Y., Majeska, R. & Kennedy, O. Osteocytes: Master orchestrators of bone. *Calcified Tissue International* (2014). doi:10.1007/s00223-013-9790-y
19. Klein-Nulend, J. & Bakker, A. D. Osteocytes: Mechanosensors of bone and orchestrators of mechanical adaptation. *Clinical Reviews in Bone and Mineral Metabolism* (2007).

doi:10.1007/s12018-008-9014-6
20. Thi, M. M., Suadicani, S. O., Schaffler, M. B., Weinbaum, S. & Spray, D. C. Mechanosensory responses of osteocytes to physiological forces occur along processes and not cell body and require αvβ3 integrin. *Proc. Natl. Acad. Sci. U. S. A.* (2013). doi:10.1073/pnas.1321210110
21. Väänänen, H. K. & Laitala-Leinonen, T. Osteoclast lineage and function. *Archives of Biochemistry and Biophysics* (2008). doi:10.1016/j.abb.2008.03.037
22. Donnaloja, F., Jacchetti, E., Soncini, M. & Raimondi, M. T. Natural and synthetic polymers for bone scaffolds optimization. *Polymers* (2020). doi:10.3390/POLYM12040905
23. Kenkre, J. S. & Bassett, J. H. D. The bone remodelling cycle. *Annals of Clinical Biochemistry* (2018). doi:10.1177/0004563218759371
24. Einhorn, T. A. & Gerstenfeld, L. C. Fracture healing: Mechanisms and interventions. *Nature Reviews Rheumatology* (2015). doi:10.1038/nrrheum.2014.164
25. Bahney, C. S. *et al.* Cellular biology of fracture healing. *Journal of Orthopaedic Research* (2019). doi:10.1002/jor.24170
26. Baker, C. E. *et al.* Bone Fracture Acute Phase Response—A Unifying Theory of Fracture Repair: Clinical and Scientific Implications. *Clin. Rev. Bone Miner. Metab.* **16**, 142–158 (2018).
27. Loi, F. *et al.* Inflammation, fracture and bone repair. *Bone* (2016). doi:10.1016/j.bone.2016.02.020
28. Schmidt-Bleek, K. *et al.* Inflammatory phase of bone healing initiates the regenerative healing cascade. *Cell Tissue Res.* (2012). doi:10.1007/s00441-011-1205-7
29. Schmidt-Bleek, K., Kwee, B. J., Mooney, D. J. & Duda, G. N. Boon and Bane of Inflammation in Bone Tissue Regeneration and Its Link with Angiogenesis. *Tissue Engineering - Part B: Reviews* (2015). doi:10.1089/ten.teb.2014.0677
30. Benoit, M., Desnues, B. & Mege, J.-L. Macrophage Polarization in Bacterial Infections. *J. Immunol.* (2008). doi:10.4049/jimmunol.181.6.3733
31. Marsell, R. & Einhorn, T. A. The biology of fracture healing. *Injury* (2011). doi:10.1016/j.injury.2011.03.031
32. Mackie, E. J., Ahmed, Y. A., Tatarczuch, L., Chen, K. S. & Mirams, M. Endochondral ossification: How cartilage is converted into bone in the developing skeleton. *International Journal of Biochemistry and Cell Biology* (2008). doi:10.1016/j.biocel.2007.06.009
33. Gerber, H. P. *et al.* VEGF couples hypertrophic cartilage remodeling, ossification and angiogenesis during endochondral bone formation. *Nat. Med.* (1999). doi:10.1038/9467
34. Kronenberg, H. M. Developmental regulation of the growth plate. *Nature* (2003). doi:10.1038/nature01657
35. Yang, L., Tsang, K. Y., Tang, H. C., Chan, D. & Cheah, K. S. E. Hypertrophic chondrocytes can become osteoblasts and osteocytes in endochondral bone formation. *Proc. Natl. Acad. Sci. U. S. A.* (2014). doi:10.1073/pnas.1302703111
36. Aghajanian, P. & Mohan, S. The art of building bone: Emerging role of chondrocyte-to-osteoblast transdifferentiation in endochondral ossification. *Bone Res.* (2018). doi:10.1038/s41413-018-0021-z
37. Dennis, S. C., Berkland, C. J., Bonewald, L. F. & Detamore, M. S. Endochondral Ossification for Enhancing Bone Regeneration: Converging Native Extracellular Matrix

Biomaterials and Developmental Engineering in Vivo. *Tissue Engineering - Part B: Reviews* (2015). doi:10.1089/ten.teb.2014.0419
38. Ford, J. L., Robinson, D. E. & Scammell, B. E. Endochondral ossification in fracture callus during long bone repair: The localisation of 'cavity-lining cells' within the cartilage. *J. Orthop. Res.* (2004). doi:10.1016/j.orthres.2003.08.010
39. Petersen, A. *et al.* A biomaterial with a channel-like pore architecture induces endochondral healing of bone defects. *Nat. Commun.* **9**, 4430 (2018).
40. Percival, C. J. & Richtsmeier, J. T. Angiogenesis and intramembranous osteogenesis. *Developmental Dynamics* (2013). doi:10.1002/dvdy.23992
41. Wang, W. & Yeung, K. W. K. Bone grafts and biomaterials substitutes for bone defect repair: A review. *Bioactive Materials* (2017). doi:10.1016/j.bioactmat.2017.05.007
42. Sandberg, O. H. & Aspenberg, P. Inter-trabecular bone formation: a specific mechanism for healing of cancellous bone: A narrative review. *Acta Orthop.* (2016). doi:10.1080/17453674.2016.1205172
43. Hollinger, J. & Kleinschmidt, J. The critical size defect as an experimental model to test bone repair materials. *J. Craniofac. Surg.* **1**, 60–68 (1990).
44. Seta, J. Healing of bone fracture: general concepts. in *Principles of Bone Regeneration* (eds. Seta, J. & Bab, I.) 1–8 (Springer Science & Business Media, 2012).
45. Hernandez, R. K., Do, T. P., Critchlow, C. W., Dent, R. E. & Jick, S. S. Patient-related risk factors for fracture-healing complications in the United Kingdom General Practice Research Database. *Acta Orthop.* (2012). doi:10.3109/17453674.2012.747054
46. The effect of smoking on bone healing: A systematic review. *Bone Jt. Res.* (2013). doi:10.1302/2046-3758.26.2000142
47. Edelmuth, S. V. C. L., Sorio, G. N., Sprovieri, F. A. A., Gali, J. C. & Peron, S. F. Comorbidities, clinical intercurrences, and factors associated with mortality in elderly patients admitted for a hip fracture. *Rev. Bras. Ortop. (English Ed.* (2018). doi:10.1016/j.rboe.2018.07.014
48. Gómez-Barrena, E. *et al.* Bone fracture healing: Cell therapy in delayed unions and nonunions. *Bone* (2015). doi:10.1016/j.bone.2014.07.033
49. Yu, X., Tang, X., Gohil, S. V. & Laurencin, C. T. Biomaterials for Bone Regenerative Engineering. *Advanced Healthcare Materials* **4**, 1268–1285 (2015).
50. Albrektsson, T. & Johansson, C. Osteoinduction, osteoconduction and osseointegration. *Eur. Spine J.* **10**, S96–S101 (2001).
51. Shafiei, Z., Bigham, A. S., Dehghani, S. N. & Torabi Nezhad, S. Fresh cortical autograft versus fresh cortical allograft effects on experimental bone healing in rabbits: Radiological, Histopathological and Biomechanical evaluation. *Cell Tissue Bank.* **10**, 19–26 (2009).
52. Winkler, T., Sass, F. A., Duda, G. N. & Schmidt-Bleek, K. A review of biomaterials in bone defect healing, remaining shortcomings and future opportunities for bone tissue engineering: The unsolved challenge. *Bone and Joint Research* (2018). doi:10.1302/2046-3758.73.BJR-2017-0270.R1
53. Misch, C. M. Autogenous bone: Is it still the gold standard? *Implant Dentistry* (2010). doi:10.1097/ID.0b013e3181f8115b
54. Rogers, G. F. & Greene, A. K. Autogenous bone graft: Basic science and clinical implications. *J. Craniofac. Surg.* (2012). doi:10.1097/SCS.0b013e318241dcba
55. Kalk, W. W. ., Raghoebar, G. M., Jansma, J. & Boering, G. Morbidity from iliac crest

bone harvesting. *J. Oral Maxillofac. Surg.* **54**, 1424–1429 (1996).
56. Chim, H. & Gosain, A. K. Biomaterials in craniofacial surgery: experimental studies and clinical application. *J. Craniofac. Surg.* **20**, 29–33 (2009).
57. Moore, M. A., Samsell, B. & McLean, J. Allograft tissue safety and technology. in *Biologics in Orthopaedic Surgery* (2018). doi:10.1016/B978-0-323-55140-3.00005-9
58. Herron, L. D. & Newman, M. H. The failure of ethylene oxide gas-sterilized freeze-dried bone graft for thoracic and lumbar spinal fusion. *Spine (Phila. Pa. 1976).* (1989). doi:10.1097/00007632-198905000-00004
59. An, H. S., Michael Simpson, J., Michael Glover, J. & Stephany, J. Comparison between allograft plus demineralized bone matrix versus autograft in anterior cervical fusion: A prospective multicenter study. *Spine (Phila. Pa. 1976).* (1995). doi:10.1097/00007632-199510001-00006
60. Aponte-Tinao, L. A., Ayerza, M. A., Muscolo, D. L. & Farfalli, G. L. What Are the Risk Factors and Management Options for Infection After Reconstruction With Massive Bone Allografts? *Clin. Orthop. Relat. Res.* (2016). doi:10.1007/s11999-015-4353-3
61. Amin, S., Achenbach, S. J., Atkinson, E. J., Khosla, S. & Melton, L. J. Trends in fracture incidence: A population-based study over 20 years. *J. Bone Miner. Res.* (2014). doi:10.1002/jbmr.2072
62. Greenwald, A. S. *et al.* Bone-graft substitutes: Facts, fictions, and applications. in *Journal of Bone and Joint Surgery - Series A* (2001). doi:10.2106/00004623-200100022-00007
63. Melke, J., Midha, S., Ghosh, S., Ito, K. & Hofmann, S. Silk fibroin as biomaterial for bone tissue engineering. *Acta Biomaterialia* (2016). doi:10.1016/j.actbio.2015.09.005
64. LeGeros, R. Z. Properties of osteoconductive biomaterials: Calcium phosphates. in *Clinical Orthopaedics and Related Research* 81–98 (2002). doi:10.1097/00003086-200202000-00009
65. Venkatesan, J., Bhatnagar, I., Manivasagan, P., Kang, K. H. & Kim, S. K. Alginate composites for bone tissue engineering: A review. *International Journal of Biological Macromolecules* (2015). doi:10.1016/j.ijbiomac.2014.07.008
66. Klemm, D., Heublein, B., Fink, H. P. & Bohn, A. Cellulose: Fascinating biopolymer and sustainable raw material. *Angewandte Chemie - International Edition* (2005). doi:10.1002/anie.200460587
67. Bhattarai, D. P., Aguilar, L. E., Park, C. H. & Kim, C. S. A review on properties of natural and synthetic based electrospun fibrous materials for bone tissue engineering. *Membranes* (2018). doi:10.3390/membranes8030062
68. Armentano, I., Dottori, M., Fortunati, E., Mattioli, S. & Kenny, J. M. Biodegradable polymer matrix nanocomposites for tissue engineering: A review. in *Polymer Degradation and Stability* (2010). doi:10.1016/j.polymdegradstab.2010.06.007
69. Luvizuto, E. R. *et al.* Osteoconductive properties of β-tricalcium phosphate matrix, polylactic and polyglycolic acid gel, and calcium phosphate cement in bone defects. *J. Craniofac. Surg.* (2012). doi:10.1097/SCS.0b013e31825e4abf
70. Wang, L. & Stegemann, J. P. Thermogelling chitosan and collagen composite hydrogels initiated with β-glycerophosphate for bone tissue engineering. *Biomaterials* (2010). doi:10.1016/j.biomaterials.2010.01.131
71. Shi, C., Yuan, Z., Han, F., Zhu, C. & Li, B. Polymeric biomaterials for bone regeneration. *Ann. Jt.* (2016). doi:10.21037/aoj.2016.11.02
72. Matthews, J. A., Wnek, G. E., Simpson, D. G. & Bowlin, G. L. Electrospinning of

collagen nanofibers. *Biomacromolecules* (2002). doi:10.1021/bm015533u
73. Holzwarth, J. M. & Ma, P. X. Biomimetic nanofibrous scaffolds for bone tissue engineering. *Biomaterials* (2011). doi:10.1016/j.biomaterials.2011.09.009
74. Yu, H. S., Won, J. E., Jin, G. Z. & Kim, H. W. Construction of mesenchymal stem cell-containing collagen gel with a macrochanneled polycaprolactone scaffold and the flow perfusion culturing for bone tissue engineering. *Biores. Open Access* (2012). doi:10.1089/biores.2012.0234
75. Gentile, P., Chiono, V., Carmagnola, I. & Hatton, P. V. An overview of poly(lactic-co-glycolic) Acid (PLGA)-based biomaterials for bone tissue engineering. *International Journal of Molecular Sciences* (2014). doi:10.3390/ijms15033640
76. Dwivedi, R. *et al.* Polycaprolactone as biomaterial for bone scaffolds: Review of literature. *Journal of Oral Biology and Craniofacial Research* (2020). doi:10.1016/j.jobcr.2019.10.003
77. Stevens, B., Yang, Y., Mohandas, A., Stucker, B. & Nguyen, K. T. A review of materials, fabrication methods, and strategies used to enhance bone regeneration in engineered bone tissues. *Journal of Biomedical Materials Research - Part B Applied Biomaterials* (2008). doi:10.1002/jbm.b.30962
78. Asti, A. & Gioglio, L. Natural and synthetic biodegradable polymers: Different scaffolds for cell expansion and tissue formation. *International Journal of Artificial Organs* (2014). doi:10.530/ijao.5000307
79. Gautam, S., Dinda, A. K. & Mishra, N. C. Fabrication and characterization of PCL/gelatin composite nanofibrous scaffold for tissue engineering applications by electrospinning method. *Mater. Sci. Eng. C* (2013). doi:10.1016/j.msec.2012.12.015
80. Gao, C., Peng, S., Feng, P. & Shuai, C. Bone biomaterials and interactions with stem cells. *Bone Research* (2017). doi:10.1038/boneres.2017.59
81. Major, R., Lackner, J. M., Sanak, M. & Major, B. Silver nanoparticles influence on the blood activation process and their release to blood plasma from synthetic polymer scaffold. in *IOP Conference Series: Materials Science and Engineering* (2016). doi:10.1088/1757-899X/119/1/012031
82. Savarino, L. *et al.* The performance of poly-ε-caprolactone scaffolds in a rabbit femur model with and without autologous stromal cells and BMP4. *Biomaterials* (2007). doi:10.1016/j.biomaterials.2007.03.011
83. Dikici, B. A., Dikici, S., Reilly, G. C., MacNeil, S. & Claeyssens, F. A novel bilayer polycaprolactone membrane for guided bone regeneration: Combining electrospinning and emulsion templating. *Materials (Basel).* (2019). doi:10.3390/ma12162643
84. Chern, M. J., Yang, L. Y., Shen, Y. K. & Hung, J. H. 3D scaffold with PCL combined biomedical ceramic materials for bone tissue regeneration. *Int. J. Precis. Eng. Manuf.* (2013). doi:10.1007/s12541-013-0298-1
85. Heydari, Z., Mohebbi-Kalhori, D. & Afarani, M. S. Engineered electrospun polycaprolactone (PCL)/octacalcium phosphate (OCP) scaffold for bone tissue engineering. *Mater. Sci. Eng. C* (2017). doi:10.1016/j.msec.2017.07.041
86. Sung, H. J., Meredith, C., Johnson, C. & Galis, Z. S. The effect of scaffold degradation rate on three-dimensional cell growth and angiogenesis. *Biomaterials* (2004). doi:10.1016/j.biomaterials.2004.01.066
87. Elmowafy, E. M., Tiboni, M. & Soliman, M. E. Biocompatibility, biodegradation and biomedical applications of poly(lactic acid)/poly(lactic-co-glycolic acid) micro and

nanoparticles. *Journal of Pharmaceutical Investigation* (2019). doi:10.1007/s40005-019-00439-x

88. Ortega-Oller, I. *et al.* Bone Regeneration from PLGA Micro-Nanoparticles. *BioMed Research International* (2015). doi:10.1155/2015/415289
89. Kowalczewski, C. J. & Saul, J. M. Biomaterials for the delivery of growth factors and other therapeutic agents in tissue engineering approaches to bone regeneration. *Frontiers in Pharmacology* (2018). doi:10.3389/fphar.2018.00513
90. Tian, H., Tang, Z., Zhuang, X., Chen, X. & Jing, X. Biodegradable synthetic polymers: Preparation, functionalization and biomedical application. *Progress in Polymer Science (Oxford)* (2012). doi:10.1016/j.progpolymsci.2011.06.004
91. Tetteh, G., Khan, A. S., Delaine-Smith, R. M., Reilly, G. C. & Rehman, I. U. Electrospun polyurethane/hydroxyapatite bioactive Scaffolds for bone tissue engineering: The role of solvent and hydroxyapatite particles. *J. Mech. Behav. Biomed. Mater.* (2014). doi:10.1016/j.jmbbm.2014.06.019
92. Guelcher, S. A. *et al.* Synthesis and in vitro biocompatibility of injectable polyurethane foam scaffolds. *Tissue Eng.* **12**, 1247–1259 (2006).
93. Mi, H. Y. *et al.* Thermoplastic polyurethane/hydroxyapatite electrospun scaffolds for bone tissue engineering: Effects of polymer properties and particle size. *J. Biomed. Mater. Res. - Part B Appl. Biomater.* (2014). doi:10.1002/jbm.b.33122
94. Liu, M. *et al.* Injectable hydrogels for cartilage and bone tissue engineering. *Bone Research* (2017). doi:10.1038/boneres.2017.14
95. Iaquinta, M. R. *et al.* Innovative biomaterials for bone regrowth. *International Journal of Molecular Sciences* (2019). doi:10.3390/ijms20030618
96. Fernandez de Grado, G. *et al.* Bone substitutes: a review of their characteristics, clinical use, and perspectives for large bone defects management. *Journal of Tissue Engineering* (2018). doi:10.1177/2041731418776819
97. Campana, V. *et al.* Bone substitutes in orthopaedic surgery: from basic science to clinical practice. *J. Mater. Sci. Mater. Med.* (2014). doi:10.1007/s10856-014-5240-2
98. Beuerlein, M. J. S. & McKee, M. D. Calcium sulfates: What is the evidence? *Journal of Orthopaedic Trauma* (2010). doi:10.1097/BOT.0b013e3181cec48e
99. Chai, F., Raoul, G., Wiss, A., Ferri, J. & Hildebrand, H. F. [Bone substitutes: Classification and concerns]. *Rev. Stomatol. Chir. Maxillofac.* (2011).
100. Gaasbeek, R. D. A., Toonen, H. G., Van Heerwaarden, R. J. & Buma, P. Mechanism of bone incorporation of β-TCP bone substitute in open wedge tibial osteotomy in patients. *Biomaterials* (2005). doi:10.1016/j.biomaterials.2005.04.056
101. Chazono, M., Tanaka, T., Komaki, H. & Fujii, K. Bone formation and bioresorption after implantation of injectable β-tricalcium phosphate granules-hyaluronate complex in rabbit bone defects. *J. Biomed. Mater. Res. - Part A* (2004). doi:10.1002/jbm.a.30094
102. Roberts, T. T. & Rosenbaum, A. J. Bone grafts, bone substitutes and orthobiologics the bridge between basic science and clinical advancements in fracture healing. *Organogenesis* (2012). doi:10.4161/org.23306
103. Lee, K. S. *et al.* The role of osteoclast in resorption of hydroxyapatite and β-tricalcium phosphate coating layer. *Key Eng. Mater.* (2009).
104. Saikia, K. C. *et al.* Calcium phosphate ceramics as bone graft substitutes in filling bone tumor defects. *Indian J. Orthop.* (2008). doi:10.4103/0019-5413.39588
105. Wagoner Johnson, A. J. & Herschler, B. A. A review of the mechanical behavior of CaP

and CaP/polymer composites for applications in bone replacement and repair. *Acta Biomaterialia* (2011). doi:10.1016/j.actbio.2010.07.012
106. Koshino, T., Murase, T., Takagi, T. & Saito, T. New bone formation around porous hydroxyapatite wedge implanted in opening wedge high tibial osteotomy in patients with osteoarthritis. *Biomaterials* (2001). doi:10.1016/S0142-9612(00)00318-5
107. Galois, L. & Mainard, D. Bone ingrowth into two porous ceramics with different pore sizes: An experimental study. *Acta Orthop. Belg.* (2004).
108. Spivak, J. M. & Hasharoni, A. Use of hydroxyapatite in spine surgery. *Eur. Spine J.* (2001). doi:10.1007/s005860100286
109. Ciardelli, G. *et al.* Blends of poly-(ε-caprolactone) and polysaccharides in tissue engineering applications. *Biomacromolecules* (2005). doi:10.1021/bm0500805
110. Pina, S., Oliveira, J. M. & Reis, R. L. Natural-based nanocomposites for bone tissue engineering and regenerative medicine: A review. *Advanced Materials* (2015). doi:10.1002/adma.201403354
111. Chae, T., Yang, H., Leung, V., Ko, F. & Troczynski, T. Novel biomimetic hydroxyapatite/alginate nanocomposite fibrous scaffolds for bone tissue regeneration. *J. Mater. Sci. Mater. Med.* (2013). doi:10.1007/s10856-013-4957-7
112. Talley, A. D., Boller, L. A., Kalpakci, K. N., Shimko, D. A. & Guelcher, C. S. A. Injectable , compression - resistant polymer / ceramic composite bone grafts promote lateral ridge augmentation without protective mesh in a canine model. *Clin. Oral Implants Res.* 592–602 (2018). doi:10.1111/clr.13257
113. Fu, S. Z. *et al.* Injectable and thermo-sensitive PEG-PCL-PEG copolymer/collagen/n-HA hydrogel composite for guided bone regeneration. *Biomaterials* (2012). doi:10.1016/j.biomaterials.2012.03.040
114. Frohbergh, M. E. *et al.* Electrospun hydroxyapatite-containing chitosan nanofibers crosslinked with genipin for bone tissue engineering. *Biomaterials* (2012). doi:10.1016/j.biomaterials.2012.09.009
115. Gaharwar, A. K., Dammu, S. A., Canter, J. M., Wu, C. J. & Schmidt, G. Highly extensible, tough, and elastomeric nanocomposite hydrogels from poly(ethylene glycol) and hydroxyapatite nanoparticles. *Biomacromolecules* (2011). doi:10.1021/bm200027z
116. Gleeson, J. P., Plunkett, N. A. & O'Brien, F. J. Addition of hydroxyapatite improves stiffness, interconnectivity and osteogenic potential of a highly porous collagen-based scaffold for bone tissue regeneration. *Eur. Cells Mater.* (2010). doi:10.22203/eCM.v020a18
117. Kane, R. J. *et al.* Hydroxyapatite reinforced collagen scaffolds with improved architecture and mechanical properties. *Acta Biomater.* (2015). doi:10.1016/j.actbio.2015.01.031
118. Kim, H. W., Knowles, J. C. & Kim, H. E. Effect of biphasic calcium phosphates on drug release and biological and mechanical properties of poly(ε-caprolactone) composite membranes. *J. Biomed. Mater. Res. - Part A* (2004). doi:10.1002/jbm.a.30100
119. Petricca, S. E., Marra, K. G. & Kumta, P. N. Chemical synthesis of poly(lactic-co-glycolic acid)/hydroxyapatite composites for orthopaedic applications. *Acta Biomater.* (2006). doi:10.1016/j.actbio.2005.12.004
120. Zhang, P., Hong, Z., Yu, T., Chen, X. & Jing, X. In vivo mineralization and osteogenesis of nanocomposite scaffold of poly(lactide-co-glycolide) and hydroxyapatite surface-grafted with poly(l-lactide). *Biomaterials* (2009). doi:10.1016/j.biomaterials.2008.08.041
121. Dong, Z., Li, Y. & Zou, Q. Degradation and biocompatibility of porous nano-

hydroxyapatite/polyurethane composite scaffold for bone tissue engineering. *Appl. Surf. Sci.* (2009). doi:10.1016/j.apsusc.2009.01.083
122. Laschke, M. W., Strohe, A., Menger, M. D., Alini, M. & Eglin, D. In vitro and in vivo evaluation of a novel nanosize hydroxyapatite particles/poly(ester-urethane) composite scaffold for bone tissue engineering. *Acta Biomater.* (2010). doi:10.1016/j.actbio.2009.12.004
123. Kong, L. *et al.* Preparation and characterization of nano-hydroxyapatite/chitosan composite scaffolds. *J. Biomed. Mater. Res. - Part A* (2005). doi:10.1002/jbm.a.30414
124. Wahl, D. A. & Czernuszka, J. T. Collagen-hydroxyapatite composites for hard tissue repair. *European Cells and Materials* (2006). doi:10.22203/eCM.v011a06
125. Cunniffe, G. M., Dickson, G. R., Partap, S., Stanton, K. T. & O'Brien, F. J. Development and characterisation of a collagen nano-hydroxyapatite composite scaffold for bone tissue engineering. *J. Mater. Sci. Mater. Med.* (2010). doi:10.1007/s10856-009-3964-1
126. Meskinfam, M. *et al.* Polyurethane foam/nano hydroxyapatite composite as a suitable scaffold for bone tissue regeneration. *Mater. Sci. Eng. C* (2018). doi:10.1016/j.msec.2017.08.064
127. Lu, S. *et al.* Settable polymer/ceramic composite bone grafts stabilize weight-bearing tibial plateau slot defects and integrate with host bone in an ovine model. *Biomaterials* **179**, 29–45 (2018).
128. Guelcher, S. A. Biodegradable Polyurethanes: Synthesis and Applications in Regenerative Medicine. *Tissue Eng. Part B Rev.* **14**, 3–17 (2008).
129. Guelcher, S. A. *et al.* Synthesis, mechanical properties, biocompatibility, and biodegradation of polyurethane networks from lysine polyisocyanates. *Biomaterials* (2008). doi:10.1016/j.biomaterials.2007.12.046
130. Shiels, S. M. *et al.* Injectable and compression-resistant low-viscosity polymer/ceramic composite carriers for rhBMP-2 in a rabbit model of posterolateral fusion: A pilot study. *J. Orthop. Surg. Res.* (2017). doi:10.1186/s13018-017-0613-0
131. Talley, A. D. *et al.* Effects of Recombinant Human Bone Morphogenetic Protein-2 Dose and Ceramic Composition on New Bone Formation and Space Maintenance in a Canine Mandibular Ridge Saddle Defect Model. *Tissue Eng. Part A* **22**, 469–479 (2016).
132. Hafeman, A. E. *et al.* Characterization of the degradation mechanisms of lysine-derived aliphatic poly(ester urethane) scaffolds. *Biomaterials* **32**, 419–429 (2011).
133. Zanetta, M. *et al.* Ability of polyurethane foams to support cell proliferation and the differentiation of MSCs into osteoblasts. *Acta Biomater.* (2009). doi:10.1016/j.actbio.2008.12.003
134. Marzec, M., Kucińska-Lipka, J., Kalaszczyńska, I. & Janik, H. Development of polyurethanes for bone repair. *Materials Science and Engineering C* (2017). doi:10.1016/j.msec.2017.07.047
135. Fernando, S., McEnery, M. & Guelcher, S. A. Polyurethanes for Bone Tissue Engineering. in *Advances in Polyurethane Biomaterials* (2016). doi:10.1016/B978-0-08-100614-6.00016-0
136. Benoit, F. M. Degradation of polyurethane foams used in the mêcme breast implant. *J. Biomed. Mater. Res.* (1993). doi:10.1002/jbm.820271014
137. Szycher, M. Biostability of Polyurethane Elastomers: A Critical Review. *Journal of Biomaterials Applications* (1988). doi:10.1177/088532828800300207
138. Van Maris, R., Tamano, Y., Yoshimura, H. & Gay, K. M. Polyurethane catalysis by

tertiary amines. *J. Cell. Plast.* (2005). doi:10.1177/0021955X05055113
139. McEnery, M. A. P. *et al.* Oxidatively degradable poly(thioketal urethane)/ceramic composite bone cements with bone-like strength. *RSC Adv.* **6**, 109414–109424 (2016).
140. McGough, M. A. P. *et al.* Nanocrystalline Hydroxyapatite-Poly(thioketal urethane) Nanocomposites Stimulate a Combined Intramembranous and Endochondral Ossification Response in Rabbits. *ACS Biomater. Sci. Eng.* **6**, 564–574 (2020).
141. McGough, M. *et al.* Poly(thioketal urethane) Autograft Extenders in an Intertransverse Process Model of Bone Formation. *Tissue Eng. Part A* (2018).
142. Martin, J. R. *et al.* A porous tissue engineering scaffold selectively degraded by cell-generated reactive oxygen species. *Biomaterials* (2014). doi:10.1016/j.biomaterials.2014.01.026
143. Patil, P. *et al.* Porcine Ischemic Wound-Healing Model for Preclinical Testing of Degradable Biomaterials. *Tissue Eng. Part C Methods* (2017). doi:10.1089/ten.tec.2017.0202
144. Martin, J. R. *et al.* Local Delivery of PHD2 siRNA from ROS-Degradable Scaffolds to Promote Diabetic Wound Healing. *Adv. Healthc. Mater.* (2016). doi:10.1002/adhm.201600820
145. Polo-Corrales, L., Latorre-Esteves, M. & Ramirez-Vick, J. E. Scaffold design for bone regeneration. *Journal of Nanoscience and Nanotechnology* (2014). doi:10.1166/jnn.2014.9127
146. Kneser, U., Schaefer, D. J., Polykandriotis, E. & Horch, R. E. Tissue engineering of bone: The reconstructive surgeon's point of view. *Journal of Cellular and Molecular Medicine* (2006). doi:10.1111/j.1582-4934.2006.tb00287.x
147. Kaigler, D., Wang, Z., Horger, K., Mooney, D. J. & Krebsbach, P. H. VEGF scaffolds enhance angiogenesis and bone regeneration in irradiated osseous defects. *J. Bone Miner. Res.* (2006). doi:10.1359/jbmr.060120
148. Eckardt, H. *et al.* Recombinant human vascular endothelial growth factor enhaces bone healing in an experimental nonunion model. *J. Bone Jt. Surg. - Ser. B* (2005). doi:10.1302/0301-620X.87B10.16226
149. Kent Leach, J., Kaigler, D., Wang, Z., Krebsbach, P. H. & Mooney, D. J. Coating of VEGF-releasing scaffolds with bioactive glass for angiogenesis and bone regeneration. *Biomaterials* (2006). doi:10.1016/j.biomaterials.2006.01.033
150. Keramaris, N. C., Calori, G. M., Nikolaou, V. S., Schemitsch, E. H. & Giannoudis, P. V. Fracture vascularity and bone healing: A systematic review of the role of VEGF. *Injury* (2008). doi:10.1016/S0020-1383(08)70015-9
151. Gerstenfeld, L. C., Cullinane, D. M., Barnes, G. L., Graves, D. T. & Einhorn, T. A. Fracture healing as a post-natal developmental process: Molecular, spatial, and temporal aspects of its regulation. *J. Cell. Biochem.* (2003). doi:10.1002/jcb.10435
152. Xie, H. *et al.* PDGF-BB secreted by preosteoclasts induces angiogenesis during coupling with osteogenesis. *Nat. Med.* (2014). doi:10.1038/nm.3668
153. Kawaguchi, H. *et al.* A local application of recombinant human fibroblast growth factor 2 for tibial shaft fractures: A randomized, placebo-controlled trial. *J. Bone Miner. Res.* (2010). doi:10.1002/jbmr.146
154. Kawaguchi, H. *et al.* Acceleration of fracture healing in nonhuman primates by fibroblast growth factor-2. *J. Clin. Endocrinol. Metab.* (2001). doi:10.1210/jcem.86.2.7199
155. Lind, M. *et al.* Transforming growth factor-β enhances fracture healing in rabbit tibiae.

*Acta Orthop.* (1993). doi:10.3109/17453679308993691
156. Tsiridis, E., Upadhyay, N. & Giannoudis, P. Molecular aspects of fracture healing:Which are the important molecules? *Injury* (2007). doi:10.1016/j.injury.2007.02.006
157. Andrew, J. G., Hoyland, J., Freemont, A. J. & Marsh, D. Insulinlike growth factor gene expression in human fracture callus. *Calcified Tissue International* (1993). doi:10.1007/BF01321886
158. Lee, Y. *et al.* The bone regenerative effect of platelet-derived growth factor-BB delivered with a chitosan/tricalcium phosphate sponge carrier. *J Periodontol* **7**, 418–24 (2000).
159. Ogilvie, C. M. *et al.* Vascular endothelial growth factor improves bone repair in a murine nonunion model. *Iowa Orthop. J.* (2012).
160. Reible, B., Schmidmaier, G., Moghaddam, A. & Westhauser, F. Insulin-like growth factor-1 as a possible alternative to bone morphogenetic protein-7 to induce osteogenic differentiation of human mesenchymal stem cells in vitro. *Int. J. Mol. Sci.* (2018). doi:10.3390/ijms19061674
161. Gronowicz, G. *et al.* Calvarial bone regeneration is enhanced by sequential delivery of fgf-2 and bmp-2 from layer-by-layer coatings with a biomimetic calcium phosphate barrier layer. *Tissue Eng. - Part A* (2017). doi:10.1089/ten.tea.2017.0111
162. Nagayasu-Tanaka, T. *et al.* Action mechanism of fibroblast growth factor-2 (FGF-2) in the promotion of periodontal regeneration in beagle dogs. *PLoS One* (2015). doi:10.1371/journal.pone.0131870
163. Urist, M. R. Bone: Formation by Autoinduction. *Science (80-. ).* **150**, 893–899 (1965).
164. Urist, M. R. & Strates, B. S. Bone morphogenetic protein. *J Dent Res* **50**, 1392–1406 (1971).
165. Spector, J. A. *et al.* Expression of bone morphogenetic proteins during membranous bone healing. *Plast. Reconstr. Surg.* **107**, 124–34 (2001).
166. McKay, W. F., Peckham, S. M. & Badura, J. M. A comprehensive clinical review of recombinant human bone morphogenetic protein-2 (INFUSE® Bone Graft). *Int. Orthop.* **31**, 729–734 (2007).
167. Herford, A. S. *et al.* Recombinant human bone morphogenetic protein 2 combined with an osteoconductive bulking agent for mandibular continuity defects in nonhuman primates. *J. Oral Maxillofac. Surg.* **70**, 703–716 (2012).
168. Garcia, J. *et al.* Effect of membrane exposure on guided bone regeneration: A systematic review and meta-analysis. *Clin. Oral Implants Res.* **29**, 328–338 (2018).
169. Rakhmatia, Y. D., Ayukawa, Y., Furuhashi, A. & Koyano, K. Current barrier membranes: Titanium mesh and other membranes for guided bone regeneration in dental applications. *Journal of Prosthodontic Research* **57**, 3–14 (2013).
170. Perri, B., Cooper, M., Lauryssen, C. & Anand, N. Adverse swelling associated with use of rh-BMP-2 in anterior cervical discectomy and fusion: a case study. *Spine J.* **7**, 235–239 (2007).
171. Wong, D. A., Kumar, A., Jatana, S., Ghiselli, G. & Wong, K. Neurologic impairment from ectopic bone in the lumbar canal: a potential complication of off-label PLIF/TLIF use of bone morphogenetic protein-2 (BMP-2). *Spine J.* **8**, 1011–1018 (2008).
172. Smucker, J. D., Rhee, J. M., Singh, K., Yoon, S. T. & Heller, J. G. Increased swelling complications associated with off-label usage of rhBMP-2 in the anterior cervical spine. *Spine (Phila. Pa. 1976).* **31**, 2813–2819 (2006).
173. Tannoury, C. A. & An, H. S. Complications with the use of bone morphogenetic protein 2

(BMP-2) in spine surgery. *Spine J.* **14**, 552–559 (2014).
174. White, A. P. *et al.* Clinical applications of BMP-7/OP-1 in fractures, nonunions and spinal fusion. *International Orthopaedics* (2007). doi:10.1007/s00264-007-0422-x
175. Perez, J. R. *et al.* Tissue Engineering and Cell-Based Therapies for Fractures and Bone Defects. *Front. Bioeng. Biotechnol.* (2018). doi:10.3389/fbioe.2018.00105
176. Webster, T. J., Ergun, C., Doremus, R. H., Siegel, R. W. & Bizios, R. Enhanced functions of osteoblasts on nanophase ceramics. *Biomaterials* (2000). doi:10.1016/S0142-9612(00)00075-2
177. Zuk, P. A. *et al.* Multilineage cells from human adipose tissue: Implications for cell-based therapies. in *Tissue Engineering* (2001). doi:10.1089/107632701300062859
178. Salingcarnboriboon, R. *et al.* Establishment of tendon-derived cell lines exhibiting pluripotent mesenchymal stem cell-like property. *Exp. Cell Res.* (2003). doi:10.1016/S0014-4827(03)00107-1
179. Seo, B. M. *et al.* Investigation of multipotent postnatal stem cells from human periodontal ligament. *Lancet* (2004). doi:10.1016/S0140-6736(04)16627-0
180. Wexler, S. A. *et al.* Adult bone marrow is a rich source of human mesenchymal 'stem' cells but umbilical cord and mobilized adult blood are not. *Br. J. Haematol.* (2003). doi:10.1046/j.1365-2141.2003.04284.x
181. Thomson, J. A. Embryonic stem cell lines derived from human blastocysts. *Science (80-. ).* (1998). doi:10.1126/science.282.5391.1145
182. Schallmoser, K. *et al.* Platelet-derived growth factors for GMP-compliant propagation of mesenchymal stromal cells. *Biomed. Mater. Eng.* (2009). doi:10.3233/BME-2009-0591
183. Sensebé, L., Gadelorge, M. & Fleury-Cappellesso, S. Production of mesenchymal stromal/stem cells according to good manufacturing practices: A review. *Stem Cell Research and Therapy* (2013). doi:10.1186/scrt217
184. Stegemann, J. P. *et al.* Cell therapy for bone repair: Narrowing the gap between vision and practice. *Eur. Cells Mater.* (2014). doi:10.22203/eCM.v027sa01
185. Giannoni, P. *et al.* Short-time survival and engraftment of bone marrow stromal cells in an ectopic model of bone regeneration. in *Tissue Engineering - Part A* (2010). doi:10.1089/ten.tea.2009.0041
186. Becquart, P. *et al.* Ischemia is the prime but not the only cause of human multipotent stromal cell death in tissue-engineered constructs in vivo. *Tissue Eng. - Part A* (2012). doi:10.1089/ten.tea.2011.0690
187. Kaempfen, A. *et al.* Engraftment of prevascularized, tissue engineered constructs in a novel rabbit segmental bone defect model. *Int. J. Mol. Sci.* (2015). doi:10.3390/ijms160612616
188. Albert, B. *et al.* Intrinsic osteoinduction of biomimetic nanostructured calcium phosphate scaffolds. *Front. Bioeng. Biotechnol.* (2016). doi:10.3389/conf.fbioe.2016.01.00698
189. Kubinová, Š. & Syková, E. Nanotechnologies in regenerative medicine. *Minimally Invasive Therapy and Allied Technologies* (2010). doi:10.3109/13645706.2010.481398
190. Wahajuddin & Arora, S. Superparamagnetic iron oxide nanoparticles: Magnetic nanoplatforms as drug carriers. *International Journal of Nanomedicine* (2012). doi:10.2147/IJN.S30320
191. Davis, H. & Leach, J. Hybrid and Composite Biomaterials in Tissue Engineering. *Top. Multifunct. Biomater. devices* (2008).
192. Lu, S. *et al.* Resorbable nanocomposites with bone-like strength and enhanced cellular

activity. *J. Mater. Chem. B* **5**, 4198–4206 (2017).
193. Fang, L., Leng, Y. & Gao, P. Processing and mechanical properties of HA/UHMWPE nanocomposites. *Biomaterials* (2006). doi:10.1016/j.biomaterials.2006.02.023
194. Hong, Z. *et al.* Nano-composite of poly(L-lactide) and surface grafted hydroxyapatite: Mechanical properties and biocompatibility. *Biomaterials* (2005). doi:10.1016/j.biomaterials.2005.04.018
195. Katz, E. & Willner, I. Integrated nanoparticle-biomolecule hybrid systems: Synthesis, properties, and applications. *Angewandte Chemie - International Edition* (2004). doi:10.1002/anie.200400651
196. Yi, H., Ur Rehman, F., Zhao, C., Liu, B. & He, N. Recent advances in nano scaffolds for bone repair. *Bone Res.* (2016). doi:10.1038/boneres.2016.50
197. Epstein, N. Complications due to the use of BMP/INFUSE in spine surgery: The evidence continues to mount. *Surg. Neurol. Int.* (2013). doi:10.4103/2152-7806.114813
198. Boden, S. D. Biology of lumbar spine fusion and use of bone graft substitutes: Present, future, and next generation. in *Tissue Engineering* (2000). doi:10.1089/107632700418092
199. Gunzburg, R. & Szpalski, M. Use of a novel β-tricalcium phosphate - Based bone void filler as a graft extender in spinal fusion surgeries. *Orthopedics* (2002). doi:10.1016/j.psychsport.2009.03.001
200. Lerner, T., Bullmann, V., Schulte, T. L., Schneider, M. & Liljenqvist, U. A level-1 pilot study to evaluate of ultraporous β-tricalcium phosphate as a graft extender in the posterior correction of adolescent idiopathic scoliosis. *Eur. Spine J.* (2009). doi:10.1007/s00586-008-0844-1
201. Rantakokko, J. *et al.* Posterolateral spondylodesis using bioactive glass S53P4 and autogenous bone in instrumented unstable lumbar spine burst fractures. A prospective 10-year follow-up study. *Scand J Surg* (2012). doi:10.1177/145749691210100113
202. Walsh, W. R. *et al.* Application of Resorbable Poly(Lactide- *co* -Glycolide) with Entangled Hyaluronic Acid as an Autograft Extender for Posterolateral Intertransverse Lumbar Fusion in Rabbits. *Tissue Eng. Part A* (2011). doi:10.1089/ten.TEA.2010.0008
203. McGough, M. A. *et al.* Poly (Thioketal Urethane) Autograft Extenders in an Intertransverse Process Model of Bone Formation. *Tissue Eng. Part A* (2019).
204. Muschler, G. F., Raut, V. P., Patterson, T. E., Wenke, J. C. & Hollinger, J. O. The design and use of animal models for translational research in bone tissue engineering and regenerative medicine. *Tissue Engineering - Part B: Reviews* (2010). doi:10.1089/ten.teb.2009.0658
205. Aerssens, J., Boonen, S., Lowet, G. & Dequeker, J. Interspecies differences in bone composition, density, and quality: Potential implications for in vivo bone research. *Endocrinology* (1998). doi:10.1210/endo.139.2.5751
206. Center for Drug Evaluation and Research. Guidance for Industry: Estimating the Maximum Safe Starting Dose in Initial Clinical Trials for Therapeutics in Adult Healthy Volunteers. *US Dep. Heal. Hum. Serv.* (2005).
207. Scarano, A., Petrone, G. & Piattelli, A. Staining Techniques for Plastic-Embedded Specimens. in *Handbook of Histology Methods for Bone and Cartilage* (2003). doi:10.1007/978-1-59259-417-7_23
208. Del Cerro, M., Cogen, J. & Del Cerro, C. Stevenel's Blue, an excellent stain for optical microscopical study of plastic embedded tissues. *Microsc. Acta* (1980).
209. van Gaalen, S. M. *et al.* Use of fluorochrome labels in in vivo bone tissue engineering

research. *Tissue engineering. Part B, Reviews* (2010). doi:10.1089/ten.teb.2009.0503
210. Dey, P. Decalcification of Bony and Hard Tissue for Histopathology Processing. in *Basic and Advanced Laboratory Techniques in Histopathology and Cytology* (2018). doi:10.1007/978-981-10-8252-8_4
211. Dyment, N. A. *et al.* High-throughput, multi-image cryohistology of mineralized tissues. *J. Vis. Exp.* (2016). doi:10.3791/54468
212. Gerstenfeld, L. C., Wronski, T. J., Hollinger, J. O. & Einhorn, T. A. Application of histomorphometric methods to the study of bone repair. *Journal of Bone and Mineral Research* (2005). doi:10.1359/JBMR.050702
213. Parfitt, A. M. Bone histomorphometry: Standardization of nomenclature, symbols and units (summary of proposed system). *Bone* (1988). doi:10.1016/8756-3282(88)90029-4
214. Campbell, G. M. & Sophocleous, A. Quantitative analysis of bone and soft tissue by micro-computed tomography: applications to ex vivo and in vivo studies. *Bonekey Rep.* (2014). doi:10.1038/bonekey.2014.59
215. Bouxsein, M. L. *et al.* Guidelines for assessment of bone microstructure in rodents using micro-computed tomography. *Journal of Bone and Mineral Research* (2010). doi:10.1002/jbmr.141

# CHAPTER III

# CHAPTER 3: COMPRESSION-RESISTANT POLYMER/CERAMIC COMPOSITE SCAFFOLDS AUGMENTED WITH rhBMP-2 PROMOTE NEW BONE FORMATION IN A NON-HUMAN PRIMATE MANDIBULAR RIDGE AUGMENTATION MODEL

**Adapted with permission from The International Journal of Oral Maxillofacial Implants:**

**Boller LA**, Jones AA, Cochran DL, Guelcher SA. Compression-Resistant Polymer/Ceramic Composite Scaffolds Augmented with rhBMP-2 Promote New Bone Formation in a Nonhuman Primate Mandibular Ridge Augmentation Model. *Int J Oral Maxillofac Implants*. 2020;35(3):616-624.

## 3.1 Abstract

This study was designed to test the hypothesis that compression-resistant (CR) scaffolds augmented with recombinant human bone morphogenetic protein-2 (rhBMP-2) at clinically relevant doses in a non-human primate lateral ridge augmentation model enhances bone formation in a dose-responsive manner without additional protective membranes. Defects (15 mm long x 8 mm wide x 5 mm deep) were created bilaterally in the mandible of 9 hamadryas baboons. The defect sites were implanted with poly (ester urethane) (PEUR)/ceramic CR scaffolds with 0.75mg/ml rhBMP-2 (CR-L), 1.5mg/ml rhBMP-2 (CR-H), or control CR scaffolds without rhBMP-2 (CR). The primary outcome of ridge width and secondary outcomes of new bone formation, cellular infiltration, and integration with host bone were evaluated using histology, histomorphometry, and μCT at 16 weeks following implantation. New bone formation in the mandible was observed in a dose-responsive manner. CR-H promoted significantly greater new bone formation compared with the CR group. In all groups, ridge width was maintained without an additional protective membrane. CR scaffolds augmented with a clinically relevant dose of rhBMP-2 (1.5mg/ml) promoted significant new bone formation. These results suggest that a compression-resistant PEUR/ceramic composite scaffold without a protective membrane may be a potential new rhBMP-2 carrier for clinical use.

# CHAPTER III

## 3.2 Introduction

Dental implants are frequently used to restore dentition. However, mandibular reconstruction is often necessary to enhance bone volume prior to dental implants. A number of materials have been utilized for ridge augmentation, but autograft remains the gold standard. However, complications associated with autograft including donor site morbidity, limited quantity, poor vascularization, and potential failure to integrate with host bone preclude its use.[1,2] These limitations have led to the development of scaffolds augmented with growth factors for ridge reconstruction.[3,4]

Bone morphogenetic proteins (BMPs) were first discovered as osteoinductive growth factors by Urist.[5] Of the many known BMPs, BMP-2 plays a critical role in bone formation.[6] Processes have been developed for the manufacture of recombinant human BMP-2 (rhBMP-2) and its subsequent clinical use.[7] Absorbable collagen sponge (ACS) rhBMP-2 carriers are an FDA-approved treatment (INFUSE® bone graft, Medtronic) for posterior-lateral spinal fusion, tibial fractures, sinus lift procedures, and extraction socket defects.[8] However, the ACS carrier is unable to withstand compressive forces and requires the use of either resorbable (collagen, polylactic acid, polyglycolic acid) or non-resorbable membranes (e-PTFE, titanium mesh). Both resorbable and non-resorbable membranes have limitations including wound dehiscence and healing complications.[9] Additionally, resorbable membranes cause swelling and inflammation concerns while non-resorbable membranes must be subsequently removed.[10]

The successful use of rhBMP-2 in ridge augmentation is dependent on both the properties of the carrier and protein concentration.[11] The ideal carrier is resorbable and optimizes predictable bone formation through controlled release of rhBMP-2 and space maintenance. Resorbable lysine-derived poly(ester urethane) (PEUR) scaffolds are promising carriers that have been frequently

utilized for bone grafting applications.[12,13] The addition of ceramic particles to PEUR scaffolds has shown improved mechanical properties and osteoconductivity.[14] Compression-resistant (CR) PEUR/ceramic composite scaffolds have previously been shown to enhance bone formation in femoral condyle plug defects in sheep.[15]

In both a canine mandibular saddle defect[16] and lateral ridge defect[17] model, rhBMP-2-augmented CR PEUR/ceramic composite scaffolds promoted new bone formation without the use of a membrane. However, the demonstration of bone formation utilizing CR composite carriers augmented with clinically relevant rhBMP-2 doses in primates is essential prior to its use in humans.[18] The purpose of this study was to test the hypothesis that CR composites without membranes maintain ridge width and promote new bone formation in a dose-responsive manner in a non-human primate model. CR scaffolds incorporating clinically relevant doses (0, 0.75, or 1.5 mg/ml) of rhBMP-2 were evaluated in a non-human primate lateral ridge augmentation model. The primary outcome of ridge width and secondary outcomes of new bone formation, cellular infiltration, and integration with host bone were evaluated with histology, histomorphometry, and μCT at 16 weeks post-operatively.

## 3.3 Materials and Methods

*Materials.* Lysine triisocyanate (LTI)-poly (ethylene glycol) (PEG) prepolymer was acquired from Ricerca Biosciences LLC. Glycerol, ε-caprolactone, stannous octoate, APTES triethylene diamine, and dipropylene glycol were purchased from Sigma-Aldrich (St. Louis, MO) and utilized for polyester triol synthesis. Glycolide and DL-lactide were also used in the polyester triol synthesis and were purchased from Polysciences (Warrington, PA). Medtronic Spinal (Memphis, TN) supplied rhBMP-2 and ceramic (CM) (15% hydroxyapatite, 85% beta tricalcium phosphate) granules. CM granules ranged from 100-500 μm for improved handling properties.

*Polyester triol synthesis.* The polyester triol was synthesized following a previously published method.[19,20] A 10% (w/w) solution was made using triethylene diamine and dipropylene glycol. Briefly, glycerol, ε-caprolactone, glycolide, and DL-lactide monomers were mixed for 40h under argon at 140°C to yield a viscous fluid. The resulting fluid was hexane-rinsed (3X) and dried under vacuum at 80°C for 48 h. The synthesized polyester had a molecular weight of 450 g $mol^{-1}$, and the backbone consisted of 70% ε-caprolactone, 20% glycolide, and 10% DL-lactide.

*Compression-resistant (CR) scaffold fabrication.* The CR scaffolds were fabricated as described previously.[17] Prior to the study, CR scaffold materials were gamma-irradiated using a dose of 25 kGY. Immediately prior to scaffold implantation within the defect, CM particles (45 wt%), lyophilized rhBMP-2, polyester triol, triethylene diamine (1.1 pphp), and LTI-PEG were mixed for 60s by hand in a 5-mL mixing cup. The NCO:OH index was set at 115 (15% excess NCO). An index of 115 produces a sufficiently cured foam and was selected to account for additional OH groups arising from the presence of blood and water within the defect space upon injection of the reactive scaffold.[21]

*Animals*. Utilizing the ridge width outcomes from our previous canine study[17], a power analysis for this non-human primate study was performed with an assumed effect size of >0.78, a power of 80%, and alpha of 0.05 to determine the sample size of 6 per group. Therefore, 9 papio hamadryas baboons (two implants per animal) were used to test the hypothesis that CR-H promotes the highest ridge width. This number of animals is consistent with previous ridge augmentation studies evaluating rhBMP-2 in non-human primates.[22–24] Skeletally mature males and females (5 males, ~23 kg, and 4 females, ~15 kg) of average weight were selected. The Institutional Animal Care and Use Committee of the Mannheimer Foundation and the ACURO of the US Army approved this study. Surgical and care procedures were performed in compliance with the Animal

Welfare Act, Animal Welfare Regulations, and the Guide for the Care and Use of Laboratory Animals.

*Pre- and postoperative care.* Prior to and following surgical procedures, the animals were kept in separate cages. All surgical procedures were performed under general anesthesia in a sterile operating room. Animals were given antibiotic ampicillin (5 mg/kg) and sustained release opioid buprenorphine (0.2 mg/kg) prior to surgery. An intravenous injection of ketamine (10 mg/kg) and glycopyrrolate (0.004 mg/kg) were used to induce general anesthesia, and an endotracheal tube was placed to maintain general anesthesia with isoflurane (approximately 0.5-4%) in oxygen to effect. Postoperatively, antibiotic enrofloxacin (5mg/kg) and meloxicam (0.1 mg/kg) for pain control were administered via intramuscular injection and subcutaneously, respectively, for 7 days. Additionally, extraction sites were inspected and flushed with Nolvadent. Following the procedures, the animals received soft food twice daily and had *ad libitum* access to water.

*Surgery 1 (Extraction and Defect Creation).* To prepare the alveolar ridge defect, incisions were made by full mucoperiosteal flap reflection. A separating disk was used to ease root extraction of all two-rooted teeth prior to removal. The buccal bone plate was removed to create a defect measuring approximately (length 15 mm, height 8 mm, depth 5 mm), and the defect margins were outlined utilizing a small round burr. Sterile saline irrigation was performed with all drilling. Flaps were closed with sutures. Each animal obtained bilateral defects.

*Surgery 2 (Ridge Augmentation).* The extraction sites were accessed and debrided after a 3-month healing period. All granulation tissue was removed from the defect site, and defect margins were redefined to ensure that the defects measured approximately 15-16 mm mesiodistally, 8-9 mm apico-coronally, and 5-6 mm bucco-lingually (**Figure 3.1A)**. Lyopholized rhBMP-2 at no (0.0 mg/mL), Low (0.75 mg/mL), or High (1.5 mg/mL) dose was mixed with the

individual components of the CR scaffolds (*n*=6 per group) and injected into the defect site (**Figure 3.1B)**. Prior to suturing, the CR grafts cured within the defect space for roughly 10 min (**Figure 3.1C-D**). The primates received randomized animal IDs to randomize treatment groups such that each animal received a different treatment group in each defect.

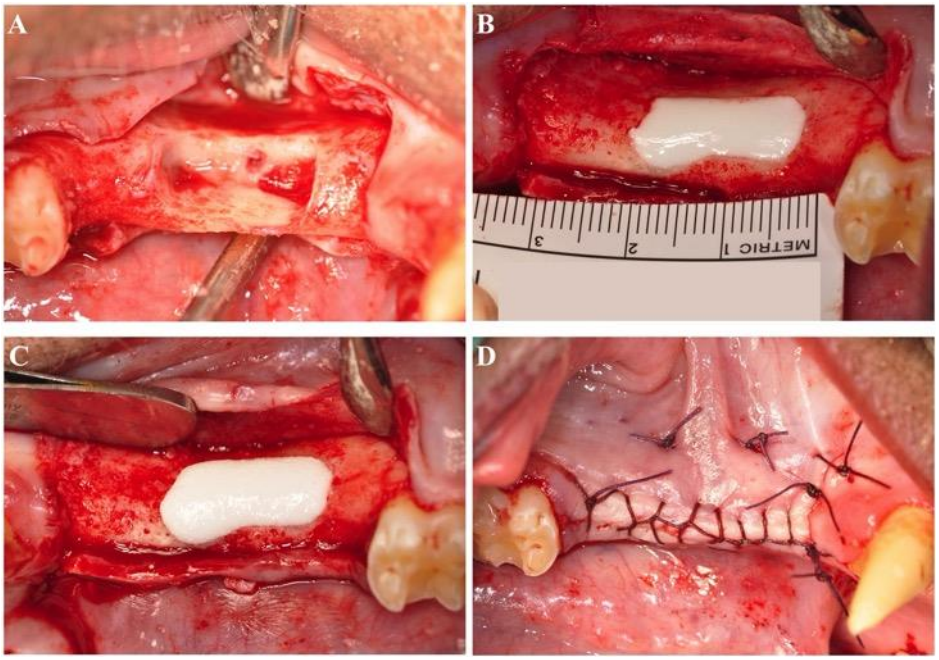


**Figure 3.1.** Surgical images. (A) Surgery to create lateral ridge defect. (B) CR immediately following injection into defect site. (C) Cured CR graft 10 minutes after injection. (D) Wound closure following graft placement.

*Sacrifice.* All animals were euthanized 16 weeks after the second surgery with an intravenous injection of pentobarbital Sodium (Fatal Plus®) (100 mg/kg body weight). The mandibles were extracted and fixed in formalin (10%) for two weeks.

*μCT Analysis.* After extraction, the fixed mandibles were analyzed using a μCT50 (SCANO Medical, Basserdorf Switzerland). Scans were performed at 70 kVp energy, 200 μA source current, 1000 projections per rotation, 800 ms integration time, and an isotropic voxel size of 17.2 μm. 3D reconstructions of the defect were generated from Scanco evaluation software in which a 100-slice region within the middle of the defect was contoured to quantitatively assess

bone formation. The total volume of new bone within the defect region was measured to calculate bone volume fraction (BV/TV).

*Histology.* Bone regeneration was assessed via non-decalcified histology.[25] After formalin fixation, samples were dehydrated with gradients of ethanol. Samples were then embedded in poly (methyl methacrylate) and allowed to polymerize for 7 days. Sections were cut from the center of each defect (bucco-lingually) with an Exakt band saw. Polished ground sections (<100μm) were stained with Sanderson's rapid bone stain to qualitatively assess cellular infiltration and bone regeneration.

*Histomorphometry.* Metamorph software (Version 7.0.1, Waltham, MA) was used to quantitatively analyze ridge width and new bone formation in the histological sections. Ridge width was measured as a function of height at the mid-section of the defect. The ridge was measured from the back wall of the defect in 2-mm increments from the coronal base of the defect and subsequently normalized to the width of the coronal base of the defect. The area of interest (AOI) for new bone formation was defined as a rectangle measuring 8 x 5 mm, corresponding with the initial defect size, where the AOI aligned with the sagittal wall and coronal base of the defect. New bone (red) and infiltrating cells (blue) were quantified within the AOI of each section utilizing Metamorph. Host bone integration, characterized by the amount of new bone formation along the host bone interface at the sagittal wall of the defect, was evaluated by measuring the amount of new bone extending into the defect space over a 1-mm distance along the sagittal wall of the defect.

*Statistical Analysis.* Summary statistics including mean and median values were calculated for each defect. The μCT and histomorphometric parameters were plotted as mean ± standard deviation and analyzed using a non-parametric Kruskal-Wallis test with Dunn's tests for pairwise

comparisons by GraphPad Prism 8.0 software (GraphPad Software). The p-values are reported for significant ($p < 0.05$) differences between groups.

## 3.4 Results

*Surgical outcomes.* The surgical procedures were uneventful. However, certain limitations exist when using non-human primates.[26] Despite pain care and monitoring, three grafts were removed by the primates between days 6-9 following the second surgery. These samples were excluded from analysis. Between days 9-14 post-op, some of the primates began to pick at their sutures, resulting in exposure of the implants. The presence or absence of the implants could not be confirmed from radiographs taken between days 14-21, and thus the possibility that the implants were either partially or fully removed by the animals cannot be excluded. However, all wounds fully healed, and no subsequent infections arose. One animal presented an abnormal defect in the right side of its mandible discovered upon the first surgical procedure. This sample was not included in the analysis. Ultimately, 14/18 samples were used for analysis.

*μCT Analysis.* μCT images obtained after 16 weeks show differences in healing between the treatment groups (**Figure 3.2A**). Representative images of the coronal planes revealed new bone present in all three groups. A significant difference in BV/TV (**Figure 3.2B**), calculated from 3D reconstructions of the mandible after 16 weeks, was observed between the CR-H group (83.83 ± 0.07 %) when compared with the CR group (59.31 ± 0.10 %) (**Table 3.1**).

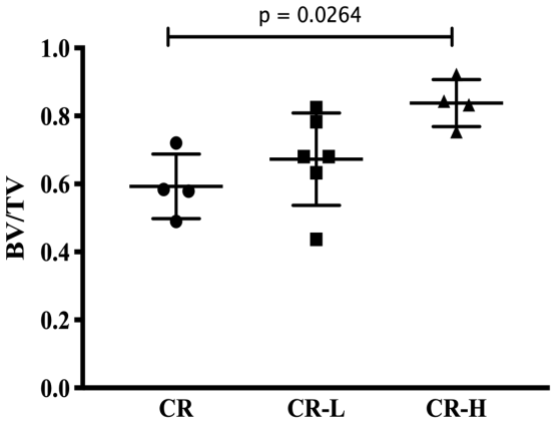


**Figure 3.2.** µCT analysis of new bone formation. Bone volume/ total volume (BV/TV) after 16 weeks for each of the treatment groups.

**Table 3.1.** Volumetric measurements of BV/TV by □CT at 16 weeks. *Significantly different compared with CR group using Dunn's test ($p<0.05$).

| Treatment Group | | BV/TV |
|---|---|---|
| CR | Mean ± SD<br>Median | 0.59 ± 0.10<br>0.58 |
| CR-L | Mean ± SD<br>Median<br>*p* | 0.67 ± 0.14<br>0.68<br>>0.999 |
| CR-H | Mean ± SD<br>Median<br>*p* | 0.84 ± 0.07*<br>0.84<br>0.0264 |

*Histological analysis.* Samples stained with Sanderson's rapid show new bone (red), cells (blue), and residual CM (black). The mandibles of the animals varied in overall volume due to the inclusion of both males and females in this study; however, the defect size and AOI were standardized in all animals regardless of sex. No evidence of inflammation was present within the defect space. New bone formation was seen in all groups, especially along the outer ridge (**Figure 3.3A**), but samples from the CR-H group exhibited the most uniform healing within the defect. High-magnification images (**Figure 3.3B**) showed new woven bone and new lamellar bone indicated by concentric lamellae. The CR group displayed more woven bone versus lamellar bone seen in the CR-L and CR-H groups.

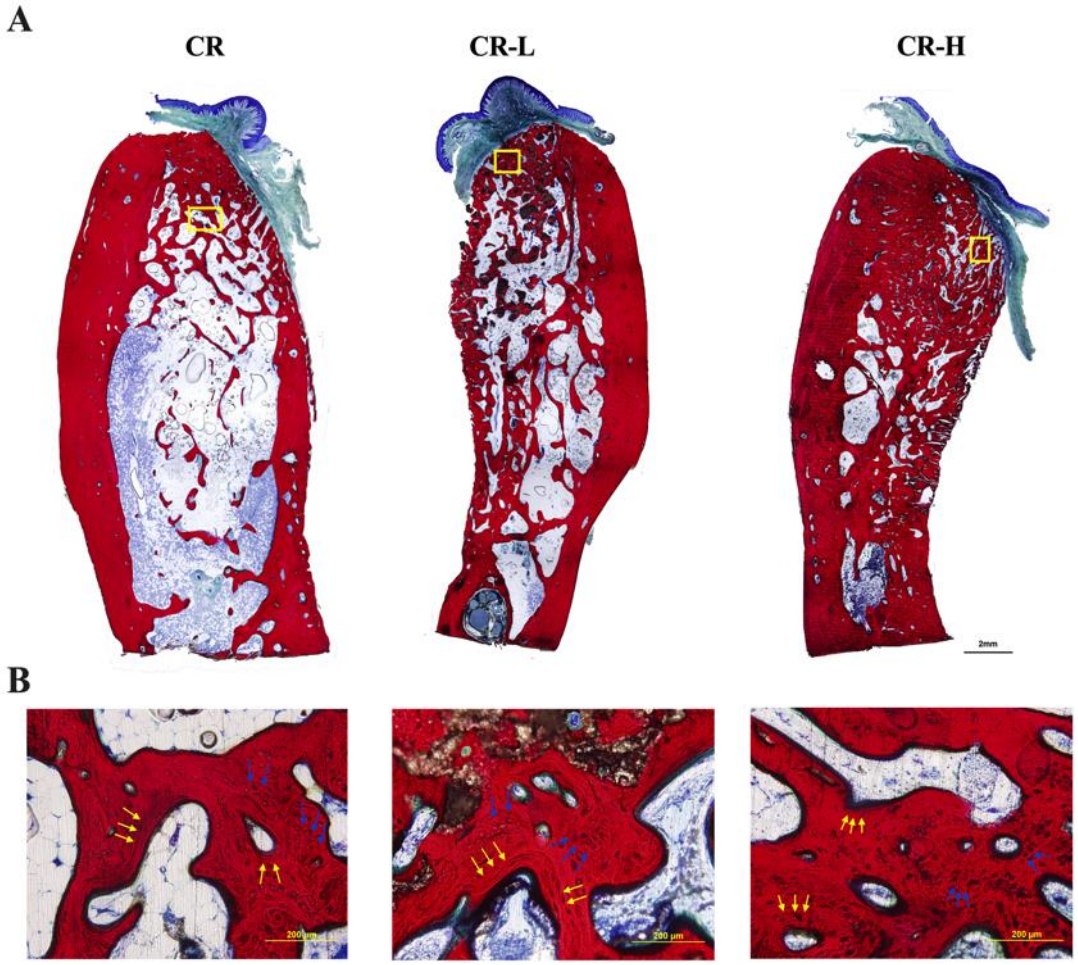


**Figure 3.3.** Representative images of histological sections. (A) Low- images (4X, 2mm scale bar) and (B) high-magnification (10X, 500µm scale bar) images display new bone (red), infiltrating cells (blue), and ceramic particles (black). Woven and lamellar bone is indicated by blue and yellow arrows, respectively.

*Histomorphometry*. The amount of new bone formation within the defects treated with CR, CR-L, and CR-H implants is listed in **Table 3.2**. Similar to the µCT results, histomorphometric analysis showed significant new bone in the CR-H group (68.3%) compared with the control group (43.9%) (**Figure 3.4A**). Comparatively, less new bone was seen in both the CR-L and CR groups. Cellular infiltration trended higher in both the CR-L and CR groups compared with the CR-H group, but the differences were not significant (**Figure 3.4B**). Integration of host bone with the implant was assessed by measuring the area% new bone near the periphery of the implant (1 mm distance from the sagittal wall of the defect). The area% new bone near the periphery was 55 -

82% (**Figure 3.4C**), which indicates that new bone grew into the implant resulting in its integration with the host bone. Ridge width as a function of ridge height was measured at 0, 2, 4, and 6 mm above the baseline of the defect (**Table 3.3**) for each sample. Ridge width was maintained in all of the groups (**Figure 3.4D)**.

**Table 3.2.** Area% (bone) and Area% (infiltrating cells) at 16 weeks measured histomorphometrically. *Significantly different compared with CR group using Dunn's test ($p<0.05$).

| | | Area% Bone | Area% Cells |
|---|---|---|---|
| CR | Mean ± SD<br>Median | 43.94 ± 5.45<br>53.38 | 13.31 ± 4.12<br>13.18 |
| CR-L | Mean ± SD<br>Median<br>*p* | 56.88 ± 12.3<br>59.18<br>0.3256 | 17.31 ± 9.98<br>14.62<br>>0.999 |
| CR-H | Mean ± SD<br>Median<br>*p* | 68.27 ± 8.19*<br>66.99<br>0.0337 | 7.83 ± 4.01<br>7.94<br>0.6147 |

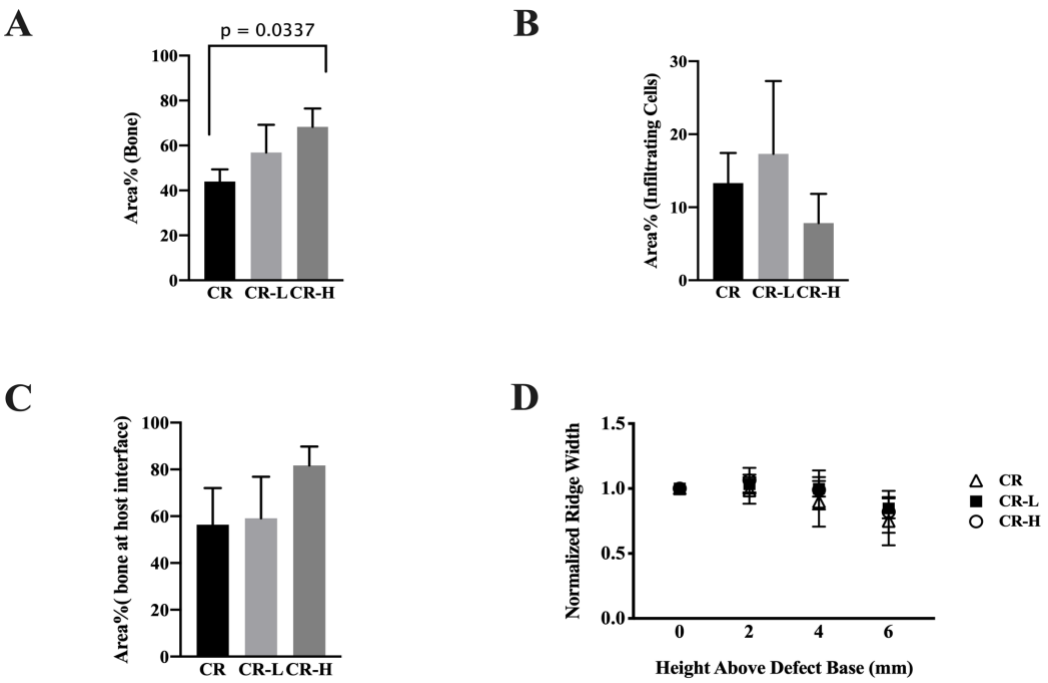


**Figure 3.4.** Histomorphometric analysis. (A) Normalized ridge width within the area of interest at 0, 2, 4, and 6 mm from the baseline of the defect. (B) Histomorphometric analysis of integration of host bone with the implants. The area% new bone near the periphery of the implant (1 mm distance from the sagittal wall of the defect) was measured. (C) Histomorphometric analysis of new bone (red) and (D) infiltrating cells (blue) within the area of interest.

**Table 3.3.** Ridge width measured at 16 weeks at 0, 2, 4, and 6, mm above the base of the defect. Ridge width was normalized to the baseline.

| | | 0 | 2 | 4 | 6 |
|---|---|---|---|---|---|
| CR | Mean ± SD<br>Median | 1.00 | 0.99 ± 0.10<br>1.00 | 0.90 ± 0.19<br>0.92 | 0.75 ± 0.19<br>0.74 |
| CR-L | Mean ± SD<br>Median | 1.00 | 1.03 ± 0.07<br>1.04 | 1.00 ± 0.06<br>0.99 | 0.85 ± 0.08<br>0.84 |
| CR-H | Mean ± SD<br>Median | 1.00 | 1.07 ± 0.09<br>1.09 | 0.99 ± 0.15<br>1.05 | 0.82 ± 0.16<br>0.89 |

## 3.5 Discussion

This study evaluated bone regeneration in CR scaffolds augmented with rhBMP-2 in a pre-clinical non-human primate lateral ridge augmentation model. Three concentrations of rhBMP-2 (0, 0.75, and 1.5 mg/ml) were used to assess ridge width and new bone formation in response to the rhBMP-2 dose.[27] We hypothesized that the CR-H (1.5 mg/ml) carrier would enhance ridge width, which was the primary outcome in the study, compared with the CR-L (0.75 mg/ml) or control (0 mg/ml) groups. Although there was not a significant increase in ridge width with the CR-H carrier augmented with the same concentration of rhBMP-2 as the FDA-approved INFUSE® bone graft, significantly higher BV/TV (**Figure 3.2**) and area% bone (**Figure 3.4)** in the lateral ridge defects were observed compared with CR samples. A post-hoc BV/TV effect size of 1.922 was calculated utilizing a Kruskal-Wallis H test based on the experimental data and actual number of replicates included in each group, which provided a power of >99%.

rhBMP-2 has previously been used to promote mandibular reconstruction in non-human primate preclinical models.[18,28,29] In this study, the non-human primate was chosen because of its anatomic and biological similarity to humans. Additionally, non-human primates experience the same dose-limiting toxicity of humans[30], and non-human primate studies are required by regulatory agencies to demonstrate the safety and efficacy of potential new therapies.[31] These

characteristics render the non-human primate lateral ridge augmentation model valuable for evaluation of potential new periodontal regenerative therapies.

Membranes are frequently used in ridge augmentation to provide a barrier that prevents soft tissue ingrowth while maintaining space within the defect to allow for new bone formation.[32] They must remain covered for the entirety of the healing period as early membrane exposure has been shown to lead to overall negative clinical outcomes.[33–35] Despite the frequent use of membranes, some studies have suggested no difference or increased new bone formation in grafts without membranes compared to those with membranes.[36,37] The ceramic granules impart compression-resistant mechanical properties to the PUR/ceramic scaffolds.[16,28] At the same dose of rhBMP-2 delivered to lateral ridge defects in hounds, ridge width and new bone formation at 16 weeks in CR carriers with no membrane was comparable to that in the collagen carrier with a membrane.[17] Consequently, in an effort to reduce the number of animals, we did not include a collagen with membrane group in the non-human primate study.

The carrier for rhBMP-2 is crucial in the induction of new bone. CR composites contained 45 wt% CM particles. The ceramic particles were added due to their osteoconductive and CR properties as reported previously in porcine [28], sheep[15], and canine[16,17] models. Residual CM particles were observed in some sections but could not be reliably quantified due to their low concentration. Resorption of CM particles was also observed in previous studies evaluating CR carriers for rhBMP-2 in canine ridge augmentation models.[16,17] These observations are consistent with a previous study reporting that CM granules implanted in extraction sockets in human patients were infiltrated and resorbed by osteoclasts.[38] Histomorphometric analysis showed preserved anatomic contour of the ridge in all groups, which contrasts with our previous study reporting that space maintenance in CR carriers increased with rhBMP-2 concentration in a canine-model of

ridge augmentation.[17] These findings suggest that CR carriers provide space maintenance and prevent tissue collapse into the defect site.

Considering that rhBMP-2 increases recruitment of osteoprogenitor cells[39], we assessed cellular infiltration into the implants by histomorphometry. The area% infiltrating cells and granulation tissue within the defect space at 16 weeks trended higher in the CR and CR-L groups compared with the CR-H group. However, differences in cellular infiltration between groups were not significant. This finding suggests that although overall cellular infiltration is comparable between groups, a larger percentage of cells in the CR-H group are osteoprogenitor cells that promote new bone formation.

This study evaluated clinically relevant doses of rhBMP-2 comparable to those used in human patients. While we cannot exclude the possibility that some of the implants were partially or completely removed at 9-14 days due to graft exposure, we have previously reported that the CR carriers deliver a 25% burst release of rhBMP-2 within the first 3 days and ~70% release after 14 days.[17] In contrast to the adsorption-controlled release reported for the collagen carrier[40], the release of rhBMP-2 from CR carriers is diffusion-controlled.[17] Thus, most of the rhBMP-2 was released from the CR grafts at the time of exposure. Consistent with a previous non-human primate study utilizing rhBMP-2 coated titanium implants[4], a dose-responsive increase in new bone formation was observed amongst groups. CR-H specimens demonstrated increased new bone formation compared with the CR group. Although ridge width was maintained in all groups, CR and CR-L showed less new bone formation near the periphery of the implant compared with the CR-H group. These observations suggest that CR carriers for rhBMP-2 promote new bone formation within the lateral ridge when administered at the same dose as the FDA-approved INFUSE® bone graft.

To minimize the number of animals needed to maintain statistical power, the study did not include multiple time points or an empty defect as a negative control, and thus the extent of self-healing of the defects could not be assessed. Despite the fact that the defect was critical-size[18,41,42], new bone formation in the control group without rhBMP-2 was observed. The observed new bone formation in the CR group is consistent with previous studies reporting modest new bone formation utilizing a compression-resistant carrier without rhBMP-2 in a non-human primate ridge models.[26,28] However, in both of these previous studies, the groups with rhBMP-2 showed increased new bone formation compared with CR carriers without rhBMP-2, suggesting that the addition of rhBMP-2 enhances the reproducibility of bone regeneration in non-human primate models. Another study utilizing a non-compression-resistant polylactic-*co*-glycolic acid foam carrier without rhBMP-2 in a non-human primate model showed negligible new bone formation in an empty defect.[18] While these findings suggest that space maintenance provided by compression-resistant scaffolds without rhBMP-2 may be sufficient to stimulate new bone formation, the addition of rhBMP-2 is anticipated to promote more predictable bone healing.

This study showed that local delivery of 1.5 mg/ml rhBMP-2, which is the concentration used clinically with a non-compression-resistant collagen carrier, increased new bone formation but not ridge width at 16 weeks. A limitation of the study is that rhBMP-2 may have accelerated ridge augmentation, which would require assessment of outcomes at earlier (e.g., 8 weeks) time points. Enhanced new bone formation at 16 weeks is not necessarily an indicator of the ability of the newly formed bone to support functional loading of dental implants, which is the primary clinical endpoint for lateral ridge augmentation procedures. Future studies will assess the ability of CR carriers to regenerate sufficient new bone to support restored dentition.

## 3.6 Conclusion

In a clinically relevant non-human primate model, we tested the hypothesis that CR PEUR/ceramic carriers for rhBMP-2 promote new bone formation in a dose-responsive manner. CR scaffolds maintained comparable ridge width in all groups and promoted new bone formation in the expected dose-responsive manner. Based on the results of this study, CR PEUR/ceramic bone grafts may be effective new carriers for rhBMP-2 for clinical use in lateral ridge augmentation procedures.

References


1. Chim, H. & Gosain, A. K. Biomaterials in craniofacial surgery: experimental studies and clinical application. *J. Craniofac. Surg.* **20**, 29–33 (2009).
2. Kalk, W. W. ., Raghoebar, G. M., Jansma, J. & Boering, G. Morbidity from iliac crest bone harvesting. *J. Oral Maxillofac. Surg.* **54**, 1424–1429 (1996).
3. Polimeni, G. *et al.* Alveolar ridge augmentation using implants coated with recombinant human growth/differentiation factor-5: Histologic observations. *J. Clin. Periodontol.* **37**, 759–768 (2010).
4. Wikesjö, U. M. E. *et al.* Bone formation at recombinant human bone morphogenetic protein-2-coated titanium implants in the posterior maxilla (Type IV bone) in non-human primates. *J. Clin. Periodontol.* **35**, 992–1000 (2008).
5. Urist, M. R. Bone: Formation by Autoinduction. *Science (80-. ).* **150**, 893–899 (1965).
6. Spector, J. A. *et al.* Expression of bone morphogenetic proteins during membranous bone healing. *Plast. Reconstr. Surg.* **107**, 124–34 (2001).
7. Wozney, J. M. *et al.* Novel regulators of bone formation: molecular clones and activities. *Science (80-. ).* **242**, 1528–34 (1988).
8. McKay, W. F., Peckham, S. M. & Badura, J. M. A comprehensive clinical review of recombinant human bone morphogenetic protein-2 (INFUSE® Bone Graft). *Int. Orthop.* **31**, 729–734 (2007).
9. Garcia, J. *et al.* Effect of membrane exposure on guided bone regeneration: A systematic review and meta-analysis. *Clin. Oral Implants Res.* **29**, 328–338 (2018).
10. Rakhmatia, Y. D., Ayukawa, Y., Furuhashi, A. & Koyano, K. Current barrier membranes: Titanium mesh and other membranes for guided bone regeneration in dental applications. *Journal of Prosthodontic Research* **57**, 3–14 (2013).
11. King, G. N. & Cochrant, D. L. Factors That Modulate the Effects of Bone Morphogenetic Protein-Induced Periodontal Regeneration: A Critical Review. *J. Periodontol.* **73**, 925–36 (2005).
12. Bonzani, I. C. *et al.* Synthesis of two-component injectable polyurethanes for bone tissue engineering. *Biomaterials* **28**, 423–433 (2007).
13. Dumas, J. E. *et al.* Synthesis and Characterization of an Injectable Allograft Bone/Polymer Composite Bone Void Filler with Tunable Mechanical Properties. *Tissue Eng. Part A* **16**, 2505–2518 (2010).
14. McEnery, M. A. P. *et al.* Oxidatively degradable poly(thioketal urethane)/ceramic composite bone cements with bone-like strength. *RSC Adv.* **6**, 109414–109424 (2016).
15. Talley, A. D. *et al.* Remodeling of injectable, low-viscosity polymer/ceramic bone grafts in a sheep femoral defect model. *J. Biomed. Mater. Res. - Part B Appl. Biomater.* **105**, 2333–2343 (2017).
16. Talley, A. D. *et al.* Effects of Recombinant Human Bone Morphogenetic Protein-2 Dose and Ceramic Composition on New Bone Formation and Space Maintenance in a Canine Mandibular Ridge Saddle Defect Model. *Tissue Eng. Part A* **22**, 469–479 (2016).
17. Talley, A. D., Boller, L. A., Kalpakci, K. N., Shimko, D. A. & Guelcher, C. S. A. Injectable , compression - resistant polymer / ceramic composite bone grafts promote lateral ridge augmentation without protective mesh in a canine model. *Clin. Oral Implants Res.* 592–602 (2018). doi:10.1111/clr.13257
18. Marukawa, E. *et al.* Bone regeneration using recombinant human bone morphogenetic

protein-2 (rhBMP) in alveolar defects of primate mandibles. *Br. J. Oral Maxillofac. Surg.* **39**, 452–9 (2001).
19. Guelcher, S. *et al.* Synthesis, in vitro degradation, and mechanical properties of two-component poly(ester urethane)urea scaffolds: effects of water and polyol composition. *Tissue Eng.* **13**, 2321–2333 (2007).
20. Guelcher, S. A. *et al.* Synthesis and in vitro biocompatibility of injectable polyurethane foam scaffolds. *Tissue Eng.* **12**, 1247–1259 (2006).
21. Prieto, E. M. & Guelcher, S. A. Tailoring properties of polymeric biomedical foams. in *Biomedical Foams for Tissue Engineering Applications* 129–162 (2014). doi:10.1533/9780857097033.1.129
22. Hanisch, O. *et al.* Bone formation and osseointegration stimulated by rhBMP-2 following subantral augmentation procedures in nonhuman primates. *Int. J. Oral Maxillofac. Implants* **12**, 785–92 (1997).
23. Boyne, P. J., Nakamura, A. & Shabahang, S. Evaluation of the long-term effect of function on rhBMP-2 regenerated hemimandibulectomy defects. *Br. J. Oral Maxillofac. Surg.* **37**, 344–352 (1999).
24. Medtronic. *PMA P050053: FDA Summary of Safety and Effectiveness Data*. (2007).
25. Lu, S. *et al.* Settable polymer/ceramic composite bone grafts stabilize weight-bearing tibial plateau slot defects and integrate with host bone in an ovine model. *Biomaterials* **179**, 29–45 (2018).
26. Miranda, D. A. O., Blumenthal, N. M., Sorensen, R. G., Wozney, J. M. & Wikesjö, U. M. E. Evaluation of Recombinant Human Bone Morphogenetic Protein-2 on the Repair of Alveolar Ridge Defects in Baboons. *J. Periodontol.* **76**, 210–20 (2005).
27. Govender, S. *et al.* Recombinant human bone morphogenetic protein-2 for treatment of open tibial fractures: a prospective, controlled, randomized study of four hundred and fifty patients. *J. Bone Joint Surg. Am.* **84-A**, 2123–34 (2002).
28. Herford, A. S. *et al.* Recombinant human bone morphogenetic protein 2 combined with an osteoconductive bulking agent for mandibular continuity defects in nonhuman primates. *J. Oral Maxillofac. Surg.* **70**, 703–716 (2012).
29. Marukawa, E. *et al.* Functional reconstruction of the non-human primate mandible using recombinant human bone morphogenetic protein-2. *Int. J. Oral Maxillofac. Surg.* **31**, 287–95 (2002).
30. FDA. Guidance for industry: Estimating the maximum safe starting dose in initial clinical trials for therapeutics in adult healthy volunteers. *FDA Guid.* (2005). doi:10.1089/blr.2006.25.697
31. Kaigler, D., K, F. & WV, G. Regulatory agencies for the evaluatioin of dental drugs, devices and biologics. in *Clinical research in oral health* (eds. Giannobile, W., Burt, B. & Genco, R.) (Wiley-Blackwell, 2010).
32. Blumenthal, N. M. A Clinical Comparison of Collagen Membranes With e-PTFE Membranes in the Treatment of Human Mandibular Buccal Class II Furcation Defects. *J. Periodontol.* **64**, 925–33 (2012).
33. Ruskin, J. D., Hardwick, R., Buser, D., Dahlin, C. & Schenk, R. K. Alveolar ridge repair in a canine model using rhTGF-beta 1 with barrier membranes. *Clin. Oral Implants Res.* **11**, 107–115 (2000).
34. Souza, S. L. S. *et al.* Guided bone regeneration with intentionally exposed membranes and its implications for implant dentistry. A 6 months re-entry randomized clinical trial. *J.*

*Osseointegration* **2**, 45–51 (2010).
35. Yoshinari, N. *et al.* Inflammatory cell population and bacterial contamination of membranes used for guided tissue regenerative procedures. *J. Periodontol.* **69**, 460–9 (1998).
36. Jovanovic, S. A., Shcenk, R., Orsini, M. & Kenney, E. Supracrestal bone formation around dental implants: an experimental dog study. *Int J Oral Maxillofac Implant.* **10**, 23–31 (1995).
37. Lee, J. Y., Lee, J. & Kim, Y. K. Comparative analysis of guided bone regeneration using autogenous tooth bone graft material with and without resorbable membrane. *J. Dent. Sci.* **8**, 281–286 (2013).
38. Wakimoto, M. *et al.* Histologic evaluation of human alveolar sockets treated with an artificial bone substitute material. *J. Craniofac. Surg.* **22**, 490–3 (2011).
39. Kimura, Y. *et al.* Controlled release of bone morphogenetic protein-2 enhances recruitment of osteogenic progenitor cells for de novo generation of bone tissue. *Tissue Eng. - Part A* **16**, 1263–70 (2010).
40. Seeherman, H. & Wozney, J. M. Delivery of bone morphogenetic proteins for orthopedic tissue regeneration. *Cytokine and Growth Factor Reviews* **16**, 329–345 (2005).
41. Asahina, I., Watanabe, M., Sakurai, N., Mori, M. & Enomoto, S. Repair of bone defect in primate mandible using a bone morphogenetic protein (BMP)- hydroxyapatite-collagen composite. *J Med Dent Sci* **44**, 63–70 (1997).
42. Fritz, M. E. *et al.* Guided bone regeneration of large mandibular defects in a primate model. *J. Periodontol.* **71**, 1484–91 (2000).

CHAPTER IV

# CHAPTER 4: POLY (ESTER URETHANE) AND POLY (THIOKETAL URETHANE) AUTOGRAFT EXTENDERS PROMOTE NEW BONE FORMATION AND REMODEL IN A RABBIT RADIUS MODEL

**Adapted from:**

**Boller LA**, McGough MAP, Shiels SM, Wenke JC, Guelcher SA. Poly (ester urethane) and Poly (thioketal urethane) Autograft Extenders Promote New Bone Formation and Remodel in a Rabbit Radius Model.

## 4.1 Abstract

Autograft (AG) is the gold standard for bone grafts, but limited quantities and patient morbidity are associated with its use. Alternatives to AG such as allograft and calcium phosphate-based materials have been studied extensively, but no current materials possess the osteoinductive, osteoconductive, and osteogenic properties of AG. AG extenders have been proposed to minimize the volume of AG while maintaining the osteoinductive properties of AG. In this study, poly (ester urethane) and poly (thioketal urethane) AG extenders were implanted in a 20-mm rabbit radius model to evaluate bone and graft remodeling. Outcomes were measured at 12 weeks and compared to an AG (no polymer) control. AG control examples exhibited some extent of bridging along the lateral side of the defect, but inconsistent healing was observed. Implanted AG extenders maintained implanted AG throughout the study. Bone growth from the defect interfaces was observed in both AG extenders, but residual polymer inhibited early cellular infiltration and subsequent bone formation within the center of the defect. PEUR-AG extenders degraded more rapidly than PTKUR-AG extenders, but no difference in bone formation was observed between the groups. These observations demonstrated that polymer composition does not affect overall bone formation and that early cellular infiltration is necessary for harnessing the osteoinductive capabilities of AG.

# CHAPTER IV

## 4.2 Introduction

Autograft (AG) bone is considered the gold standard in bone grafting. It is osteoinductive, osteoconductive, and osteogenic and does not pose a risk for disease transmission. [1–3] AG comes in various forms including both cancellous and cortical. [3] Cancellous AG is most often harvested from the iliac crest (IC); however, other donor sites such as the posterior superior iliac spine, femur, proximal tibia, and distal radius are utilized. [4–7] Cancellous AG contains mesenchymal stem cells (MSCs), osteoblasts, and growth factors including bone morphogenetic proteins (BMPs) which contribute to its osteoinductivity. [3,8] The trabeculae present within cancellous AG allow for enhanced cellular infiltration and vascularization in comparison to cortical AG. [8] Cortical AG is ideal for defects that require structural support as it offers superior mechanical properties in comparison with cancellous AG. However, cortical AG is less osteoinductive than cancellous AG and its density results in slower revascularization and inhibits cellular infiltration. [8,9]. Despite its osteogenic properties, AG has multiple drawbacks including high donor site morbidity which occurs in 10 – 39 % of patients and limited availability. [6]

The use of allograft from donors is an alternative to AG. Allograft is more readily available than AG and provides structural support, but it does not possess the same osteoinductive capacity as AG due to its processing. [2] Furthermore, allograft faces potential immune rejection and slow osseointegration with host bone. [10] Synthetic materials such as calcium phosphate (CaP) based composites and the use of growth factors such as BMPs have evolved as substitutes for AG, [11–13] but none of the options have been shown to match all of the benefits provided by AG. Residual ceramics in CaP composites can take months or years to completely resorb, [14,15] and the use of the FDA-approved rhBMP-2 treatment (INFUSE® bone graft, Medtronic) is limited to a few clinical indications. [16–18]

To overcome the limitations in AG availability, various approaches to increase the overall volume of AG while maintaining its osteogenic and osteoinductive properties have been employed. Additional material blended with AG is known as an 'extender'. An early study demonstrated the utility of demineralized bone matrix as an AG extender. [19] More recently, tissue engineered approaches to incorporate synthetic bone substitutes with AG have been investigated. CaPs such as β-tricalcium phosphate (β-TCP) and hydroxyapatite were evaluated as AG extenders for spinal applications. [20–23] Similarly, poly (propylene fumarate)- and poly(lactide-co-glycolide) (PLGA)-based polymer AG extenders have also been evaluated for spinal applications [24–27], while AG extenders utilizing bioactive glass particles have been investigated in the femur. [28]

Lysine-based poly (ester urethanes) (PEURs) and poly (thioketal urethanes) (PTKURs) have been previously investigated in bone regeneration applications. [29–32] The mechanical properties of these materials can be easily altered, and the addition of ceramic particles, AG, and allograft supports new bone formation at various anatomic sites. [33–36] Previous work has demonstrated selective, cell-mediated, first-order degradation of PTKUR *in vivo*. [37] Furthermore, low-porosity PTKURs utilized in rabbit intertransverse processes [38] and femoral plugs [32] exhibited new bone formation, but minimal PTKUR degradation was observed. Slow degradation is advantageous in applications in which mechanical stability is required, however, in applications utilizing biologics, quicker graft resorption is necessary to harness the osteoinductivity. In a previous study, PEUR has been used to deliver rhBMP-2 and has demonstrated balanced polymer resorption and new bone formation [36,39]. Therefore, we utilized faster resorbing PEUR [40,41] and compared with PTKUR [37] in an autograft extender to test the hypothesis that PEUR would degrade faster and allowing for increased cellular infiltration and bone formation in a rabbit radius model.

# CHAPTER IV

Herein, settable and resorbable PTKUR-AG and PEUR-AG extenders were implanted in 20-mm segmental defects in the rabbit radius to investigate new bone and graft remodeling capabilities. In this study, PTKUR or PEUR was blended with fresh IC AG. The resulting material was subsequently molded to size and implanted into the defect. *In vivo* outcomes assessed post-operatively with x-ray, μCT, histology, and histomorphometry were compared to an AG control.

## 4.3 Materials and Methods

*Materials*. All chemicals were purchased from Sigma-Aldrich with the exception of anhydrous diethyl ether purchased from Fisher Scientific. Lysine triisocyanate-polyethylene glycol (LTI-PEG) prepolymer (NCO=21.7%) was obtained from Ricerca Biosciences LLC.

*Polyester triol and thioketal diol synthesis.* The polyester triol (molecular weight 450 g $mol^{-1}$) was synthesized utilizing a previously published method. [42] Briefly, glycerol, 70% ε-caprolactone, 20% glycolide, and 10% DL-lactide monomers were mixed for 40 hours under argon at 140°C. The resulting fluid was vacuum dried at 80°C for 48 hours.

Thioketal (TK) diol was synthesized utilizing a previously published method. [31] Briefly, 2,2-dimethoxypropane and thioglycolic acid were reacted in the presence of bismuth (III) chloride at room temperature for 24 hours. The resulting solution was filtered, dissolved in tetrahydrofuran, and added dropwise to $LiAlH_4$ under anhydrous conditions. The reaction was refluxed at 52°C for 18 hours, and the product was filtered and vacuum dried for 48 hours.

*AG extender fabrication.* PTKUR- and PEUR-AG extenders were fabricated by adapted two-component reactive-liquid molding methods as previously described. [38] Briefly, polyisocyanate comprised of either TK diol or polyester triol, 10 pphp FeAA catalyst in ϵ-caprolactone 0.5% (w/w), and LTI-PEG prepolymer were mixed together. Morselized AG (70

wt%) was added to the mixture and stirred by hand until homogeneous. The targeted index (NCO:OH) was 200.

*AG extenders in rabbit radius defect.* All surgical and care procedures were approved by the Institutional Animal Care and Use Committee of the US Army Institute of Surgical Research, Fort Sam Houston, TX. Procedures were performed in compliance with the Animal Welfare Act, Animal Welfare Regulations, and the Guide for the Care and Use of Laboratory Animals.

Adult New Zealand White rabbits were used in this study (n =12). Animals were randomly assigned to PEUR-AG, PTKUR-AG, or AG control treatment groups (n=4 per group). Animals were premedicated with slow-release Buprenorphine (0.1 mg $kg^{-1}$) an anesthetized with isoflurane (1-3%). For all groups, the animal's left hindlimb and right forelimb were shaved and prepared for sterile surgery using alternating washes of alcohol and povidone-iodine. The left IC was exposed, and AG (0.6-0.7 g) was obtained using an oscillating saw. Excess soft tissue was removed, and a bone mill (R. Quétin) was used to morselize the harvested bone. The IC harvest site was closed, and the right radius was exposed. An oscillating saw was used to create a 20 mm segmental defect in the radius. AG extenders were prepared as explained in section 2.3 and were shaped to size (5 mm x 20 mm). AG control (morselized AG without PTKUR or PEUR) was molded to shape and carefully placed within the defect. A surgical elevator was used to place the AG extenders inn the defects to ensure correct placement. AG extenders were allowed to cure *in situ* (**Figure 4.1**) after which the radial site was closed. Post-operative x-ray images (Faxitron X20) were taken throughout recovery and Calcein green and Xylenol orange fluorochromes were injected at 4 and 8 weeks post-operatively, respectively, to evaluate bone remodeling temporally. Animals were anesthetized and euthanized at 12 weeks. The radii were harvested and placed into formalin for further analysis.

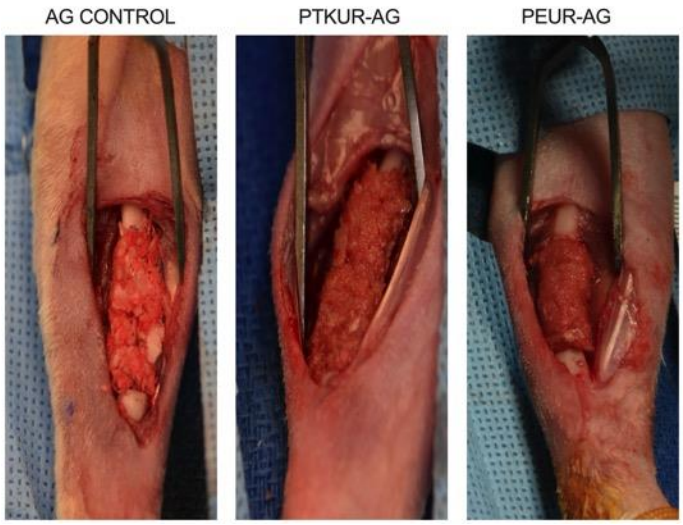


**Figure 0.1.** Surgical images. AG control, PTKUR-AG extender, and PEUR-AG extender in the 20 mm defect prior to closure.

*µCT Analysis*. µCT analysis was performed using a µCT50 (SCANCO). Radii were scanned at 70 kVp energy, 200 µA source current, 1000 projections per rotation, 800 ms integration time, and 17.2 µm voxel size. In order to spatially evaluate bone growth throughout the defect, bone area was calculated for each axial section (17.2 µm) totaling 20 mm. The area of interest (AOI) included the proximal onset of the defect and extended the length of the defect. It is not possible to distinguish AG from old or new bone utilizing µCT, thus the ulna was included in analysis due to bone formation observed within the interosseous syndesmosis interfacing the ulna in some of the samples. Bone area was plotted as a function of defect length where 0 mm and 20 mm represented the proximal and distal ends of the defect, respectively. Additionally, the total volume of new bone within the AOI was measured to calculate bone volume fraction (BV/TV).

*In vivo histological evaluation***.** Non-decalcified histology was utilized to evaluate bone formation and remodeling. [35,39] After formalin fixation, radii were dehydrated and embedded in poly (methyl methacrylate). Serial coronal sections were cut from the center of each defect with an Exakt band saw. Sections were polished and stained with Sanderson's Rapid Bone Stain to

assess osteogenesis and remodeling. An unstained section was utilized to analyze fluorochrome binding. High magnification histological images were obtained via bright-field microscopy (Olympus BX41).

For quantitative histomorphometry, images were taken at 4X via-bright field and fluorescent microscopy (Biotek Cytation). The AOI was defined as a 20 x 5 mm rectangular region that encompassed the entirety of the graft and defect. The ulna was excluded from the AOI. The same AOI was used for both Sanderson's Rapid stained and fluorescent sections. Quantification of new bone, infiltrating cells and tissue, and residual polymer was performed using Metamorph (Version 7.0.1). Bone was thresholded either as red (Sanderson's rapid) or green/orange (fluorochromes). Residual material was thresholded as black stain and infiltrating cells were thresholded as blue/teal. Thresholded area was reported as an area percentage of the total AOI.

*Statistical Analysis.* Data were analyzed utilizing GraphPad Prism (Version 8.4.1) and reported as mean ± standard deviation. Treatment group outcomes at 12 weeks were evaluated using an ANOVA with a Tukey's multiple comparison test. Treatment group outcomes compared at 4 and 8 weeks were evaluated using a two-way ANOVA with Tukey's multiple comparison test. Statistical significance was set at $p<0.05$.

## 4.4 Results

*Surgical outcomes.* The surgical procedures and subsequent healing were uneventful. No fractures of the radii occurred. X-rays displayed healing progression from 0 to 12 weeks in all of the groups (**Figure 4.2**). AG control presented challenges in implantation and shape maintenance during the surgical procedures due to the lack of a binding agent. However, AG control remained in place throughout the study and displayed complete bridging of the defect along the lateral side of the defect (**Figure 4.2A**). Bridging along the lateral side of the defect was observed within 3 of

the AG samples. Both AG extenders were coherent throughout surgical placement and remained stable throughout the entirety of the study (**Figure 4.2B-C**). The AG extenders displayed new bone growth at the host bone/graft interfaces and graft remodeling was observed in both AG extenders, specifically at the proximal and distal ends of the defect where new bone and decreasing residual graft was observed. Both AG extenders exhibited increasing opacity within the grafts over the 12-week time course, and no differences in new bone formation within the graft were qualitatively observed between PTKUR- and PEUR- AG groups.

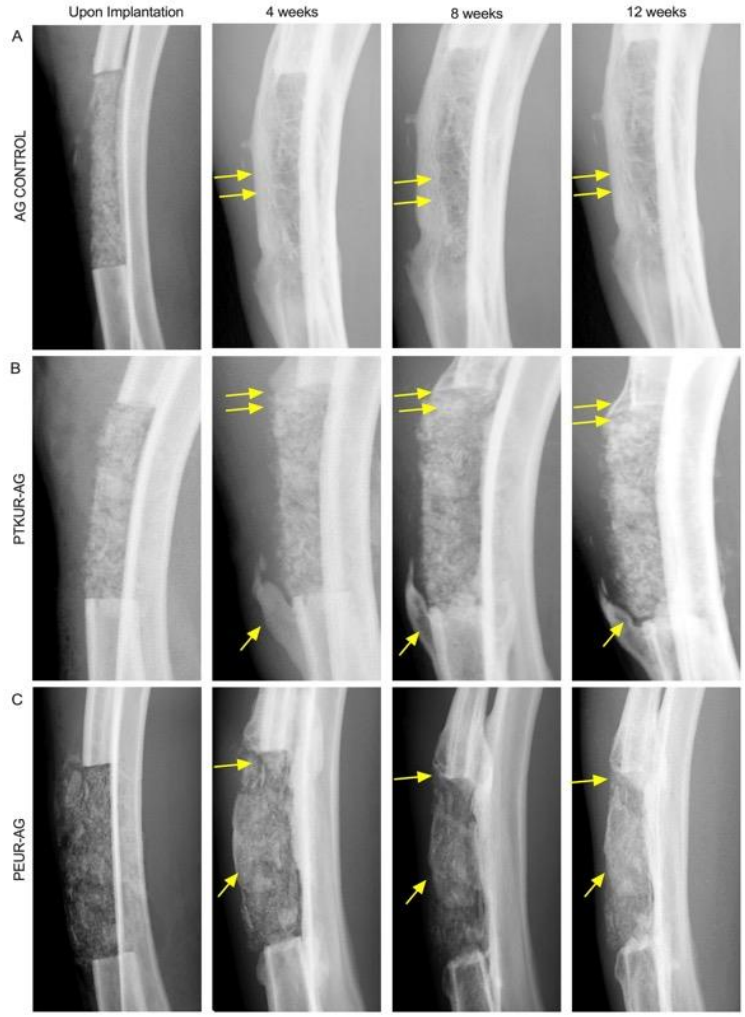


**Figure 0.2.** Representative X-ray images of (A) AG control, (B) PTKUR-AG, and (C) PEUR-AG acquired after the surgical procedures and after 4, 8, and 12 weeks of healing. Areas of bone remodeling and formation are noted by yellow arrows.

*In vivo bone formation with PTKUR- and PEUR-AG extenders.* Representative µCT images revealed no significant difference in bone formation between groups at 12 weeks (**Figure 4.3A**). These observations were confirmed with quantitative µCT analysis (**Figure 4.3B-C**). All groups displayed similar trends of increased bone area at the proximal and distal ends of the defect with a gradual decrease in bone area as the center of the defect was approached (**Figure 4.3B**). PEUR-AG extenders showed slightly increased BV/TV compared with PTKUR-AG and AG control, but the differences were not significant (**Figure 4.3C**).

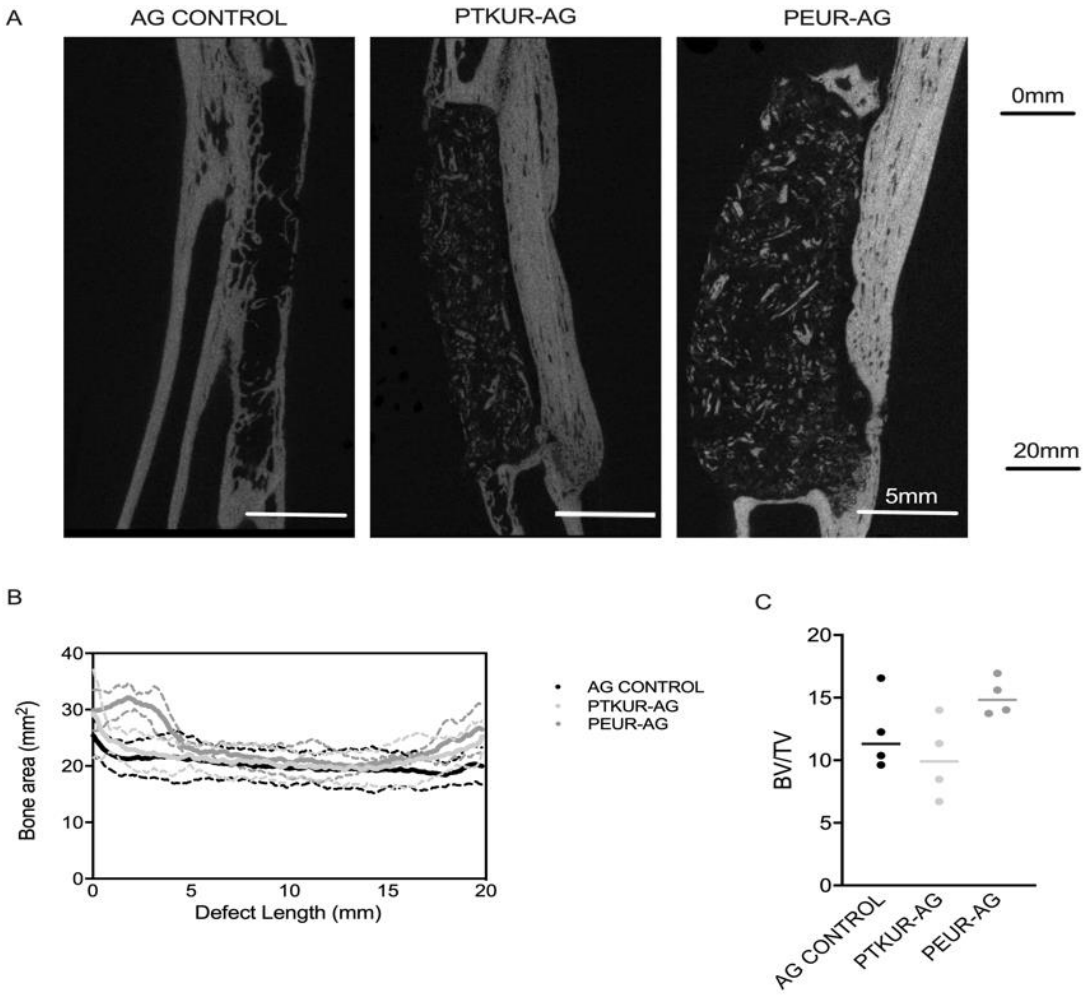


**Figure 0.3.** µCT analysis of bone remodeling. Representative images of (A) AG control, PTKUR-AG, and PEUR-AG 12 weeks post-operatively. (B) Bone area at 12 weeks measured as a function of defect length by µCT from the proximal to distal interfaces of the defect. Corresponding dotted lines representative standard deviation. (C) Bone volume/ total volume (BV/TV) at 12 weeks for each treatment group

Similarly, bone formation via histological analysis was observed within all groups (**Figure 4.4A, Figure 4.5**). Quantitative histomorphometric analysis at 12 weeks showed no significant difference in new bone formation between PTKUR- and PEUR-AG extenders (**Figure 4.4B**). AG control, however, exhibited significantly increased new bone formation when compared to both AG extenders (**Figure 4.4B**). Although the AG control displayed greater new bone formation, healing within the samples appeared to be inconsistent (**Figure 4.4C**). Though, AG extenders displayed less overall new bone formation, bone appeared to form evenly throughout the defect (**Figure 4.4C**).

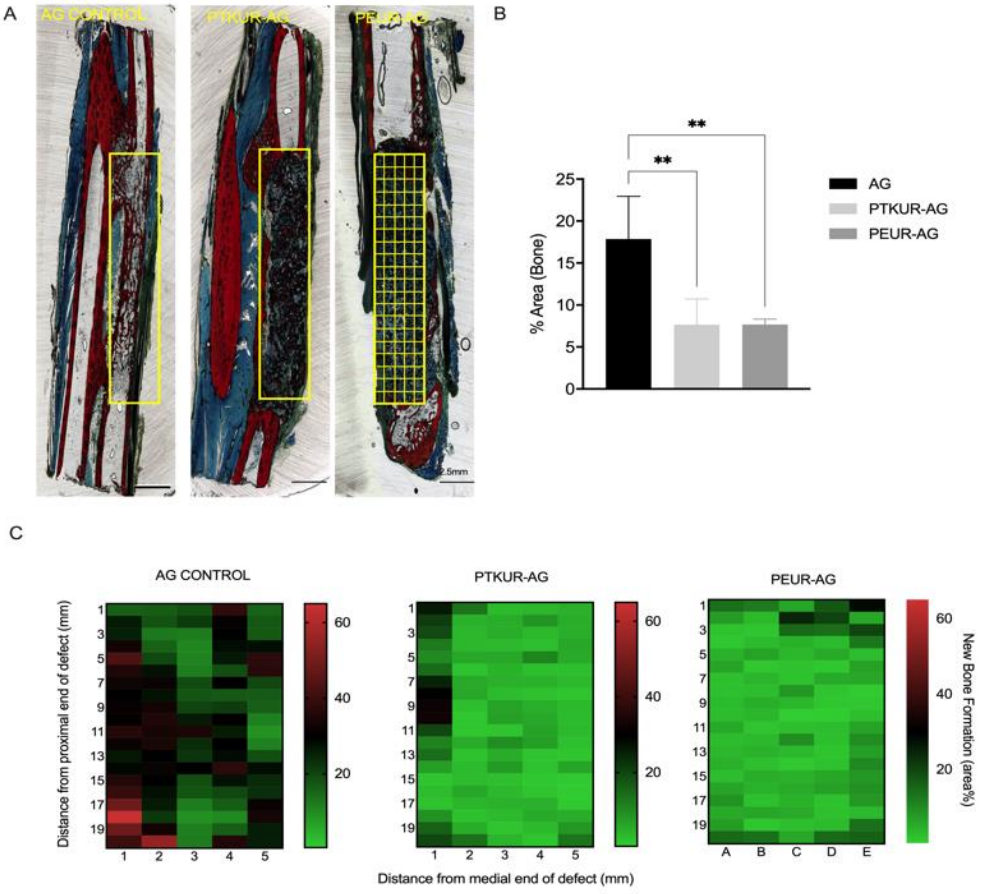


**Figure 0.4.** New bone formation in AG extenders. (A) Representative images of Sanderson's Rapid stained AG, PTKUR-AG, and PEUR-AG histological sections. The AOI (20 mm x 5 mm) used for analysis is indicated by the yellow box. (B) Histomorphometric analysis of area % new bone (red) at 12 weeks within the defect. (C) Heatmaps demonstrate new bone formation as a function of location. The AOI used for analysis is indicated by the yellow grid (each square = 1 mm2). Plotted data are average values within each group. Statistical significance determined using One-way ANOVA, **p<0.01.

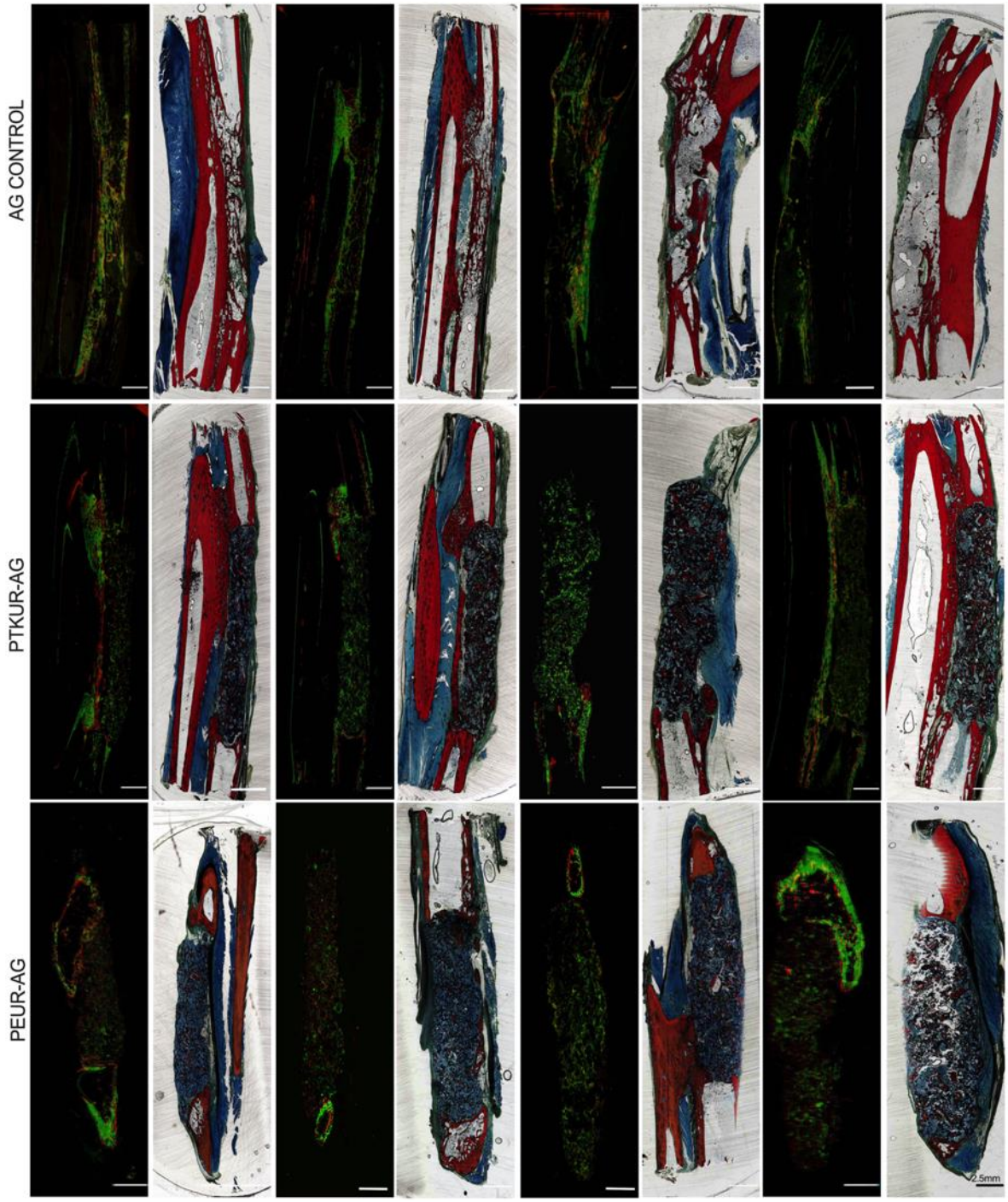


**Figure 0.5.** Fluorescent and Sanderson's Rapid stained histological sections of AG control, PTKUR-AG, and PEUR-AG extenders.

Representative histological sections show the ingrowth of new bone at the graft interface indicating osseointegration in all groups. (**Figure 4.6A)** Furthermore, osteoblasts were observed around the perimeter of bone ingrowth, suggesting active ongoing remodeling (**Figure 4.6B**).

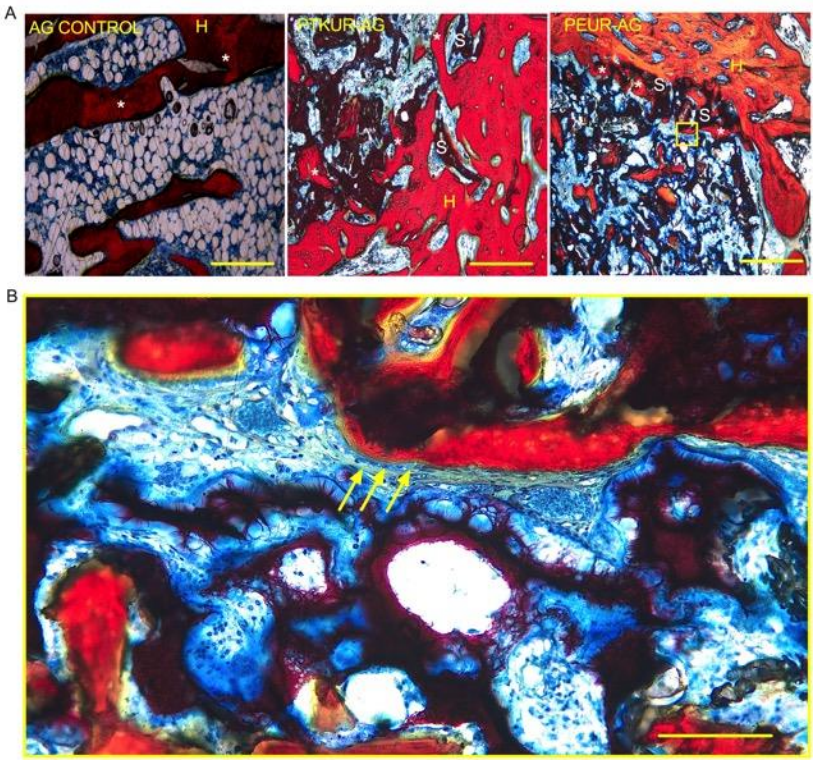


**Figure 0.6.** Osseointegration of AG extenders. (A) Histological images demonstrate osseointegration of the AG extenders at the host bone/material interface. H represents new bone, S represents scaffold, and * represents new bone growth. (Scale bar, 1 mm) (B) New bone growth occurring within the graft. Yellow arrows point to osteoblasts. (Scale bar, 100µm).

*PTKUR and PEUR graft remodeling*. Histological analysis revealed residual polymer (black) in AG extenders (**Figure 4.4A, Figure 4.5**). These findings were confirmed via histomorphometric analysis (AOI represented in **Figure 4.4A**) in which PTKUR-AG exhibited significantly more residual polymer compared with the PEUR-AG group (**Figure 4.7A**). High-magnification images further showed that PTKUR-AG underwent slower resorption as evidenced by the higher amount of dense residual polymer (black) in the PTKUR-AG sections compared with the extensive resorption gaps evident in the PEUR-AG sections (**Figure 4.7B-C**). All groups supported cellular and tissue infiltration (teal/blue), but significantly greater cellular and tissue

infiltration was observed in the PEUR-AG group compared with PTKUR-AG and AG control (**Figure 4.7A-C**). Osteoclast degradation was observed near bone and residual graft within the AG extender (**Figure 4.7D**).

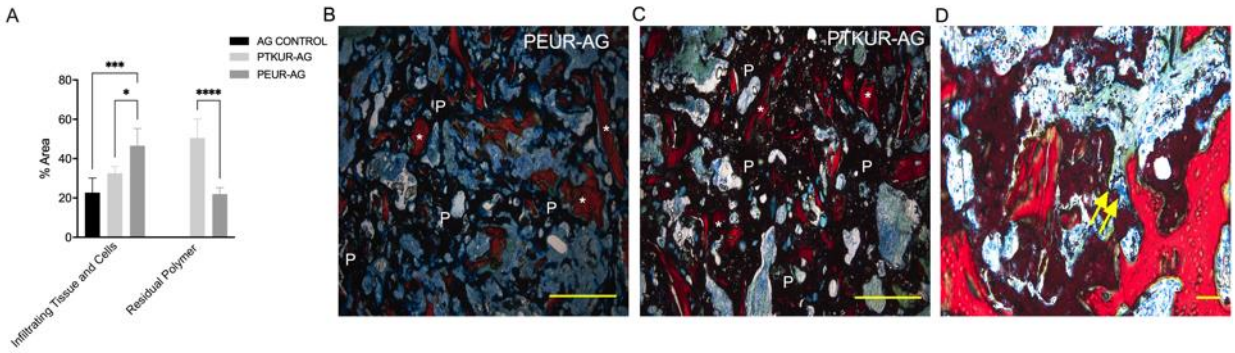


**Figure 0.7.** AG extender graft remodeling. (A) Histomorphometric analysis of area % infiltrating cells and tissue and residual polymer within the defect after 12 weeks post implantation. Representative images of residual polymer in (B) PEUR-AG extenders and (C) PTKUR-AG extenders. P denotes residual polymer and * denotes implanted AG. (Scale bar, 1mm) (D) Osteoclast degradation of AG extender. Yellow arrows indicate multi-nucleated osteoclast. (Scale bar, 100μm). Statistical significance determined using Two-way ANOVA, *p<0.05, ***p<0.001, ****p<0.0001.

Bone remodeling throughout the healing process was observed in all groups, especially at the proximal and distal host bone/graft interfaces (**Figure 4.5**). Remodeling was observed within the PTKUR- and PEUR-AG grafts around the periphery of implanted AG at 4 and 8 weeks, indicating mineralization nucleating from implanted AG particles within the extenders (**Figure 4.8A**). PTKUR- and PEUR- AG extenders exhibited increased bone remodeling at 4 weeks (green) when compared with 8 weeks (orange), however, these differences were not significant (**Figure 4.8B**). Additionally, increased bone remodeling was observed at the graft/host bone interface indicating osseointegration of both AG extenders (**Figure 4.8C-D**). The AG control demonstrated significantly greater bone remodeling compared to the AG extenders at both 4 and 8 weeks (**Figure 4.8B**). Inconsistent healing was observed as only two of the four control exhibited complete bridging along the lateral edge of the defect (**Figure 4.5**).

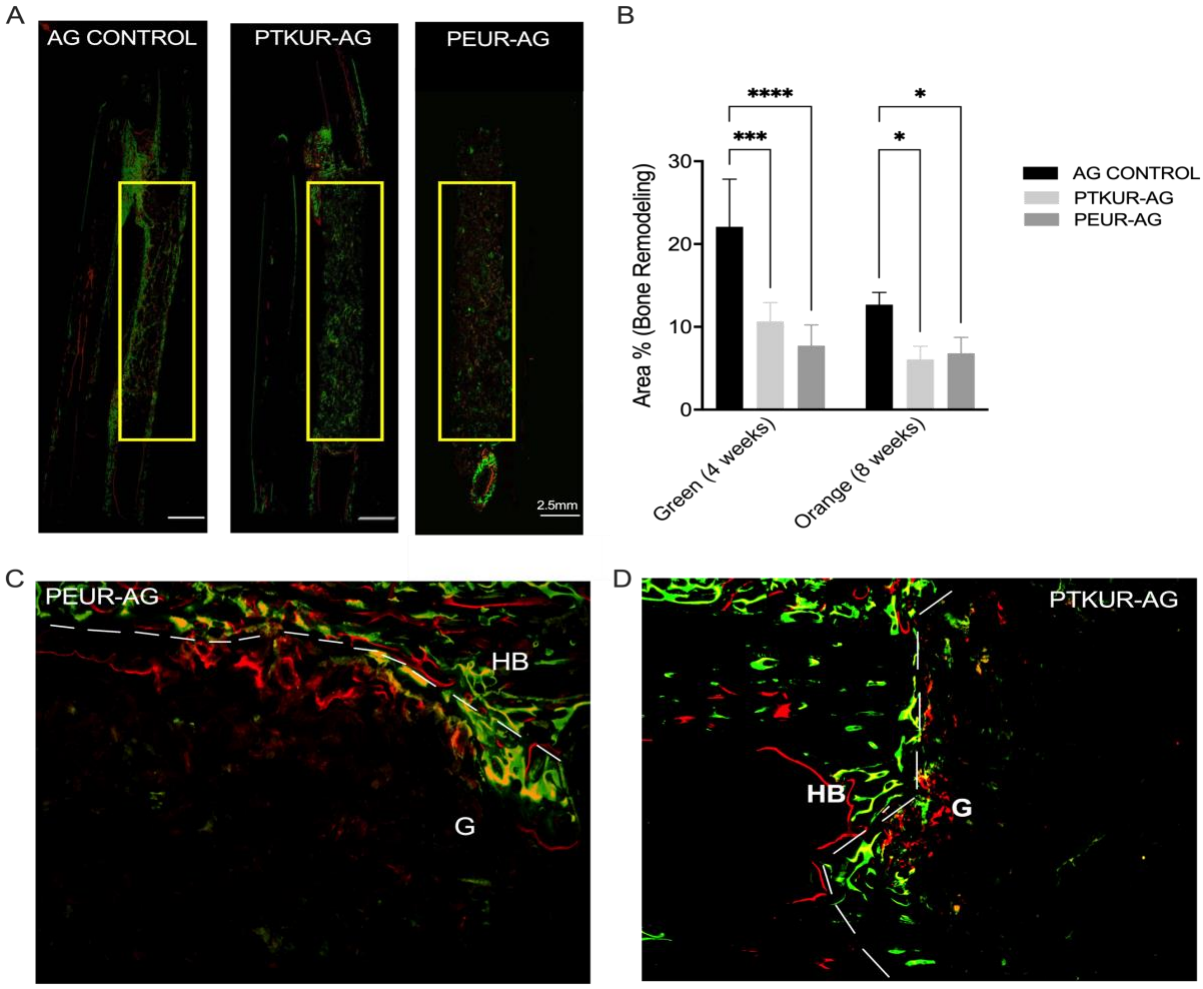


**Figure 0.8.** Dynamic histomorphometric analysis at 4- and 8-weeks. (A) Representative fluorescent images of AG, PTKUR-AG, and PEUR-AG groups. The AOI is indicated by the yellow box. (B) Histomorphometric analysis of area % active bone remodeling at 4 (green) and 8 8 (orange) weeks within the defect. Representative images of bone remodeling at the host bone graft interface demonstrating osseointegration in (C) PEUR-AG extenders and (D) PTKUR-AG extenders. Statistical significance determined using Two-way ANOVA, *p<0.05, ****p<0.0001.

## 4.5 Discussion

In this work, we implanted PTKUR-AG and PEUR-AG extenders in a 20-mm rabbit radial defect to evaluate the effects of polymer composition on both bone formation and graft remodeling *in vivo*. Both PTKUR- and PEUR-AG extenders supported bone formation and comparable to that of AG control. Furthermore, AG extenders degraded and simultaneously maintained AG within the defect for 12 weeks. PEUR-AG extenders degraded more rapidly compared with PTKUR-AG

extenders. However, new bone formation in both AG extenders was delayed compared with the AG control.

To understand the effect of polymer composition on bone formation and graft remodeling, AG extenders were implanted in a 20-mm rabbit radial defect. This model was selected as no external fixation was required [2] and a non-critical sized defect was chosen to maintain the capacity to heal. [43,44] No graft failure was observed within any of the groups throughout the 12 weeks, suggesting that AG extenders exhibited sufficient compression resistant properties. Previous studies in the spine and mandible demonstrated that an elastic modulus >1 MPa provided compression resistant properties. [45,46] We previously reported PTKUR-AG and PEUR-allograft moduli of 6.08 MPa and 4.38 - 9.47 MPa, respectively. [38,47]

Previous studies performed in the rabbit radius have reported bone growth from the proximal end of the defect, distal end of the defect, and the interosseus membrane. [43,48–50] Similarly, we observed bone formation in these directions. Due to observed ossification within the interosseous membrane and the inability for µCT to distinguish between new and old bone, the ulna was included in µCT analysis. Despite inclusion of the ulna, no significant differences in BV/TV were observed between groups. Furthermore, µCT bone area quantification indicated increased bone at the proximal and distal end of the defect, indicating bone growth from the interfaces. Consistent with previous studies utilizing AG [51–53], new bone via creeping substitution at the host bone/graft interface was observed (**Figure 4.6C**).

Histomorphometric analysis was performed to evaluate remodeling specifically in the 5 mm x 20 mm defect space, thus bone present in the interosseus membrane was excluded from analysis. Transverse sections were obtained from the center of the defect to evaluate bone formation at its most stringent point. Ultimately, no significant difference in bone between

PTKUR- and PEUR-AG extender was observed via histomorphometric analysis. The AG control demonstrated significantly increased new bone within the defect compared with AG extenders at 12 weeks via histomorphometric analysis, but new bone formation appeared to be variable throughout the defect. These differences were not observed in overall BV/TV between groups, suggesting that PTKUR- and PEUR-AG promoted bone formation, particularly in the interosseus membrane surrounding the defect while AG control promoted significantly greater bone formation within the defect site itself.

In agreement with an earlier PTKUR-AG study in a biologically stringent intertransverse process defect [38], residual polymer was observed in PTKUR-AG extenders at 12 weeks. PEUR degradation occurred more rapidly than PTKUR degradation as evidenced by significantly less residual polymer within the defect at 12 weeks. PTKUR degrades in response to specific cell types including osteoclasts, macrophages, and other ROS secreting cells [37] while PEUR degrades via hydrolytic and autocatalytic degradation. [54] Furthermore, AG control exhibited the least amount of cellular infiltration at 12 weeks demonstrating that cells recruited to the AG were osteoprogenitor cells that underwent direct differentiation. PTKUR-AG extenders exhibited less cellular infiltration than PEUR-AG extenders demonstrating that cells were able to more readily infiltrate into the graft as the polymer degraded. Upon cancellous AG implantation, early vascularization begins at 2 days and is quickly followed by the influx of MSCs from the osteoinductive signals of AG. Since the osteoinductive signals from AG occur in the first weeks after implementation [55], these findings suggest that residual polymer inhibited the osteoinductive effects of AG.

Dynamic bone histomorphometry is a widely utilized method for evaluating bone remodeling. [56,57] As mentioned above, ossification within the interosseus membrane was excluded

from dynamic histomorphometric analysis. In agreement with our static histomorphometric findings, bone remodeling at 4 and 8 weeks was greater in AG control compared with PTKUR- and PEUR-AG extenders within the defect. It is likely that the lack of polymer in AG control allowed for more extensive cellular infiltration and new bone formation. Despite a smaller 10 mm defect size, a previous study utilizing highly porous cell-seeded hydroxyapatite scaffolds did not observe fluorochrome binding within the scaffold until six weeks post-implantation [49]. Herein, fluorescent staining beginning at 4 weeks was apparent within the grafts in the AG extender groups suggesting that embedded AG maintained bioactivity. Additionally, abundant osseointegration at the host bone/graft interface in both AG extenders was observed further confirming bioactivity. AG is replaced by the formation of new bone on old bone [55]. Full degradation of synthetic polymers can take anywhere from 4 to 24 months *in vivo* [58], thus residual polymer likely inhibited bone remodeling within the center of the AG grafts. Future work should focus on optimizing a fast-degrading polymer.

## 4.6 Conclusion

In this work, PTKUR- and PEUR-AG extenders were evaluated against AG control in a rabbit radius model. PTKUR- and PEUR-AG extenders both maintained AG in the defect throughout the study and demonstrated bone formation along the host bone/graft interface comparable to AG control. Polymer resorption and subsequent cellular infiltration was observed within the defect space in both AG extenders but did not have an effect on overall bone formation. These results suggest that early cellular infiltration is necessary for harnessing and maximizing the osteoinductive capabilities of AG.

References


1. Albrektsson, T. & Johansson, C. Osteoinduction, osteoconduction and osseointegration. *Eur. Spine J.* **10**, S96–S101 (2001).
2. Shafiei, Z., Bigham, A. S., Dehghani, S. N. & Torabi Nezhad, S. Fresh cortical autograft versus fresh cortical allograft effects on experimental bone healing in rabbits: Radiological, Histopathological and Biomechanical evaluation. *Cell Tissue Bank.* **10**, 19–26 (2009).
3. Baldwin, P. *et al.* Autograft, Allograft, and Bone Graft Substitutes: Clinical Evidence and Indications for Use in the Setting of Orthopaedic Trauma Surgery. *Journal of orthopaedic trauma* (2019). doi:10.1097/BOT.0000000000001420
4. Myeroff, C. & Archdeacon, M. Autogenous bone graft: Donor sites and techniques. *Journal of Bone and Joint Surgery - Series A* (2011). doi:10.2106/JBJS.J.01513
5. Rogers, G. F. & Greene, A. K. Autogenous bone graft: Basic science and clinical implications. *J. Craniofac. Surg.* (2012). doi:10.1097/SCS.0b013e318241dcba
6. Carlisle, E. R. & Fischgrund, J. S. Bone Graft and Fusion Enhancement. in *Surgical Management of Spinal Deformities* (2009). doi:10.1016/B978-141603372-1.50030-5
7. Arrington, E. D., Smith, W. J., Chambers, H. G., Bucknell, A. L. & Davino, N. A. Complications of iliac crest bone graft harvesting. *Clin. Orthop. Relat. Res.* (1996). doi:10.1097/00003086-199608000-00037
8. Roberts, T. T. & Rosenbaum, A. J. Bone grafts, bone substitutes and orthobiologics the bridge between basic science and clinical advancements in fracture healing. *Organogenesis* (2012). doi:10.4161/org.23306
9. Bae, D. S. & Waters, P. M. Free Vascularized Fibula Grafting: Principles, Techniques, and Applications in Pediatric Orthopaedics. *Orthop. J. Harvard Med. Sch.* (2006).
10. Aponte-Tinao, L. A., Ayerza, M. A., Muscolo, D. L. & Farfalli, G. L. What Are the Risk Factors and Management Options for Infection After Reconstruction With Massive Bone Allografts? *Clin. Orthop. Relat. Res.* (2016). doi:10.1007/s11999-015-4353-3
11. Urban, R. M., Turner, T. M., Hall, D. J., Inoue, N. & Gitelis, S. Increased bone formation using calcium sulfate-calcium phosphate composite graft. in *Clinical Orthopaedics and Related Research* (2007). doi:10.1097/BLO.0b013e318059b902
12. Parikh, S. N. Bone graft substitutes in modern orthopedics. *Orthopedics* (2002). doi:10.3928/0147-7447-20021101-27
13. Sohn, H. S. & Oh, J. K. Review of bone graft and bone substitutes with an emphasis on fracture surgeries. *Biomaterials Research* (2019). doi:10.1186/s40824-019-0157-y
14. Chazono, M., Tanaka, T., Komaki, H. & Fujii, K. Bone formation and bioresorption after implantation of injectable β-tricalcium phosphate granules-hyaluronate complex in rabbit bone defects. *J. Biomed. Mater. Res. - Part A* (2004). doi:10.1002/jbm.a.30094
15. Sheikh, Z. *et al.* Mechanisms of in vivo degradation and resorption of calcium phosphate based biomaterials. *Materials* (2015). doi:10.3390/ma8115430
16. McKay, W. F., Peckham, S. M. & Badura, J. M. A comprehensive clinical review of recombinant human bone morphogenetic protein-2 (INFUSE® Bone Graft). *Int. Orthop.* **31**, 729–734 (2007).
17. Smucker, J. D., Rhee, J. M., Singh, K., Yoon, S. T. & Heller, J. G. Increased swelling complications associated with off-label usage of rhBMP-2 in the anterior cervical spine. *Spine (Phila. Pa. 1976).* **31**, 2813–2819 (2006).

18. Stiel, N. *et al.* Evaluation of complications associated with off-label use of recombinant human bone morphogenetic protein-2 (rhBMP-2) in pediatric orthopaedics. *J. Mater. Sci. Mater. Med.* (2016). doi:10.1007/s10856-016-5800-8
19. Cammisa, F. P. *et al.* Two-Year Fusion Rate Equivalency between Grafton® DBM Gel and Autograft in Posterolateral Spine Fusion: A Prospective Controlled Trial Employing a Side-by-Side Comparison in the Same Patient. *Spine (Phila. Pa. 1976).* (2004). doi:10.1097/01.BRS.0000116588.17129.B9
20. Dai, L. Y. & Jiang, L. S. Single-level instrumented posterolateral fusion of lumbar spine with β-tricalcium phosphate versus autograft: A prospective, randomized study with 3-year follow-up. *Spine (Phila. Pa. 1976).* (2008). doi:10.1097/BRS.0b013e3181732a8e
21. Lerner, T., Bullmann, V., Schulte, T. L., Schneider, M. & Liljenqvist, U. A level-1 pilot study to evaluate of ultraporous β-tricalcium phosphate as a graft extender in the posterior correction of adolescent idiopathic scoliosis. *Eur. Spine J.* (2009). doi:10.1007/s00586-008-0844-1
22. Smucker, J. D., Petersen, E. B. & Fredericks, D. C. Assessment of MASTERGRAFT PUTTY as a graft extender in a rabbit posterolateral fusion model. *Spine (Phila. Pa. 1976).* (2012). doi:10.1097/BRS.0b013e31824444c4
23. Smucker, J. D., Petersen, E. B., Nepola, J. V & Fredericks, D. C. Assessment of Mastergraft(®) strip with bone marrow aspirate as a graft extender in a rabbit posterolateral fusion model. *Iowa Orthop. J.* (2012).
24. Hile, D. D. *et al.* A poly(propylene glycol-co-fumaric acid) based bone graft extender for lumbar spinal fusion: In vivo assessment in a rabbit model. *Eur. Spine J.* (2006). doi:10.1007/s00586-005-1001-8
25. Chedid, M. K., Tundo, K. M., Block, J. E. & Muir, J. M. Hybrid Biosynthetic Autograft Extender for Use in Posterior Lumbar Interbody Fusion: Safety and Clinical Effectiveness. *Open Orthop. J.* (2015). doi:10.2174/1874325001509010218
26. Lewandrowski, K. U. *et al.* Augmentation of osteoinduction with a biodegradable poly(propylene glycol-co-fumaric acid) bone graft extender. A histologic and histomorphometric study in rats. *Biomed. Mater. Eng.* (1999).
27. Walsh, W. R. *et al.* Application of Resorbable Poly(Lactide- *co* -Glycolide) with Entangled Hyaluronic Acid as an Autograft Extender for Posterolateral Intertransverse Lumbar Fusion in Rabbits. *Tissue Eng. Part A* (2011). doi:10.1089/ten.TEA.2010.0008
28. Keränen, P. *et al.* Bioactive glass granules as extender of autogenous bone grafting in cementless intercalary implant of the canine femur. *Scand. J. Surg.* (2007). doi:10.1177/145749690709600310
29. Fernando, S., McEnery, M. & Guelcher, S. A. Polyurethanes for Bone Tissue Engineering. in *Advances in Polyurethane Biomaterials* (2016). doi:10.1016/B978-0-08-100614-6.00016-0
30. Guelcher, S. A. Biodegradable Polyurethanes: Synthesis and Applications in Regenerative Medicine. *Tissue Eng. Part B Rev.* **14**, 3–17 (2008).
31. McEnery, M. A. P. *et al.* Oxidatively degradable poly(thioketal urethane)/ceramic composite bone cements with bone-like strength. *RSC Adv.* **6**, 109414–109424 (2016).
32. McGough, M. A. P. *et al.* Nanocrystalline Hydroxyapatite-Poly(thioketal urethane) Nanocomposites Stimulate a Combined Intramembranous and Endochondral Ossification Response in Rabbits. *ACS Biomater. Sci. Eng.* **6**, 564–574 (2020).
33. Talley, A. D. *et al.* Remodeling of injectable, low-viscosity polymer/ceramic bone grafts

in a sheep femoral defect model. *J. Biomed. Mater. Res. - Part B Appl. Biomater.* **105**, 2333–2343 (2017).
34. Samavedi, S., Whittington, A. R. & Goldstein, A. S. Calcium phosphate ceramics in bone tissue engineering: A review of properties and their influence on cell behavior. *Acta Biomaterialia* (2013). doi:10.1016/j.proeng.2016.11.236
35. Lu, S. *et al.* Settable polymer/ceramic composite bone grafts stabilize weight-bearing tibial plateau slot defects and integrate with host bone in an ovine model. *Biomaterials* **179**, 29–45 (2018).
36. Talley, A. D., Boller, L. A., Kalpakci, K. N., Shimko, D. A. & Guelcher, C. S. A. Injectable , compression - resistant polymer / ceramic composite bone grafts promote lateral ridge augmentation without protective mesh in a canine model. *Clin. Oral Implants Res.* 592–602 (2018). doi:10.1111/clr.13257
37. Martin, J. R. *et al.* A porous tissue engineering scaffold selectively degraded by cell-generated reactive oxygen species. *Biomaterials* (2014). doi:10.1016/j.biomaterials.2014.01.026
38. McGough, M. A. *et al.* Poly (Thioketal Urethane) Autograft Extenders in an Intertransverse Process Model of Bone Formation. *Tissue Eng. Part A* (2019).
39. Boller, L., Jones, A., Cochran, D. & Guelcher, S. Compression-Resistant Polymer/Ceramic Composite Scaffolds Augmented with rhBMP-2 Promote New Bone Formation in a Nonhuman Primate Mandibular Ridge Augmentation Model. *Int J Oral Maxillofac Implant.* **35**, 616–624 (2020).
40. Dumas, J. E. *et al.* Balancing the rates of new bone formation and polymer degradation enhances healing of weight-bearing allograft/polyurethane composites in rabbit femoral defects. *Tissue Eng. Part A* **20**, 115–29 (2014).
41. Hafeman, A. E. *et al.* Characterization of the degradation mechanisms of lysine-derived aliphatic poly(ester urethane) scaffolds. *Biomaterials* **32**, 419–429 (2011).
42. Guelcher, S. *et al.* Synthesis, in vitro degradation, and mechanical properties of two-component poly(ester urethane)urea scaffolds: effects of water and polyol composition. *Tissue Eng.* **13**, 2321–2333 (2007).
43. Bodde, E. W. H., Spauwen, P. H. M., Mikos, A. G. & Jansen, J. A. Closing capacity of segmental radius defects in rabbits. *J. Biomed. Mater. Res. - Part A* (2008). doi:10.1002/jbm.a.31549
44. Wheeler, D. L., Stokes, K. E., Park, H. M. & Hollinger, J. O. Evaluation of particulate bioglass in a rabbit radius ostectomy model. *J. Biomed. Mater. Res.* (1997). doi:10.1002/(SICI)1097-4636(199705)35:2<249::AID-JBM12>3.0.CO;2-C
45. Talley, A. D. *et al.* Effects of Recombinant Human Bone Morphogenetic Protein-2 Dose and Ceramic Composition on New Bone Formation and Space Maintenance in a Canine Mandibular Ridge Saddle Defect Model. *Tissue Eng. Part A* **22**, 469–479 (2016).
46. Shiels, S. M. *et al.* Injectable and compression-resistant low-viscosity polymer/ceramic composite carriers for rhBMP-2 in a rabbit model of posterolateral fusion: A pilot study. *J. Orthop. Surg. Res.* (2017). doi:10.1186/s13018-017-0613-0
47. Dumas, J. E. *et al.* Synthesis and Characterization of an Injectable Allograft Bone/Polymer Composite Bone Void Filler with Tunable Mechanical Properties. *Tissue Eng. Part A* **16**, 2505–2518 (2010).
48. Guda, T. *et al.* In vivo performance of bilayer hydroxyapatite scaffolds for bone tissue regeneration in the rabbit radius. *J. Mater. Sci. Mater. Med.* (2011). doi:10.1007/s10856-

011-4241-7
49. Rathbone, C. R. *et al.* Effect of cell-seeded hydroxyapatite scaffolds on rabbit radius bone regeneration. *J. Biomed. Mater. Res. - Part A* (2014). doi:10.1002/jbm.a.34834
50. Guda, T. *et al.* Guided bone regeneration in long-bone defects with a structural hydroxyapatite graft and collagen membrane. *Tissue Eng. - Part A* (2013). doi:10.1089/ten.tea.2012.0057
51. Wang, W. & Yeung, K. W. K. Bone grafts and biomaterials substitutes for bone defect repair: A review. *Bioactive Materials* (2017). doi:10.1016/j.bioactmat.2017.05.007
52. Ehrler, D. M. & Vaccaro, A. R. The use of allograft bone in lumbar spine surgery. in *Clinical Orthopaedics and Related Research* (2000). doi:10.1097/00003086-200002000-00005
53. Yazar, S. Onlay Bone Grafts in Head and Neck Reconstruction. *Semin. Plast. Surg.* (2010). doi:10.1055/s-0030-1263067
54. Antheunis, H., Van Der Meer, J. C., De Geus, M., Heise, A. & Koning, C. E. Autocatalytic equation describing the change in molecular weight during hydrolytic degradation of aliphatic polyesters. *Biomacromolecules* (2010). doi:10.1021/bm100125b
55. Khan, S. N. *et al.* The biology of bone grafting. *The Journal of the American Academy of Orthopaedic Surgeons* (2005). doi:10.5435/00124635-200501000-00010
56. Parfitt, A. The physiologic and clinical significance of bone histomorphometric data. in *Bone histomorphometry: techniques and interpretations* (1983).
57. Compston, J., Skingle, L. & Dempster, D. W. Bone Histomorphometry. in *Vitamin D: Fourth Edition* (2018). doi:10.1016/B978-0-12-809965-0.00053-7
58. Sheikh, Z. *et al.* Biodegradable materials for bone repair and tissue engineering applications. *Materials* (2015). doi:10.3390/ma8095273

CHAPTER V

# CHAPTER 5: MECHANISM BY WHICH POLYMERIC DISPERSED NANOCRYSTALLINE HYDROXYAPATITE PROMOTES OSTEOGENESIS IN VITRO

**Adapted from:**

**Boller LA**, Shiels SM, Florian DC, Peck S, Schoenecker JG, Duvall C, Wenke JC, Guelcher SA. Effects of Nanocrystalline Hydroxyapatite Concentration and Skeletal Site on Bone and Cartilage Formation in Rats. *In review.*

## 5.1 Abstract

Many biomaterials-based bone regeneration strategies rely on the use of calcium phosphates such as nano-crystalline hydroxyapatite (nHA) to create bone-like scaffolds. In this study, nHA was dispersed in reactive polymers to form composite scaffolds that were evaluated *in vitro*. Matrix assays demonstrated that nHA influenced mineralization and subsequent osteogenesis in a dose-dependent manner *in vitro*. nHA dispersed in polymeric composites promoted osteogenesis via the PiT1 and Erk1/2 signaling pathway, a similar mechanism as particulated nHA.

## 5.2 Introduction

Hydroxyapatite is a naturally occurring component of bone (50 - 70 wt%).[1] Due to the inherent brittleness of ceramics, they are frequently combined with polymers to prepare composite scaffolds with improved toughness.[2] Thus, many studies have utilized nanocrystalline hydroxyapatite (nHA) composites to recapitulate the bone microenvironment in order to promote bone regeneration. [3–6] Although it is widely accepted that nHA promotes osteogenic differentiation of osteoprogenitor cells [7–12], some studies have shown small amounts of nHA stimulate chondrogenic differentiation *in vitro.* [13,14] However, the mechanism by which cells interact with nHA dispersed in polymeric composites to determine a chondrogenic or osteogenic fate is not well understood.

# CHAPTER V

Sodium phosphate (NaPi) cotransporters mediate the movement of Pi into cells. There are currently three identified NaPi transporter families, however, PiT1 and PiT2 are the only NaPi transporters expressed in bone and are thought to play a critical role in NaPi transport in osteoblasts.[15–18] Pi is a well-known factor in maintaining homeostasis in bone.[19] A recent study suggested PiT activation leading to osteogenesis in the presence of freely available nHA.[20] It has been suggested that PiT activation stimulates the extracellular signal regulated kinases (Erk1/2) as Pi has been shown to stimulate the Erk1/2 pathway. In the present study, we investigated the nHA dose response in slow-resorbing poly (ε-caprolactone urethane) (PCLUR) composites *in vitro* to determine how the differentiation of human mesenchymal stem cells (hMSCs) was influenced by nHA loading.

## 5.3 Materials and Methods

*Materials.* Crude lysine triisocyanate (LTI) was acquired from Jinan Haohua Industry Co., Ltd. (Jinan, China) and was refluxed with activated carbon prior to use. [21] nHA particles (< 200 nm) were purchased from Engi-Mat (previously nGimat, Lexington, KY).

*nHA-PCLUR 2D disk fabrication.* nHA particles were mixed with LTI for 10 min with a speed-mixer (FlackTek, Inc, Landrum, SC) to prepare a nHA-LTI prepolymer. The nHA-LTI prepolymer (0-60 wt% nHA) mixture was cured at 50°C for 3 h. nHA-LTI prepolymer was mixed with PCL300 and FeAA catalyst solution with a speed mixer for 30 s, resulting in a nHA-PCLUR crosslinked network. The nHA-PCLUR was cast into 14-mm diameter tubes, cured, and sliced into 0.5 mm films. Slowly degrading PCLUR was used as the polymeric component for *in vitro* cell culture experiments to minimize the effects of degradation of poly (thioketal urethane) (PTKUR) composites on cellular outcomes (**Figure 5.1**).

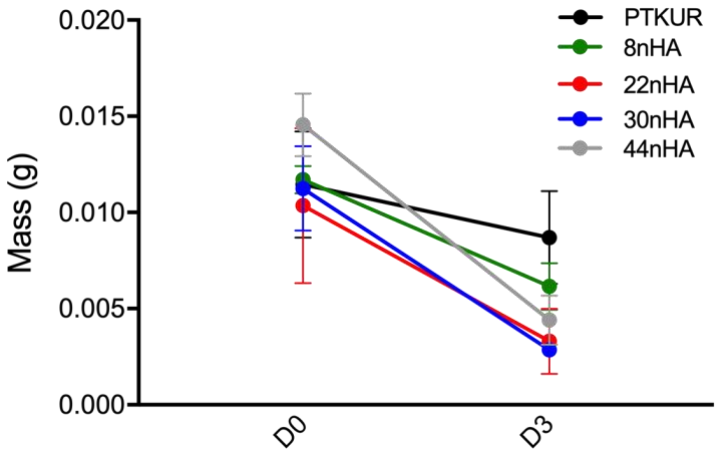


**Figure 5.1.** Degradation of nHA-PTKUR scaffolds in vitro. Mass of the samples measured at Day 0 and Day 3 after immersion in degradation medium.

*nHA-PTKUR in vitro degradation.* nHA-PTKUR scaffolds were submerged in a degradation medium composed of 20 wt% hydrogen peroxide and 0.1 M cobalt chloride dissolved in DI water. This media generated hydroxyl radicals ($OH^{\bullet}$), a reactive oxygen species produced by inflammatory cells near the defect site. [21,22] Scaffolds were immersed in media at 37°C for 3 days, dried under vacuum for 48 h, and weighed to determine the degradation rate.

*Cell Culture.* hMSCs (PromoCell) were cultured in Mesenchymal Stem Cell Growth Medium 2 (PromoCell) supplemented with 10% fetal bovine serum (FBS, Gibco) 1% antibiotic-antimycotic (Anti-anti, Gibco) at 37°C and 5% $CO_2$. Medium was changed every 3 days. Cells were detached at confluency of 80% with 0.05% Trypsin EDTA (Gibco). All subsequent *in vitro* cell culture experiments were carried out using Mesenchymal Stem Cell Growth Medium 2.

*In vitro matrix staining and analysis.* Prior to cell seeding, nHA-PCLUR films were gamma-irradiated using a dose of 25 kGY and pre-soaked overnight in medium. hMSCs were seeded at ($50 \times 10^6$ cells $mL^{-1}$) onto nHA-PCLUR films. For the Alizarin Red S assay, cell-laden films were washed at their respective time points with phosphate-buffered saline (PBS), fixed in 10% formalin, and stained with Alizarin Red S ($20 \times 10^{-3}$ M). Films were washed with DI water

and remaining bound Alizarin Red S dye was extracted with Sodium Dodecyl Sulfate (5%). Absorbance of the extracted dye was read at optical density 540 nm, and dye extracted from cell-free nHA-PCLUR films served as blank controls. For the von Kossa assay, cell-laden films were washed at their respective timepoints with PBS and placed in a silver nitrate solution (5%) for 10 min in the dark. Films were then immersed in a sodium carbonate/formaldehyde solution, rinsed with water, immersed in Farmer's reducer, and subsequently counter stained with Toluene Blue (2%). Area% mineralization (black nodule staining) was quantified using NIH ImageJ. For the Alcian Blue Assay, cell laden films were washed at their respective timepoints with PBS and stained using Alcian Blue 8GX (1%). Films were then washed with DI water and remaining bound Alcian Blue dye was extracted with 4M guanidine HCl. Absorbance of the extracted Alcian Blue dye was read at optical density 615 nm and dye extracted from cell-free nHA-PCLUR films served as blank controls. Images for all matrix stains were taken with a reflected-light microscope (Zeiss Axioscope 5).

*Fluorescent imaging and Fourier Resonance Energy Transfer (FRET) analysis.* hMSCs seeded on nHA-PCLUR films were stained for PiT1 (ab237527, Abcam), PiT2 (sc-377326, Santa Cruz Biotechnology), and FGFR2 (ab58201, Abcam). Primary antibodies were applied at 1:100 dilution overnight at 4°C. Detection via confocal microscopy (Carl Zeiss 710) was performed using secondary antibodies labeled with Alexa Flour 488 and Alexa Flour 568 at 1:200 dilution. Immunofluorescent intensity analysis was performed with FIJI Image J (NIH) and measured as corrected total cell fluorescence. Photobleaching FRET experiments with PiT1(Alexa Flour 488) and FGFR2 (Alexa Flour 568) were performed by exciting the fluor with the 561 nm laser 300 times with 100% laser power. The fluorescence intensity of the donor fluor was measured before

and after photobleaching of the acceptor, and energy transfer efficiency was calculated using these values.

*Western Blot analysis.* hMSCs were scraped from nHA-PCLUR films and homogenized in RIPA buffer supplemented with protease and phosphatase inhibitors (Thermo Scientific). Proteins were separated with (12%) gel, transferred to a nitrocellulose membrane, and stained with primary antibodies for phospho-p44/42 MAPK (ERK1/2) (9101, Cell Signaling Technology) and p44/42 MAPK (9102, Cell Signaling Technology) overnight at 4°C. Signal detection was performed with Western ECL Substrate (Bio-rad). Bands were analyzed using densitometry via Image J (NIH). Mouse β-tubulin (2146, Cell Signaling Technology) was used as a loading control.

*Statistical analysis.* All Immunofluorescence images were acquired with the same parameters. Data were analyzed utilizing GraphPad Prism (Version 8.4.1) and reported as mean ± standard deviation. Treatment groups compared over time (% nHA vs. time) were compared using a two-way ANOVA with Tukey's multiple comparison test. Statistical significance was set at $p<0.05$.

## 5.4 Results

*nHA dose influences osteogenesis in vitro.* To better understand the effects of nHA on mineralization, Alizarin Red S and von Kossa staining assays (**Figure 5.2A**) were performed on hMSC-laden nHA-PCLUR films. Alizarin Red S-stained films were measured with spectrophotometer at 540 nm wavelength. By Day 3, a significant difference in mineralization was observed in ≥45nHA groups compared with ≤15nHA groups. A continued significant difference in mineralization was observed in ≥45nHA groups throughout the duration of the time course. During days 1- 14, an increase in intensity of Alizarin Red staining was seen in all groups with peak intensity at Day 14 for all groups except the PCLUR control (**Figure 5.2B**).

Additionally, von Kossa staining was also performed to assess the formation of mineralized nodules. Similar to Alizarin Red data, the area% nodules indicated that nHA increased osteogenesis of the hMSCs in a dose-dependent manner. At Day 21, a significant increase in nodules was observed between the PCLUR group and ≥45nHA groups (**Figure 5.2C**). To evaluate chondrogenesis in hMSCs seeded on nHA-PCLUR films, glycosaminoglycan (GAG) content was evaluated by Alcian blue staining. The cells did not phenotypically resemble chondrocytes (**Figure 5.2A**), and no significant differences were seen between groups at the respective timepoints (**Figure 5.2D**).

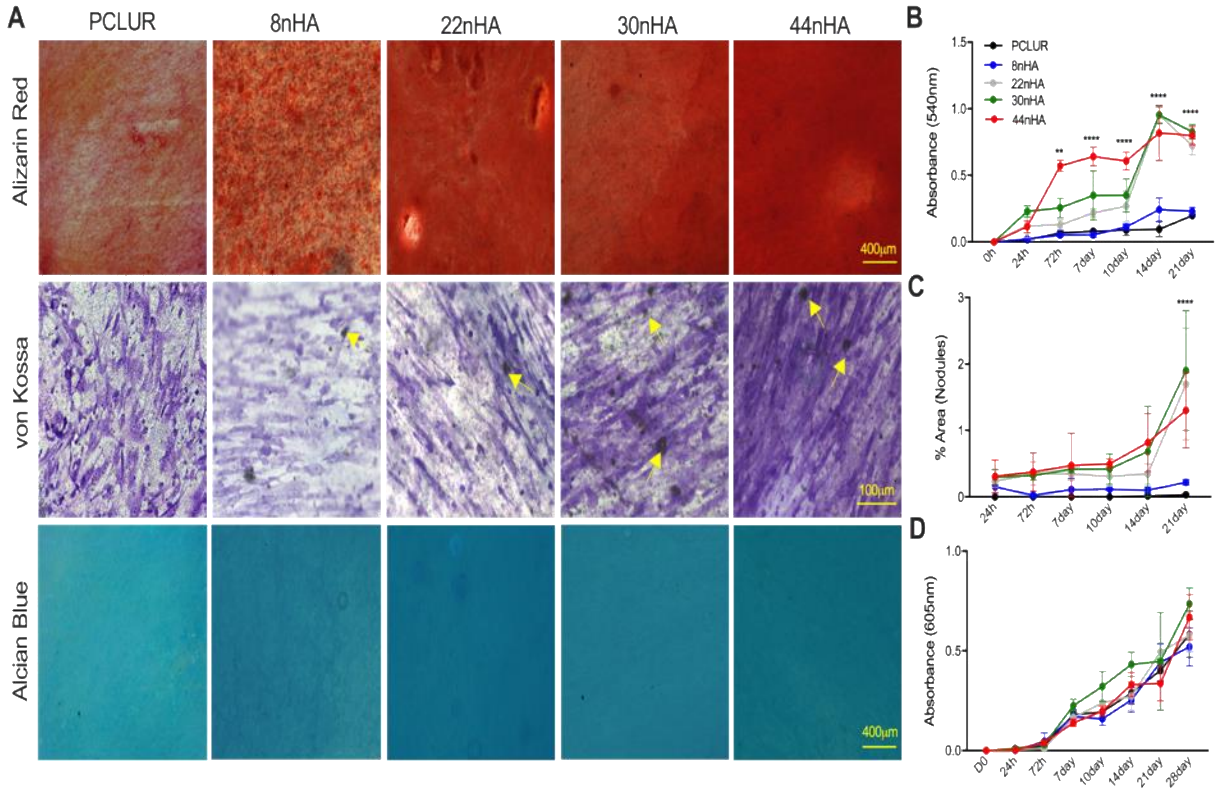


**Figure 5.2.** Effect of nHA on osteogenic and chondrogenic differentiation of hMSCs. (A) Representative images of Alizarin Red S stained hMSCs at D14 (4X), von Kossa and Toluene Blue stained hMSCs at D14 (yellow arrows indicate von Kossa nodules) (20X), and Alcian Blue stained hMSCs at D14 (4X). (B) Absorbance of extracted Alizarin Red S dye read at 540nm. (C) Quantification of von Kossa nodules. (D) Absorbance of extracted Alcian Blue dye read at 605nm. Statistical significance of mineralization at various time points tested using Two Way ANOVA, *p<0.05, **p<0.01, ***p<0.001, **** p<0.0001.

*Expression of PiT and FGFR2 change in response to nHA in vitro.* Immunofluorescent staining was performed on Sodium-dependent Phosphate Transporter 1 (SLC20a1/PiT1), Sodium-dependent Phosphate Transporter 2 (SLC20a2/PiT2), and Fibroblast Growth Factor Receptor-2 (FGFR2) to better understand the mechanism by which nHA stimulates differentiation. Immunofluorescence intensity of PiT1 in hMSCs seeded on nHA-PTKUR films increased in all nHA containing groups by 72 h compared with PCLUR (**Figure 5.3A**). Similarly, FGFR-2 intensity in hMSCs seeded on nHA-PTKUR films increased in all nHA containing groups by 72 h compared with PCLUR (**Figure 5.3B**). No positive detection of PiT2 staining was observed within any of the groups. FRET experiments to characterize the interaction of PiT1 and FGFR2 revealed no colocalization of PiT1 and FGFR2 (**Figure 5.3C**).

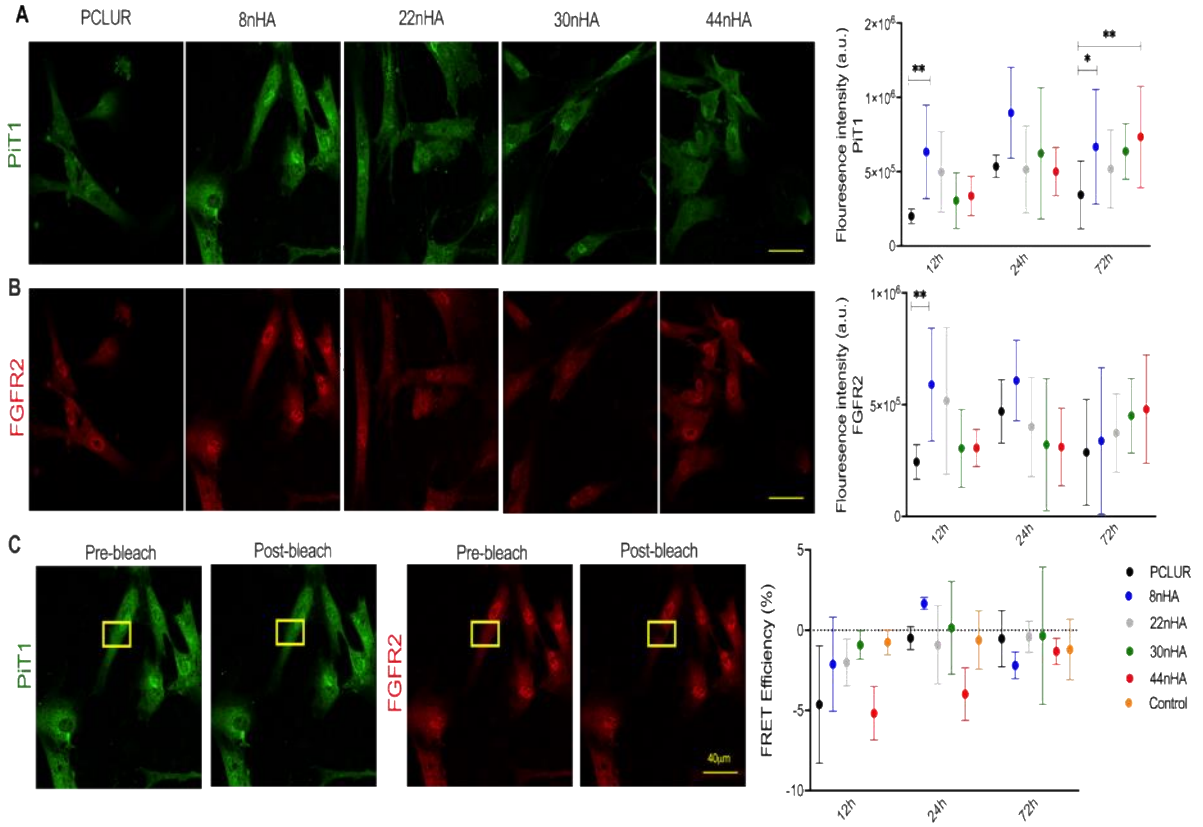


**Figure 5.3.** Effect of nHA on PiT1, PiT2, and FGFR activation and colocalization in vitro. (A) Representative images of immunofluorescent staining for PiT1 (green) and (B) FGFR-2 (red) performed on hMSCs seeded on nHA-PCLUR films for 12 h (40X). Immunofluorescence intensity measured as corrected total cell fluorescence of (A) PiT1 and (B) FGFR-2 in hMSCs seeded on nHA-PCLUR films for 12, 24, and 72 h. (C) FRET measured by acceptor photobleaching in hMSCs seeded on nHA-PCLUR films for, 12, 24, and 72 h. FRET efficiency was determined by acceptor photobleaching method and was measured only in the bleached area. Statistical significance of immunofluorescent materials dependent on nHA evaluated using Two-way ANOVA, *p<0.05, **p<0.01.

*nHA stimulates downstream Erk1/2 signaling*. Western blots were performed to determine if polymer-bound nHA stimulated Erk1/2 signaling at 12, 24, and 72 h (**Figure 5.4A**). Phosphorylation of p44/42 MAPK (Erk1/2) was measured over time. An increase in phosphorylation of Erk1/2 between the nHA groups at 12 h was observed. Interestingly, at 24 h a slight decrease in phosphorylation occurred and there were no significant differences between groups; however, at 72 h there was a significant increase in Erk1/2 phosphorylation in all nHA groups (**Figure 5.4B**).

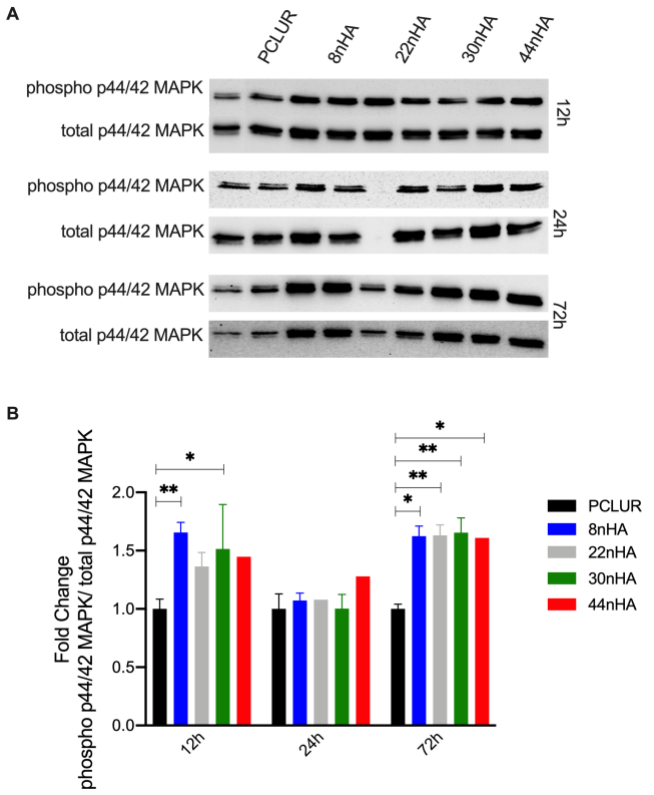


**Figure 5.4.** Effect of nHA on Erk1/2 signaling. (A) Representative western blots of Erk1/2 phosphorylation in hMSCs seeded on nHA-PCLUR films at 12, 24, and 72h timepoints. (B) Quantification of and relative fold change of phospho p44/42 MAPK/ total p44/42 MAPK band densities at respective time points. Bands normalized to PCLUR. β-Tubulin used as a loading control for all analysis. Statistical significance of fold change dependent on nHA evaluated using Two-way ANOVA, *p<0.05, **p<0.01.

## 5.5 Discussion

In this study, we investigated the mechanism by which nHA induces osteoblast differentiation *in vitro* and assessed cartilage and bone formation in nHA-PTKUR composites in response to nHA loading and implantation site in rats. nHA dispersed in polymeric composites at loadings >22 wt% induced osteoblast differentiation *in vitro* via the PiT1 and Erk1/2 signaling pathways, similar to a previous study using aqueous dispersions of nHA powders. [20]

hMSCs have the ability to differentiate into mesoderm-type cells including osteoblasts, chondrocytes, and adipocytes. [22] Multiple investigations have suggested that calcium (Ca) and phosphate (Pi) precipitated from nHA and other calcium phosphates are involved in upregulation of osteogenic gene expression. [23–25] In this study, hMSC osteogenic differentiation increased in a

nHA dose-dependent manner, which is in agreement with a previous study using collagen scaffolds. [26] The early induction (day 3) of mineralization seen with Alizarin Red in the ≥ 22nHA groups further confirmed the osteogenic potential of nHA. In contrast with a recent study reporting that low concentrations of nHA may contribute to chondrogenesis [13], we found that GAG formation was independent of nHA content. Furthermore, the cells cultured on nHA-PTKUR substrates did not phenotypically resemble chondrocytes.

Calcium-sensing receptors [27] and a family of sodium dependent phosphate transporters (PiTs) [28] can bind to nHA. hMSCs seeded on nHA-PCLUR films demonstrated increased fluorescence for PiT1 as early as 12 h *in vitro*. By 72 h these differences were significant, consistent with the onset of increased mineralization seen by Alizarin Red staining. In contrast, hMSCs seeded on PCLUR exhibited significantly lower fluorescent intensity for PiT1 at 72 h. These findings are consistent with previous studies reporting that PiT1/SLC20a1 plays a role in nHA signaling. [20,29,30] Additionally, FGFRs are activated by increased Pi [31,32] and are involved in fracture healing. [33] Specifically, FGFR1 and FGFR2 are highly expressed in osteoprogenitors and osteoblasts. [34] A previous study established that both FGFR and PiT signaling are required for nHA-mediated osteoblast differentiation. A decrease in FGFR2 gene expression in hMSCs was observed at 24 h in response to nHA treatment compared with untreated cells. [20] Herein, we observed a similar trend in response to >22nHA at 24 h. Furthermore, we determined that PiT1 and FGFR2 do not colocalize suggesting that they are not located in the same subcellular structures and are not simultaneously activated by nHA.

Pi-mediated osteogenesis is dependent on the MAPK Erk1/2 pathway [35], which is essential for osteoblast differentiation and inhibition of ectopic cartilage formation in the perichondrium. [35] Furthermore, inhibition of Erk1/2 may promote chondrogenesis. [36] Herein, nHA loadings >8 wt%

enhanced Erk1/2 signaling. These findings show that nHA dispersed in polymeric composites induced osteoblast differentiation and mineralization through PiT1 and Erk1/2 signaling at low loadings (>8 wt%).

## 5.6 Conclusion

This study demonstrated that nHA has a dose-dependent effect on mineralization *in vitro*. Furthermore, nHA increased PiT1 signaling and downstream Erk1/2 signaling. Together, these results provided evidence that nHA promotes osteogenic differentiation in a dose-dependent manner. Understanding the mechanism by which embedded nHA functions *in vitro* can influence future design of nHA composites for *in vivo* studies.

References


1. Clarke, B. Normal bone anatomy and physiology. *Clin. J. Am. Soc. Nephrol.* (2008). doi:10.2215/CJN.04151206
2. Wagoner Johnson, A. J. & Herschler, B. A. A review of the mechanical behavior of CaP and CaP/polymer composites for applications in bone replacement and repair. *Acta Biomaterialia* (2011). doi:10.1016/j.actbio.2010.07.012
3. Bal, Z., Kaito, T., Korkusuz, F. & Yoshikawa, H. Bone regeneration with hydroxyapatite-based biomaterials. *Emergent Mater.* (2019). doi:10.1007/s42247-019-00063-3
4. Guda, T. *et al.* In vivo performance of bilayer hydroxyapatite scaffolds for bone tissue regeneration in the rabbit radius. *J. Mater. Sci. Mater. Med.* (2011). doi:10.1007/s10856-011-4241-7
5. Guda, T. *et al.* Guided bone regeneration in long-bone defects with a structural hydroxyapatite graft and collagen membrane. *Tissue Eng. - Part A* (2013). doi:10.1089/ten.tea.2012.0057
6. Kattimani, V. S., Kondaka, S. & Lingamaneni, K. P. Hydroxyapatite–-Past, Present, and Future in Bone Regeneration. *Bone Tissue Regen. Insights* (2016). doi:10.4137/btri.s36138
7. Ha, S. W., Jang, H. L., Nam, K. T. & Beck, G. R. Nano-hydroxyapatite modulates osteoblast lineage commitment by stimulation of DNA methylation and regulation of gene expression. *Biomaterials* (2015). doi:10.1016/j.biomaterials.2015.06.039
8. Shu, R., McMullen, R., Baumann, M. J. & McCabe, L. R. Hydroxyapatite accelerates differentiation and suppresses growth of MC3T3-E1 osteoblasts. *J. Biomed. Mater. Res. - Part A* (2003). doi:10.1002/jbm.a.20021
9. Wutticharoenmongkol, P., Pavasant, P. & Supaphol, P. Osteoblastic phenotype expression of MC3T3-E1 cultured on electrospun polycaprolactone fiber mats filled with hydroxyapatite nanoparticles. *Biomacromolecules* (2007). doi:10.1021/bm700451p
10. Wang, X. F. *et al.* Nano hydroxyapatite particles promote osteogenesis in a three-dimensional bio-printing construct consisting of alginate/gelatin/hASCs. *RSC Adv.* (2016). doi:10.1039/c5ra21527g
11. Lee, J. H. *et al.* Enhanced Osteogenesis by Reduced Graphene Oxide/Hydroxyapatite Nanocomposites. *Sci. Rep.* (2015). doi:10.1038/srep18833
12. Wang, H. *et al.* Biocompatibility and osteogenesis of biomimetic nano-hydroxyapatite/polyamide composite scaffolds for bone tissue engineering. *Biomaterials* (2007). doi:10.1016/j.biomaterials.2007.04.014
13. Wang, Y., Wu, S., Kuss, M. A., Streubel, P. N. & Duan, B. Effects of Hydroxyapatite and Hypoxia on Chondrogenesis and Hypertrophy in 3D Bioprinted ADMSC Laden Constructs. *ACS Biomater. Sci. Eng.* (2017). doi:10.1021/acsbiomaterials.7b00101
14. Spadaccio, C. *et al.* Poly-l-lactic acid/hydroxyapatite electrospun nanocomposites induce chondrogenic differentiation of human MSC. *Ann. Biomed. Eng.* (2009). doi:10.1007/s10439-009-9704-3
15. Montessuit, C., Bonjour, J. P. & Caverzasio, J. Expression and Regulation of Na-Dependent Pi Transport in Matrix Vesicles Produced by Osteoblast-like Cells. *J. Bone Miner. Res.* (1995). doi:10.1002/jbmr.5650100416
16. Nielsen, L., Pedersen, F. & L, P. Expression of type III sodium-dependent phosphate

transporters/retroviral receptors mRNAs during osteoblast differentiation. *Bone* **28**, 160–166 (2001).
17. Collins, J. F., Bai, L. & Ghishan, F. K. The SLC20 family of proteins: Dual functions as sodium-phosphate cotransporters and viral receptors. *Pflugers Archiv European Journal of Physiology* (2004). doi:10.1007/s00424-003-1088-x
18. Beck, G. R., Zerler, B. & Moran, E. Phosphate is a specific signal for induction of osteopontin gene expression. *Proc. Natl. Acad. Sci.* (2002). doi:10.1073/pnas.140021997
19. Penido, M. G. M. G. & Alon, U. S. Phosphate homeostasis and its role in bone health. *Pediatric Nephrology* (2012). doi:10.1007/s00467-012-2175-z
20. Ha, S. W., Park, J., Habib, M. M. & Beck, G. R. Nano-Hydroxyapatite Stimulation of Gene Expression Requires Fgf Receptor, Phosphate Transporter, and Erk1/2 Signaling. *ACS Appl. Mater. Interfaces* (2017). doi:10.1021/acsami.7b12029
21. McEnery, M. A. P. *et al.* Oxidatively degradable poly(thioketal urethane)/ceramic composite bone cements with bone-like strength. *RSC Adv.* **6**, 109414–109424 (2016).
22. Abdallah, B. M. & Kassem, M. Human mesenchymal stem cells: From basic biology to clinical applications. *Gene Therapy* (2008). doi:10.1038/sj.gt.3303067
23. Chai, Y. C., Roberts, S. J., Schrooten, J. & Luyten, F. P. Probing the osteoinductive effect of calcium phosphate by using an in vitro biomimetic model. *Tissue Eng. - Part A* (2011). doi:10.1089/ten.tea.2010.0160
24. Khoshniat, S. *et al.* Phosphate-dependent stimulation of MGP and OPN expression in osteoblasts via the ERK1/2 pathway is modulated by calcium. *Bone* (2011). doi:10.1016/j.bone.2010.12.002
25. Barradas, A. M. C. *et al.* Molecular mechanisms of biomaterial-driven osteogenic differentiation in human mesenchymal stromal cells. *Integr. Biol. (United Kingdom)* (2013). doi:10.1039/c3ib40027a
26. Cunniffe, G. M., Curtin, C. M., Thompson, E. M., Dickson, G. R. & O'Brien, F. J. Content-Dependent Osteogenic Response of Nanohydroxyapatite: An in Vitro and in Vivo Assessment within Collagen-Based Scaffolds. *ACS Appl. Mater. Interfaces* (2016). doi:10.1021/acsami.6b06596
27. Goltzman, D. & Hendy, G. N. The calcium-sensing receptor in bone-mechanistic and therapeutic insights. *Nature Reviews Endocrinology* (2015). doi:10.1038/nrendo.2015.30
28. Biber, J., Hernando, N. & Forster, I. Phosphate Transporters and Their Function. *Annu. Rev. Physiol.* (2013). doi:10.1146/annurev-physiol-030212-183748
29. Bon, N. *et al.* Phosphate (p i )-regulated heterodimerization of the highaffinity sodium-dependent p i transporters pit1/slc20a1 and pit2/slc20a2 underlies extracellular p i sensing independently of p i uptake. *J. Biol. Chem.* (2018). doi:10.1074/jbc.M117.807339
30. Shih, Y. R. V. *et al.* Calcium phosphate-bearing matrices induce osteogenic differentiation of stem cells through adenosine signaling. *Proc. Natl. Acad. Sci. U. S. A.* (2014). doi:10.1073/pnas.1321717111
31. Yamazaki, M. *et al.* Both FGF23 and extracellular phosphate activate Raf/MEK/ERK pathway via FGF receptors in HEK293 cells. *J. Cell. Biochem.* (2010). doi:10.1002/jcb.22842
32. Nishino, J. *et al.* Extracellular Phosphate Induces the Expression of Dentin Matrix Protein 1 Through the FGF Receptor in Osteoblasts. *J. Cell. Biochem.* (2017). doi:10.1002/jcb.25742
33. Dimitriou, R., Tsiridis, E. & Giannoudis, P. V. Current concepts of molecular aspects of

bone healing. *Injury* (2005). doi:10.1016/j.injury.2005.07.019
34. Jacob, A. L., Smith, C., Partanen, J. & Ornitz, D. M. Fibroblast growth factor receptor 1 signaling in the osteo-chondrogenic cell lineage regulates sequential steps of osteoblast maturation. *Dev. Biol.* (2006). doi:10.1016/j.ydbio.2006.05.031
35. Matsushita, T. *et al.* Extracellular Signal-Regulated Kinase 1 (ERK1) and ERK2 Play Essential Roles in Osteoblast Differentiation and in Supporting Osteoclastogenesis. *Mol. Cell. Biol.* (2009). doi:10.1128/mcb.01549-08
36. Li, J. *et al.* MEK/ERK and p38 MAPK regulate chondrogenesis of rat bone marrow mesenchymal stem cells through delicate interaction with TGF-β1/Smads pathway. *Cell Prolif.* (2010). doi:10.1111/j.1365-2184.2010.00682.x

# CHAPTER VI

# CHAPTER 6: EFFECTS OF NANOCRYSTALLINE HYDROXYAPATITE CONCENTRATION AND SKELETAL SITE ON BONE AND CARTIALGE IN RATS

**Adapted from:**

**Boller LA**, Shiels SM, Florian DC, Peck S, Schoenecker JG, Duvall C, Wenke JC, Guelcher SA. Effects of Nanocrystalline Hydroxyapatite Concentration and Skeletal Site on Bone and Cartilage Formation in Rats. *In review*..

## 6.1 Abstract

Most fractures heal by a combination of endochondral and intramembranous ossification dependent upon strain and vascularity at the fracture site. In this study, nHA was dispersed in reactive polymers to form a composite 3D tissue engineered scaffold that were evaluated *in vivo*. Scaffolds were implanted into a 2-mm defect in the femoral diaphysis or metaphysis of Sprague-Dawley rats to evaluate new bone formation at 4 and 8 weeks. Two formulations were tested: a poly (thioketal) urethane scaffold without nHA (PTKUR) and a PTKUR scaffold augmented with 22 wt% nHA (22nHA). The scaffolds supported new bone formation in both anatomic sites. In the metaphysis, augmentation of scaffolds with nHA promoted an intramembranous healing response. Within the diaphysis, nHA inhibited endochondral ossification. Immunohistochemistry was performed on cryo-sections of the bone/scaffold interface in which CD146, CD31, Endomucin, CD68, and Myeloperoxidase were evaluated. No significant differences in the infiltrating cell populations were observed. These findings suggest that nHA dispersed in polymeric composites induces osteogenic differentiation of adherent endogenous cells, which has skeletal site-specific effects on fracture healing.

## 6.2 Introduction

Fracture healing occurs through two processes after initial trauma. Primary healing, or intramembranous ossification, takes place when progenitor cells undergo direct differentiation into osteoblasts followed by subsequent ossification and Haversian remodeling. This process occurs

when the fracture gap is minimal and the defect site is both stable and sufficiently vascularized. [1,2] Secondary healing, or endochondral ossification, occurs when bone forms through an intermediate cartilaginous callus. [3,4] Hypertrophic chondrocytes within the callus contribute to new bone formation either by undergoing programmed cell death allowing for resorption, vascularization, and osteogenesis [5] or by transdifferentiating directly into osteoblasts and osteocytes. [6] Endochondral ossification often takes place in fractures with significant strain and can occur with limited initial vascularization. [3] Most fractures, however, heal by a combination of both intramembranous and endochondral ossification due to the variable amounts of vascularity and strain in the fracture microenvironment. [3,7]

Recapitulating natural fracture healing *in vivo* remains a limitation in biomaterial-based bone regeneration strategies. Current approaches to bone regeneration typically promote intramembranous ossification through the use of osteoconductive and osteoinductive biomaterials [8,9] and are not designed for the specific anatomic conditions or site at which they are being used, which can lead to unsatisfactory healing. Therefore, there has been increasing interest in biomaterials-based strategies that promote endochondral ossification, including chondrogenic priming of scaffolds [10,11], mechanical loading [12], and aligned pore architectures. [13] However, little is understood about how material composition influences the mechanisms by which new bone is formed.

Poly (thioketal urethane) (PTKUR)-based composites have been shown to support new bone formation *in vivo* [14]. In a recent study evaluating nHA-PTKUR cements in a metaphyseal femoral defect in rabbits, intramembranous ossification on the periphery of the cement and endochondral ossification in the hypoxic interior was observed. [15] PTKURs degrade in response to reactive oxygen species (ROS) secreted by infiltrating cells. [16,17] Thus, a hypoxic environment

along with macrophages and osteoclasts present in bone are anticipated to promote endochondral ossification; however, it is not understood how nHA affects PTKUR degradation or how degradation varies at different anatomic sites within the bone.

Matrix staining and the effects of nHA on membrane bound receptors and subsequent signaling pathways were evaluated *in vitro*. Subsequently, we implanted 3D nHA-PTKUR scaffolds in both femoral diaphyseal and metaphyseal models of bone regeneration to evaluate new bone formation and the mechanism by which it formed at both 4 and 8 weeks. *In vivo* outcomes were assessed by μCT, histology, and histomorphometry. Additionally, the population of host cells infiltrating the nHA-PTKUR scaffolds were characterized by immunohistochemistry (IHC) in frozen sections [18,19].

## 6.3 Materials and Methods

*Materials.* Crude lysine triisocyanate (LTI) was acquired from Jinan Haohua Industry Co., Ltd. (Jinan, China) and was refluxed with activated carbon prior to use [16]. Materials for thioketal diol (TK) synthesis, poly(ε-caprolactone) triol (PCL, 300 g $mol^{-1}$), and iron (III) acetylacetonate (FeAA) catalyst were purchased from Sigma-Aldrich. A catalyst solution was prepared from FeAA (5 wt%) dissolved in vacuum-dried ε -caprolactone. nHA particles (< 200 nm) were purchased from Engi-Mat (previously nGimat, Lexington, KY).

*TK diol synthesis.* TK diol (MW = 196 g $mol^{-1}$) was synthesized following a previously published method [14]. Briefly, thioglycolic acid and 2,2-dimethoxypropane were reacted with bismuth (III) chloride for 24 h at room temperature and dried for 24 h under vacuum. The intermediate was dissolved in tetrahydrofuran and added to lithium aluminum hydride ($LiAlH_4$) in diethyl ether at 0°C. The reaction was refluxed at 52°C overnight. $LiAlH_4$ was quenched and the final product was filtered using aqueous NaOH and diethyl ether. The aqueous layer was removed

using a separation funnel and sodium sulfate. After filtering, solvent was removed from the product using rotary evaporation, and the product was dried under vacuum for 24 h.

*Fabrication of 3D nHA-PTKUR scaffolds.* 3D-printed scaffolds were fabricated following a previously published method. [20] 4 mm x 3 mm wax molds with trabecular structure mimicking that of the trabeculae of the femoral head were 3D printed. nHA-LTI pre-polymer, TK diol, and FeAA catalyst were mixed to yield a reactive nHA-PTKUR composite that was injected into the mold. The material-filled wax molds were cured at 50°C for 12 h. After curing, the wax molds were leached from the nHA-PTKUR scaffolds with acetone. The resulting cylindrical scaffolds were 3 mm Ø x 2 mm.

*nHA-PTKUR scaffold characterization*. nHA-PTKUR scaffolds (n=3) were tested in uniaxial compression mode (Instron DynaMight 8800 Servohydraulic Test System). The displacement rate was kept at a constant 1.3 mm $min^{-1}$, and compression was continued until failure. Force-displacement curves were obtained and converted to stress-strain curves to determine elastic modulus, maximum strength, and yield strain and strength for each construct. For imaging, scaffolds were gold sputter-coated and imaged using scanning electron microscopy (Carl Zeiss Inc.) equipped with Everhart-Thornley detector for topographical imaging.

*In vivo implantation of nHA-PTKUR scaffolds in rats.* All surgical and care procedures were approved by the Institutional Animal Care and Use Committee of the US Army Institute of Surgical Research, Fort Sam Houston, TX. Procedures were performed in compliance with the Animal Welfare Act, Animal Welfare Regulations, and the Guide for the Care and Use of Laboratory Animals. Male mature Sprague-Dawley rats were used in this study (n=80, 368±2g). Animals were premedicated with slow-release Buprenorphine (0.1 mg $kg^{-1}$) an anesthetized using gaseous isoflurane (1-3%). Animals were randomly assigned to one of two different anatomic site

models: femoral diaphysis or femoral metaphysis. For both groups, the animal's hindlimbs were shaved and prepared for sterile surgery using alternating washes of alcohol and povidone-iodine.

The diaphyseal defect model and fixation method were followed as previously described [23]. Briefly, the femoral shaft was exposed and a polyacetyl plate placed on the anterolateral surface of the femur. The plate was attached with a threaded Kirschner wire and a 2-mm mid-diaphyseal full-thickness defect made with a small oscillating saw under continuous irrigation with saline. Animals were randomly assigned a treatment group (**Table 6.1**) and received a scaffold (3 mm Ø x 2 mm) within the defect. For the metaphyseal defect, a medial skin incision was made over the right femur, the vastus medialis and gracillis muscles separated, and the distal end of the femur exposed. A 1-mm pilot hole was made through the medial epicondyle. A 3 mm Ø x 2 mm defect was created and flushed with saline, and either a PTKUR or 22nHA scaffold was placed into the defect. The procedure was repeated on the left leg, and the opposite scaffold composition was inserted (**Figure 6.1**). Animals recovered for 4 or 8 weeks.

**Table 6.1.** Treatment groups evaluated in rat diaphyseal and femoral metaphyseal defects.

| | Component wt% | | # of replicates | | | |
|---|---|---|---|---|---|---|
| Group | nHA (prepolymer) | nHA (total scaffold) | 4 wks-diaphyseal | 8 wks-diaphyseal | 4 wks-metaphyseal | 8 wks-metaphyseal |
| PTKUR | 0 | 0 | 8 | 8 | 8 | 8 |
| 8nHA | 15 | 8.4 | 4 | 4 | 0 | 0 |
| 22nHA | 35 | 22.2 | 8 | 8 | 8 | 8 |
| 30nHA | 45 | 30.5 | 4 | 4 | 0 | 0 |
| | | | Total: 80 | | | |

Animals were anesthetized and euthanized at their designated time-point with an overdose of pentobarbital. The femora were harvested and flash frozen in liquid nitrogen. After flash freezing, all K-wire pins were removed from the femora.

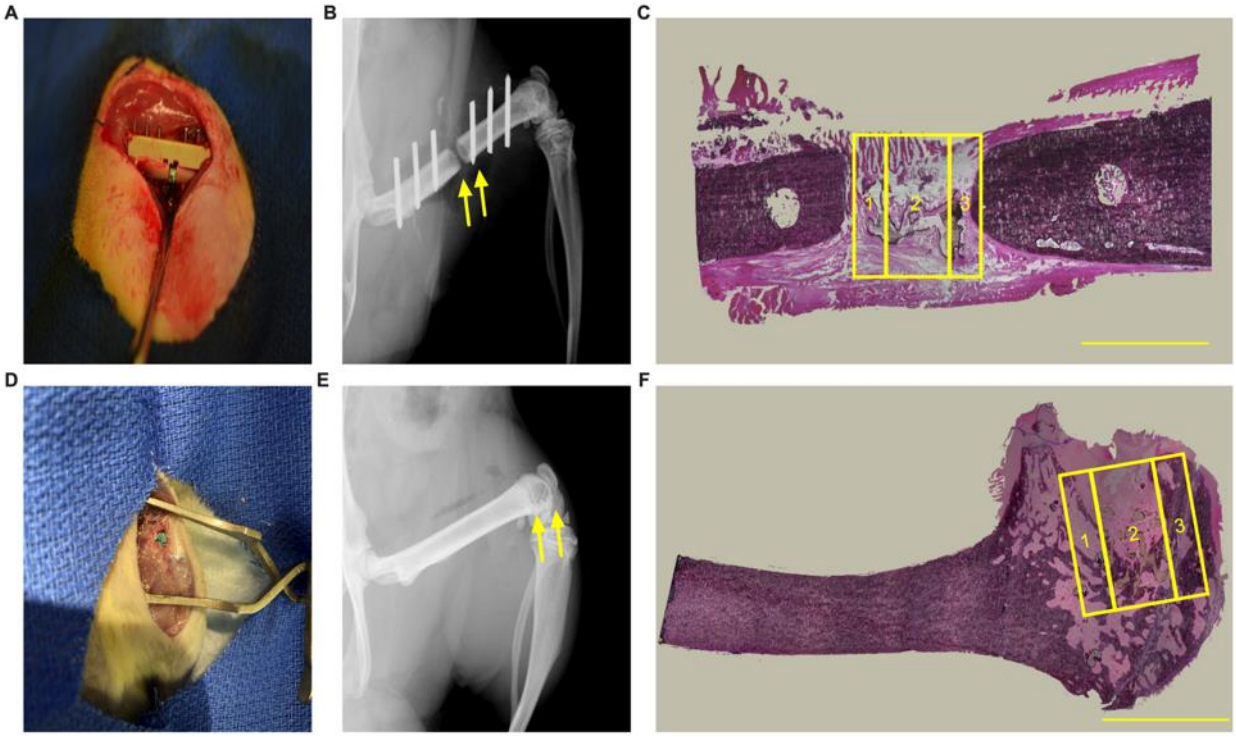


**Figure 6.1.** Surgical images. (A) Representative image of nHA-PTKUR scaffold in diaphyseal surgical site. (B) Representative X-ray image of diaphysis, yellow arrows indicate defect. Light opacity observed in the defect space from nHA in nHA-PTKUR scaffolds. (C) A schematic representation of the regions of interest (ROI) utilized for histomorphometric and spatial analysis within the diaphysis. D) Representative image of nHA-PTKUR scaffold in metaphyseal surgical site. (E) Representative X-ray image of metaphysis. Yellow arrows indicate defect. Light opacity observed in the defect space from nHA in nHA-PTKUR scaffolds. (F) A schematic representation of the regions of interest (ROI) utilized for histomorphometric and spatial analysis within the metaphysis. Scale bars, 2mm.

*In vivo histological and immunohistochemical (IHC) staining and analysis.* Samples used for all histological analysis were embedded in SCEM compound (SECTION-LAB Co. Ltd.) and cut longitudinally into 5-µm sections with a cryostat (Leica CM1850). Hematoxylin and Eosin (H&E) staining was performed for visualization of cellular and tissue structure (SECTION-LAB Co. Ltd.). Von Kossa staining was performed for analysis of new bone within the defect. Safranin O was performed to visualize regions of cartilage within the sample with Fast Green used as a counter stain for bone. Sections were imaged via bright-field microscopy (Olympus BX41).

IHC staining for CD68 (Ab31630, Abcam), CD146 (Ab75769, Abcam), Endomucin (Orb100879, Biorbyt), CD31 (ab24590, Abcam), and Myeloperoxidase (Ab9535, Abcam) was

performed at 1:100 dilution. All primary antibodies were diluted in and incubated overnight at 4$^{o}$C. Appropriate secondary antibodies were applied for 1 h at room temperature and DAB substrate kit (Thermo Scientific) was used for detection via bright-field microscopy (Olympus BX41). Hematoxylin counterstaining was used for all IHC samples. 20X magnification images were acquired and positively stained cells were counted using FIJI ImageJ. IHC+ cells were reported as a percentage of the total number of cells present within the image.

For quantitative histomorphometry, images were taken at 4X via bright-field microscopy (Olympus BX41). The area of interest (AOI) was defined as a 2 mm x 3 mm rectangular region that encompassed the full scaffold and defect space. Quantification was performed using Metamorph (Version 7.0.1). Bone was thresholded as black stain in the von Kossa sections and cartilage was thresholded as orange in the Safranin O sections. Bone and cartilage within the defect were reported as an area percentage of the total AOI (**Figure 6.1).**

*µCT analysis.* Femora that were utilized for µCT were placed into formalin and were scanned at 70 kVp energy, 200 µA source current, 1000 projections per rotation, 800 ms integration time, and 17.2 µm voxel size using a µCT50 (SCANCO). The defect region was contoured to quantitatively assess the morphometric parameters, bone volume density (BV/TV), trabecular thickening (Tb.Th.), trabecular spacing (Tb.Sp.), and trabecular number (Tb. N.).

*Statistical Analysis.* Data were analyzed utilizing GraphPad Prism (Version 8.4.1) and reported as mean ± standard deviation. Treatment groups at singular time points or singular anatomic sites (% nHA) were evaluated using an ANOVA with a Tukey's multiple comparison test. Treatment groups compared over time and between anatomic site (% nHA vs. time or % nHA vs. anatomic site) were compared using a two-way ANOVA with Tukey's multiple comparison test. Statistical significance was set at $p<0.05$.

## 6.4 Results

*nHA-PTKUR scaffold characterization.* To maintain handling and mechanical properties of the material[15] for *in vivo* applications, we varied the concentration of nHA in the prepolymer between 0-45% nHA. 3D nHA-PTKUR scaffolds mimicked porous trabecular bone (**Figure 6.2A**), and SEM images displayed porosity throughout the scaffold (**Figure 6.2B)**. The moduli (5-16 MPa) and yield strength (0.23- 0.5MPa) of the nHA-PTKUR scaffolds increased in a nHA dose-dependent manner. The groups containing nHA displayed a higher ultimate strength and yield strength compared with PTKUR. No significant differences in yield strain were observed among groups (**Figure 6.2C**).

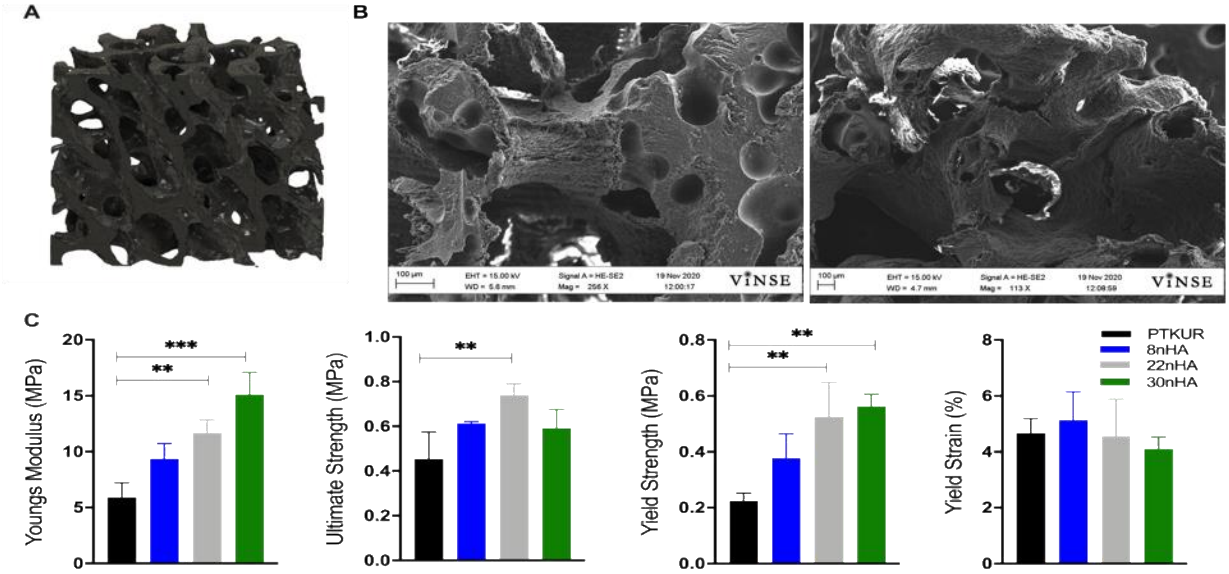


**Figure 6.2.** Porous structure and mechanical properties of 3D nHA-PTKUR scaffolds. (A) Representative .stl image of a 3D nHA-PTKUR scaffold. (B) Representative SEM images of the nHA-PTKUR scaffold internal porous structure. (C) Material properties of nHA-PTKUR porous scaffolds measured under compressive loading. Statistical significance of material properties dependent on nHA evaluated using One-way ANOVA, **p<0.01.

*nHA does not promote bone formation in a dose dependent manner in rat diaphyseal defects.* In an initial pilot study varying the wt% of nHA in a diaphyseal model, no difference was seen in the amount of new bone between groups at 4 weeks. At 8 weeks, the largest amount of new bone formation was observed in the PTKUR and 22nHA groups (**Figure 6.3A**). Increased

cartilage was seen in PTKUR samples at 4 weeks compared with the nHA treatment groups. By 8 weeks, cartilage in the PTKUR treatment decreased as the amount of new bone in the PTKUR group increased (**Figure 6.3A**). To conserve the number of animals used, all subsequent studies and analysis evaluated only PTKUR and 22nHA groups.

At 4 weeks, 3D µCT reconstructions revealed no significant differences in BV/TV between groups. At 8 weeks, the PTKUR group exhibited greater new bone formation compared with the 22nHA group although the difference was not significant. Both groups showed greater new bone formation compared with the groups at 4 weeks. A significant increase in trabecular thickening was observed in the PTKUR and 22nHA groups at 8 weeks compared with groups at 4 weeks. No significant differences in trabecular spacing or trabecular number were observed (**Figure 6.3B)**

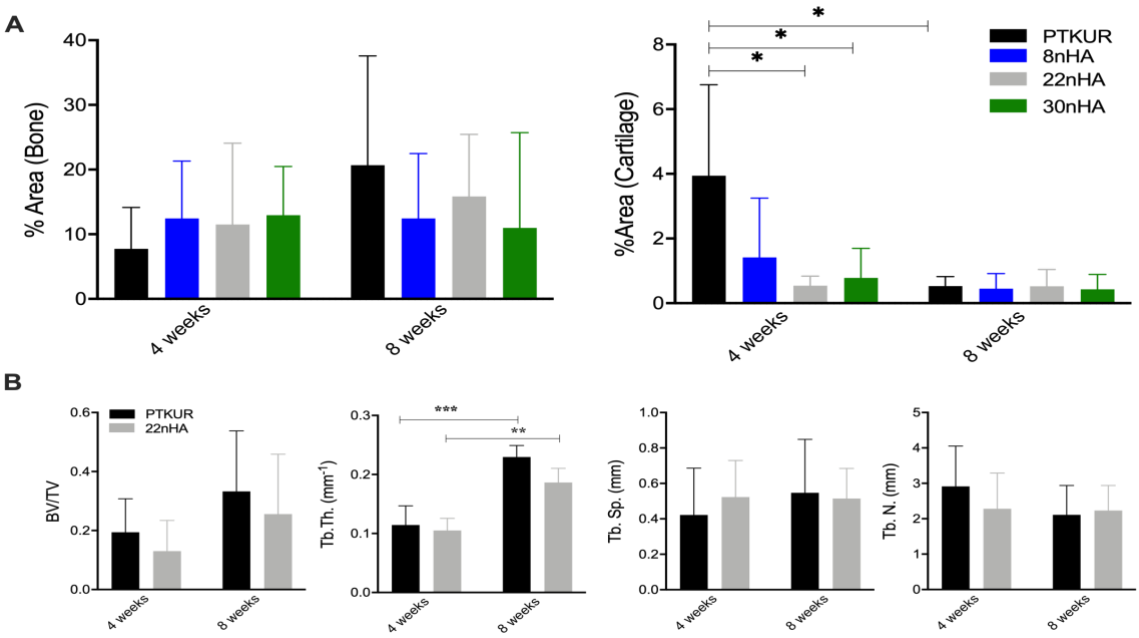


**Figure 6.3.** New bone formation analysis of nHA-PTKUR pilot study. Histomorphometric analysis of (A) area % bone and area % cartilage at 4 and 8 weeks. (B) Bone morphometric parameters (Bone volume/ total volume (BV/TV), trabecular thickening (Tb.Th.), trabecular spacing (Tb.Sp.) and trabecular number (Tb.N.)) from µCT analysis of new bone formation in rat diaphyseal model after 4 and 8 weeks. Statistical significance of histomorphometric outcomes and bone morphometric parameters at respective time points tested using Two-way ANOVA, *p<0.05, **p<0.01, ***p<0.001.

*The effects of nHA on new bone formation in vivo differ in diaphyseal and metaphyseal models.* No difference was seen in the amount of new bone between PTKUR and 22nHA at 4 weeks in the diaphyseal model (**Figure 6.4A**). However, an increase in new bone was seen in PTKUR at 8 weeks compared with 22nHA (**Figure 6.4B**). PTKUR at 4 weeks showed a significant increase in cartilage formation within the scaffold compared with 22nHA at 4 weeks. As bone increased over time within PTKUR scaffolds, the area% cartilage significantly decreased from 4 weeks to 8 weeks (**Figure 6.4C**). Histological evidence of a large cartilage callus ossifying into bone was present in PTKUR samples (**Figure 6.5A-C**), while only small amounts of cartilage ossifying into bone were observed in 22nHA (**Figure 6.5D-F**).

In contrast with the diaphyseal model, histomorphometry of von Kossa stained PTKUR scaffolds in the metaphyseal model showed significantly less new bone compared with 22nHA scaffolds at both 4 and 8 weeks (**Figure 6.4D-E**). Minimal (<1.0%) cartilage was seen in the metaphyseal model in both groups, and no significant difference in the amount of cartilage between PTKUR and 22nHA in the metaphyseal model was observed (**Figure 6.4F**).

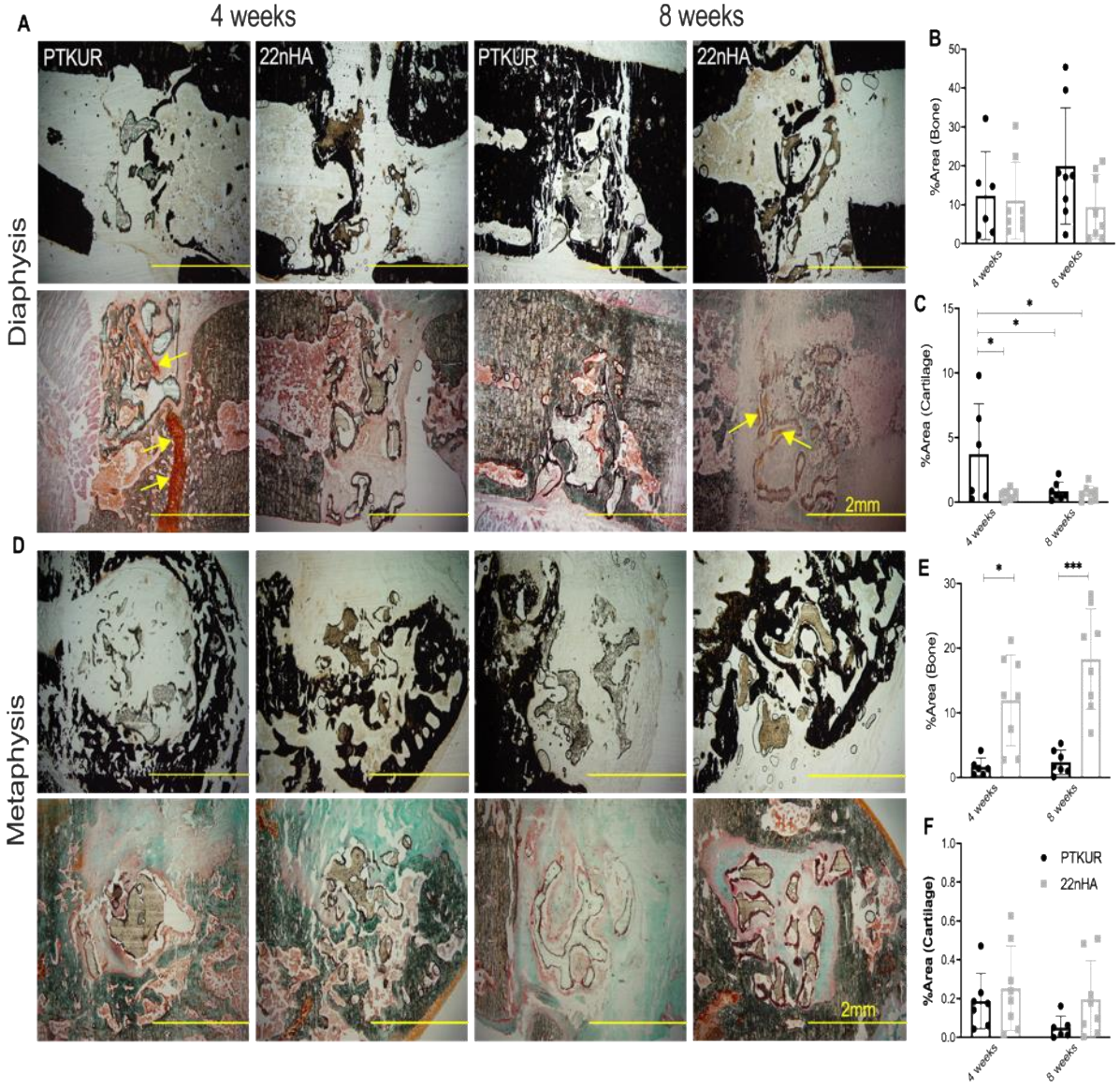


**Figure 6.4.** Histomorphometric analysis of new bone and cartilage formation in nHA-PTKUR scaffolds in rat diaphyseal and metaphyseal models. (A) Representative images of diaphyseal von Kossa and Safranin O - stained sections (4X). Histomorphometric analysis of (B) area % bone and (C) area % cartilage in nHA-PTKUR scaffolds at 4 and 8 weeks within the diaphysis. (D) Representative images of metaphyseal von Kossa- and Safranin O-stained sections (4X). Histomorphometric analysis of (E) area % bone and (F) area % cartilage in nHA-PTKUR scaffolds at 4 and 8 weeks within the metaphysis. Statistical significance determined using Two-way ANOVA, *$p<0.05$, ***$p<0.001$.

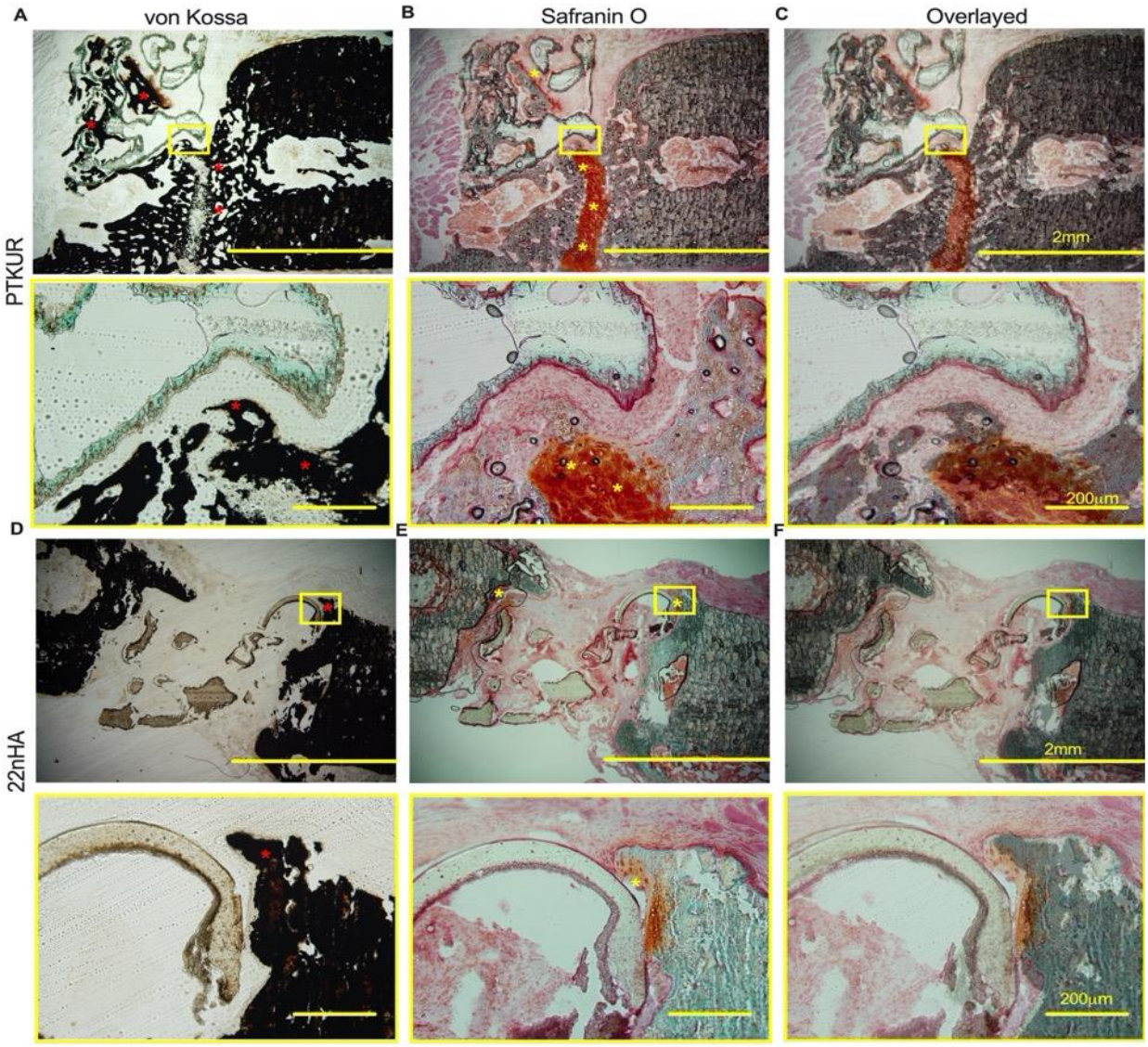


**Figure 6.5.** High magnification histology of new bone and cartilage formation in nHA-PTKUR scaffolds within the diaphyseal model. Representative von Kossa images (Top row, 4X and bottom row, 20X) depicting new bone formation in (A) PTKUR scaffolds where new bone (red stars) is seen throughout the middle of the defect and into the scaffold and (D) 35nHA where new bone is only seen on the periphery of the defect. Representative Safranin O (Top row, 4X and bottom row, 20X) images depicting cartilage (orange) in (B) PTKUR scaffolds where cartilage is seen infiltrating and ossifying into bone within the defect and scaffold and (E) 35nHA scaffolds where only small amounts of cartilage are seen at the periphery of the defect. (C, F) Superimposed von Kossa and Safranin O images depict where cartilage is actively ossifying into bone.

*Infiltrating cell populations within nHA-PTKUR scaffolds do not differ significantly between anatomic sites.* To assess the whether the population of host cells within the scaffolds contributed to the observed differences in bone formation at different anatomic sites, IHC was

performed for CD146, Endomucin (Emcn), and CD31 (**Figure 6.6A**). No significant differences in $CD146^+$ staining, a marker that differentiates between marrow-derived multipotent stromal cells and terminally differentiated cells [24], were observed between groups or anatomic sites at both 4 weeks and 8 weeks (**Figure 6.6B**). $Emcn^+$ cells were present within both anatomic sites, and no differences were seen between groups or anatomic sites at 4 and 8 weeks (**Figure 6.6C**). Some $CD31^+$ staining was observed in the diaphysis, but no significant differences between groups were seen. However, in the metaphysis significantly more $CD31^+$ staining was observed in 22nHA compared with PTKUR (**Figure 6.6D**). $CD31^+$ staining was observed predominantly around the perimeter of the scaffolds and of bone (**Figure 6.6A**). The spatial distribution of $CD31^+$ staining throughout the defect appeared to be co-localized with new bone (**Figure 6.6E**).

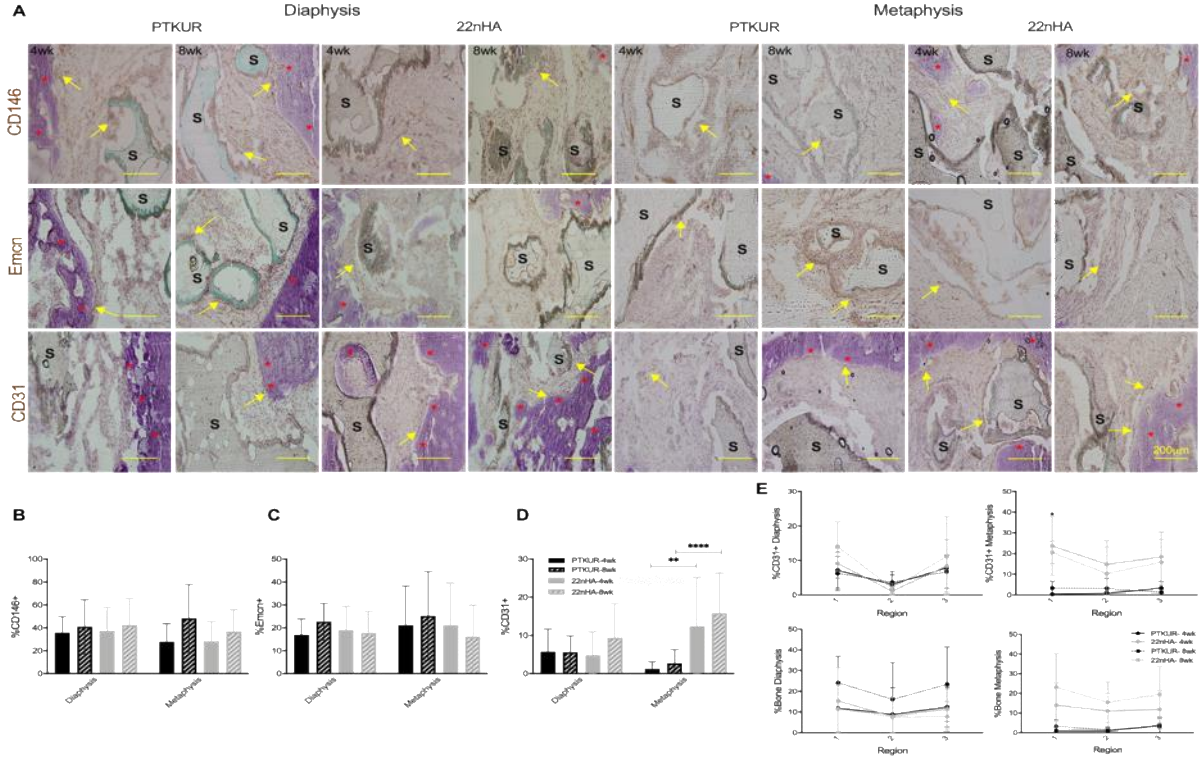


**Figure 6.6.** Infiltrating cell populations in nHA-PTKUR scaffolds at 4 and 8 weeks. (A) Representative diaphyseal and metaphyseal sections stained with CD146, Endomucin, and CD31 at 4 and 8 weeks (20X). Yellow arrows indicate positive staining, S indicates scaffold, red asterisks indicate bone. Quantification of (B) CD146+, (C) Endomucin+, and (D) CD31+ staining. (E) Spatial distribution of CD31+ staining and new bone within each defect. Statistical significance determined using Two-way ANOVA, **p<0.01, ****p<0.0001.

*PTKUR degradation in vivo.* For a better understanding of macrophage-medicated degradation of PTKUR *in vivo*, IHC for myeloperoxidase (MPO) and CD68 was performed. Histological sections showed visible differences in MPO, a marker of ROS and oxidative stress, between treatment groups (**Figure 6.7A**). Positive MPO staining was observed around the periphery of the PTKUR scaffolds at both anatomic sites. Quantification of IHC confirmed these observations, and a significant increase in $MPO^+$ cells was seen in PTKUR groups at both 4 and 8 weeks in the diaphyseal model and at 8 weeks in the metaphyseal model (**Figure 6.7B**). No significant differences in $CD68^+$ macrophages were observed qualitatively or quantitatively (**Figure 6.7C**) between groups or anatomic sites at both 4 and 8 weeks.

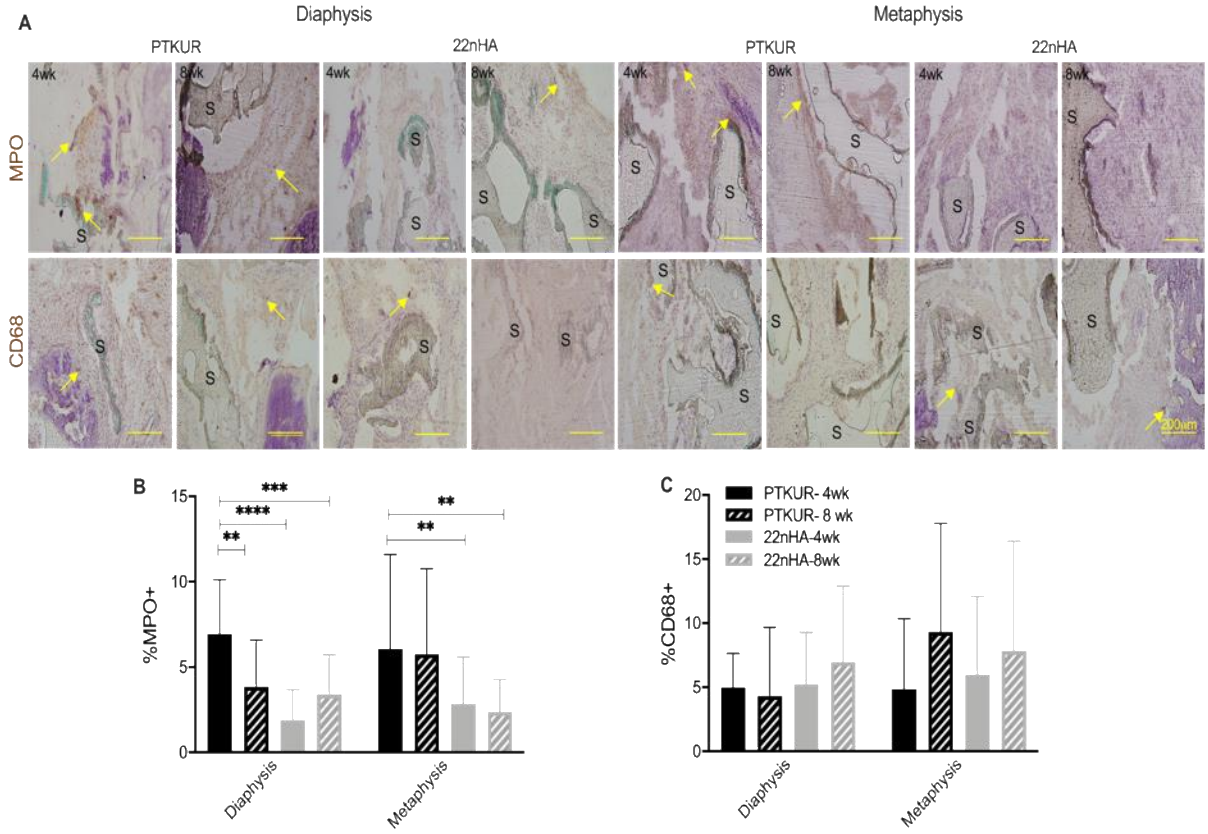


**Figure 6.7.** nHA-PTKUR degradation in vivo. (A) Representative diaphyseal and metaphyseal sections stained with Myeloperoxidase and CD68 at 4 and 8 weeks (20X). Yellow arrows indicate positive staining. S indicates scaffold. Quantification of (B) MPO+ and (C) CD68+ staining. Statistical significance determined using Two-way ANOVA, **p<0.001, ***p<0.001, ****p<0.0001.

## 6.5 Discussion

While nHA, a naturally occurring form of calcium apatite, has been widely studied as a synthetic bone graft due to its mechanical and osteogenic properties [25], its effects on ossification at specific anatomic sites have not been directly investigated. Additionally, we implanted nHA-PTKUR scaffolds in two anatomic sites in rats, the femoral diaphysis and femoral metaphysis, to gain a comprehensive understanding of nHA and its effect on ossification *in vivo*. New cartilage was observed in the absence of nHA at diaphyseal but not metaphyseal sites. In contrast, new bone formation increased with nHA loading at metaphyseal but not diaphyseal sites. Thus, nHA composite scaffolds induce osteogenic differentiation of adherent endogenous progenitor cells, which can either promote or inhibit fracture healing depending on the skeletal site.

To understand the effects of nHA loading and anatomic site on ossification *in vivo*, we implanted nHA-PTKUR scaffolds into diaphyseal and metaphyseal bone defects in rats and assessed outcomes at 4 and 8 weeks. Scaffolds were implanted in non-critical-size (2 mm) defects in order to maintain the capacity to heal.[26] Histological and immunohistochemical analysis of new bone and cartilage formation as well as infiltrating cell populations was performed using cryo-sectioning techniques. The anatomic site and nHA loading affected the mechanism by which new bone formed within the scaffolds *in vivo*. PTKUR scaffolds showed evidence of endochondral ossification through callus formation at 4 weeks followed by ongoing callus ossification at 8 weeks. New bone was seen throughout the scaffolds and the defect space. These findings are consistent with a previous study in which endochondral ossification was observed at 3 and 6 weeks in a porous collagen scaffold. [13] In contrast, the 22nHA group displayed only small amounts of cartilage undergoing ossification near the periphery of the defect. New bone formation was limited to the endosteum and periphery of the defect and did not extensively infiltrate the scaffolds. These

findings suggest that the presence of nHA in diaphyseal defects impairs endochondral ossification, which is the predominant healing mechanism at this anatomic site [27], resulting in less bone formation at 8 weeks.

In metaphyseal defects, minimal cartilage (<0.2%) was observed in either of the groups, and significantly more new bone formation was observed in 22nHA compared with PTKUR. In a previous study, low-porosity (<5%) nHA-PTKUR cements implanted in metaphyseal defects in rat femora osseointegrated by intramembranous ossification near the periphery coupled with infiltration of chondrocytes and endochondral ossification in the hypoxic interior. [15] In contrast, the nHA-PTKUR scaffolds used in this study were 80% porous [20] and endochondral ossification in the metaphysis was not observed. Consistent with our *in vitro* findings and previous studies [28], the addition of nHA within metaphyseal defects promoted intramembranous ossification by directly inducing osteoblast differentiation. Thus, the effects of nHA on the predominant mechanisms of ossification depended on the anatomic site where the scaffolds were implanted.

Vascularity at the fracture site is imperative for successful bone regeneration. [29] Previous studies have shown both CD31 and Endomucin to be markers of angiogenesis.[30,31] Bone contains specific subtypes of capillaries, Type H ($CD31^{hi}/Emcn^{hi}$) and Type L ($CD31^{lo}/Emcn^{lo}$) vessels [30], typically found in the metaphysis and diaphysis, respectively. Previous studies have established a relationship between Type H vessels and $Osterix^{+}$ cells which can differentiate into osteoblasts and osteocytes. [30,32] While significant differences in Endomucin staining were not detected between anatomic sites in the present study, increased $CD31^{+}$ staining was observed in the 22nHA group in the metaphysis. Furthermore, we observed $CD31^{+}$ staining predominantly where new bone formation was also observed via spatial analysis.

Recent studies have suggested CD146 as a marker to discriminate between bone marrow-derived multipotent stromal cells and terminally differentiated cells.[13,24,33] Furthermore, $CD146^+$ cells have the capacity to differentiate into bone-like tissue and cartilage *in vitro.* [34] No differences in $CD146^+$ cells between defect sites or treatment groups were observed. To determine if there was a difference in macrophage and inflammatory responses between groups, IHC for CD68 was performed. No differences in $CD68^+$ cells were observed between groups, indicating a normal host response to the implanted scaffolds. Together, these data demonstrate that nHA did not have an effect on the infiltrating cell populations. While the addition of growth factors such as bone morphogenetic proteins act by recruiting and inducing differentiation of endogenous MSCs at the defect site [2] , the results from this study demonstrate that the effects of embedded nHA do not display such osteoinductive behavior and are limited to cellular interactions with the surface of the scaffold.

At 8 weeks, residual scaffold remained in the defect sites. PTKUR breaks down rapidly in response to ROS secreted by macrophages and other adherent inflammatory cells [17,35], while nHA degrades slowly by osteoclast-mediated resorption *in vivo.* [36] Slow degradation of low-porosity nHA-PTKUR cements was observed in a previous study. [15] In the present study, the interconnected pores of the scaffolds allowed for increased cellular infiltration. PTKUR in both anatomic sites displayed enhanced $MPO^+$ staining compared with the minimal $MPO^+$ staining observed in the 22nHA material. A previous study in a porcine model showed enhanced macrophage activity localized at scaffold/tissue interface in PTKUR scaffolds [35]. The reduced $MPO^+$ staining observed in 22nHA suggests that the presence of nHA results in fewer adherent macrophages on the surface of the scaffold, and thus nHA-PTKUR scaffolds degrade at a slower rate compared with PTKUR.

## 6.6 Conclusion

nHA-PTKUR scaffolds implanted in rats promoted both intramembranous and endochondral ossification dependent on material formulation and anatomic sites, indicating the importance of these factors as key regulators in assessing overall outcomes and efficacy of novel biomaterials for bone regeneration. Moving forward, more tailored approaches for bone regeneration based on natural healing response for specific anatomic sites and applications must be adopted.

References


1. Percival, C. J. & Richtsmeier, J. T. Angiogenesis and intramembranous osteogenesis. *Developmental Dynamics* (2013). doi:10.1002/dvdy.23992
2. Wang, W. & Yeung, K. W. K. Bone grafts and biomaterials substitutes for bone defect repair: A review. *Bioactive Materials* (2017). doi:10.1016/j.bioactmat.2017.05.007
3. Baker, C. E. *et al.* Bone Fracture Acute Phase Response—A Unifying Theory of Fracture Repair: Clinical and Scientific Implications. *Clin. Rev. Bone Miner. Metab.* **16**, 142–158 (2018).
4. Marsell, R. & Einhorn, T. A. The biology of fracture healing. *Injury* (2011). doi:10.1016/j.injury.2011.03.031
5. Kronenberg, H. M. Developmental regulation of the growth plate. *Nature* (2003). doi:10.1038/nature01657
6. Yang, L., Tsang, K. Y., Tang, H. C., Chan, D. & Cheah, K. S. E. Hypertrophic chondrocytes can become osteoblasts and osteocytes in endochondral bone formation. *Proc. Natl. Acad. Sci. U. S. A.* (2014). doi:10.1073/pnas.1302703111
7. Einhorn, T. A. & Gerstenfeld, L. C. Fracture healing: Mechanisms and interventions. *Nature Reviews Rheumatology* (2015). doi:10.1038/nrrheum.2014.164
8. Kolk, A. *et al.* Current trends and future perspectives of bone substitute materials - From space holders to innovative biomaterials. *Journal of Cranio-Maxillofacial Surgery* (2012). doi:10.1016/j.jcms.2012.01.002
9. Sheehy, E. J., Kelly, D. J. & O'Brien, F. J. Biomaterial-based endochondral bone regeneration: a shift from traditional tissue engineering paradigms to developmentally inspired strategies. *Materials Today Bio* (2019). doi:10.1016/j.mtbio.2019.100009
10. Harada, N. *et al.* Bone regeneration in a massive rat femur defect through endochondral ossification achieved with chondrogenically differentiated MSCs in a degradable scaffold. *Biomaterials* (2014). doi:10.1016/j.biomaterials.2014.05.052
11. Matsiko, A. *et al.* An endochondral ossification approach to early stage bone repair: Use of tissue-engineered hypertrophic cartilage constructs as primordial templates for weight-bearing bone repair. *J. Tissue Eng. Regen. Med.* (2018). doi:10.1002/term.2638
12. McDermott, A. M. *et al.* Recapitulating bone development through engineered mesenchymal condensations and mechanical cues for tissue regeneration. *Sci. Transl. Med.* (2019). doi:10.1126/scitranslmed.aav7756
13. Petersen, A. *et al.* A biomaterial with a channel-like pore architecture induces endochondral healing of bone defects. *Nat. Commun.* **9**, 4430 (2018).
14. McGough, M. A. *et al.* Poly (Thioketal Urethane) Autograft Extenders in an Intertransverse Process Model of Bone Formation. *Tissue Eng. Part A* (2019).
15. McGough, M. A. P. *et al.* Nanocrystalline Hydroxyapatite-Poly(thioketal urethane) Nanocomposites Stimulate a Combined Intramembranous and Endochondral Ossification Response in Rabbits. *ACS Biomater. Sci. Eng.* **6**, 564–574 (2020).
16. McEnery, M. A. P. *et al.* Oxidatively degradable poly(thioketal urethane)/ceramic composite bone cements with bone-like strength. *RSC Adv.* **6**, 109414–109424 (2016).
17. Martin, J. R. *et al.* A porous tissue engineering scaffold selectively degraded by cell-generated reactive oxygen species. *Biomaterials* (2014). doi:10.1016/j.biomaterials.2014.01.026
18. Panaroni, C. *et al.* PTH Signaling in Osteoprogenitors Is Essential for B-Lymphocyte

Differentiation and Mobilization. *J. Bone Miner. Res.* (2015). doi:10.1002/jbmr.2581
19. Dyment, N. A. *et al.* High-throughput, multi-image cryohistology of mineralized tissues. *J. Vis. Exp.* (2016). doi:10.3791/54468
20. Vanderburgh, J. P., Fernando, S. J., Merkel, A. R., Sterling, J. A. & Guelcher, S. A. Fabrication of Trabecular Bone-Templated Tissue-Engineered Constructs by 3D Inkjet Printing. *Adv. Healthc. Mater.* **6**, (2017).
21. Hafeman, A. E. *et al.* Characterization of the degradation mechanisms of lysine-derived aliphatic poly(ester urethane) scaffolds. *Biomaterials* **32**, 419–429 (2011).
22. Guelcher, S. A. *et al.* Synthesis, mechanical properties, biocompatibility, and biodegradation of polyurethane networks from lysine polyisocyanates. *Biomaterials* (2008). doi:10.1016/j.biomaterials.2007.12.046
23. Brown, K. V *et al.* Improving bone formation in a rat femur segmental defect by controlling bone morphogenetic protein-2 release. *Tissue Eng. Part A* **17**, 1735–46 (2011).
24. Sacchetti, B. *et al.* Self-Renewing Osteoprogenitors in Bone Marrow Sinusoids Can Organize a Hematopoietic Microenvironment. *Cell* (2007). doi:10.1016/j.cell.2007.08.025
25. Venkatesan, J. & Kim, S. K. Nano-hydroxyapatite composite biomaterials for bone tissue engineering - A review. *Journal of Biomedical Nanotechnology* (2014). doi:10.1166/jbn.2014.1893
26. Seta, J. Healing of bone fracture: general concepts. in *Principles of Bone Regeneration* (eds. Seta, J. & Bab, I.) 1–8 (Springer Science & Business Media, 2012).
27. Inoue, S., Otsuka, H., Takito, J. & Nakamura, M. Decisive differences in the bone repair processes of the metaphysis and diaphysis in young mice. *Bone Reports* (2018). doi:10.1016/j.bonr.2017.11.003
28. Sandberg, O. H. & Aspenberg, P. Inter-trabecular bone formation: a specific mechanism for healing of cancellous bone: A narrative review. *Acta Orthop.* (2016). doi:10.1080/17453674.2016.1205172
29. Keramaris, N. C., Calori, G. M., Nikolaou, V. S., Schemitsch, E. H. & Giannoudis, P. V. Fracture vascularity and bone healing: A systematic review of the role of VEGF. *Injury* (2008). doi:10.1016/S0020-1383(08)70015-9
30. Kusumbe, A. P., Ramasamy, S. K. & Adams, R. H. Coupling of angiogenesis and osteogenesis by a specific vessel subtype in bone. *Nature* (2014). doi:10.1038/nature13145
31. Kenswil, K. J. G. *et al.* Characterization of Endothelial Cells Associated with Hematopoietic Niche Formation in Humans Identifies IL-33 As an Anabolic Factor. *Cell Rep.* (2018). doi:10.1016/j.celrep.2017.12.070
32. Nakashima, K. *et al.* The novel zinc finger-containing transcription factor Osterix is required for osteoblast differentiation and bone formation. *Cell* (2002). doi:10.1016/S0092-8674(01)00622-5
33. Harkness, L., Zaher, W., Ditzel, N., Isa, A. & Kassem, M. CD146/MCAM defines functionality of human bone marrow stromal stem cell populations. *Stem Cell Res. Ther.* (2016). doi:10.1186/s13287-015-0266-z
34. Serafini, M. *et al.* Establishment of bone marrow and hematopoietic niches in vivo by reversion of chondrocyte differentiation of human bone marrow stromal cells. *Stem Cell Res.* (2014). doi:10.1016/j.scr.2014.01.006
35. Patil, P. *et al.* Porcine Ischemic Wound-Healing Model for Preclinical Testing of Degradable Biomaterials. *Tissue Eng. Part C Methods* (2017).

doi:10.1089/ten.tec.2017.0202
36. Wenisch, S. *et al.* In vivo mechanisms of hydroxyapatite ceramic degradation by osteoclasts: Fine structural microscopy. *J. Biomed. Mater. Res. - Part A* (2003). doi:10.1002/jbm.a.10091

# CHAPTER VII

## CHAPTER 7: SUMMARY AND CONCLUSIONS

In this work, osteoinductive polyurethane composites were evaluated *in vitro* and *in vivo* to evaluate the mechanisms of bone formation and remodeling. The work described in this dissertation was motivated by the findings in Chapter 3 in which compression-resistant poly (ester urethane) (PEUR) carriers for recombinant human bone morphogenetic protein- 2 (rhBMP-2) were found to promote new bone formation in a dose-responsive manner in a clinically relevant non-human primate model. However, the costs associated of gaining FDA approval for a new carrier for a biologic growth factor demonstrated the need to develop osteoinductive bone substitutes without the use of rhBMP-2. Previous success in the lab utilizing autograft (AG) and the lack of FDA approval needed for its use prompted further investigation of AG extenders. We sought to determine the optimal AG extender composition to promote enhanced bone formation and graft remodeling *in vivo*. Although poly (thioketal urethane) (PTKUR) composites were slower to degrade than PEUR composites, comparable bone formation was observed with both polymers. However, reduced osteoinductivity of polymer-embedded AG was observed thus prompting the transition to an alternative osteoinductive component. Nanocrystalline hydroxyapatite (nHA) was selected due to its ability to be homogenously dispersed within polymer and extensive research demonstrating its osteoinductivity. The results from our *in vitro* studies demonstrated that polymer dispersed nHA promotes mineralization and subsequent osteoblast differentiation in a dose-dependent manner through phosphate transporter-1 (PiT1) and Erk1/2 signaling. *In vivo* results showed that nHA-PTKUR scaffolds promote both intramembranous and endochondral ossification dependent on material formulation and anatomic sites. The results of these studies detailed herein demonstrate how material formulation can alter cellular behavior, subsequent

osteogenesis, and remodeling. Moving forward, more tailored approaches for bone regeneration based on natural healing response for specific skeletal sites and applications must be adopted.

AG is the gold standard of bone grafting but is limited in its availability, thus, AG extenders have been developed to increase the overall volume of AG while maintaining its osteogenic and osteoinductive properties. Previous work in the lab utilizing AG demonstrated new bone formation but demonstrated slow polymer degradation. These findings led to the hypothesis that PEUR composites would degrade at a rate more ideal for the formation of new bone. Thus, in Chapter 4, AG was mixed with PTKUR or PEUR to determine the optimal AG composition to enhance bone and graft remodeling *in vivo*. PTKUR- and PEUR-AG extenders were developed and implanted in a rabbit radius model. In this model, both PTKUR- and PEUR- AG extenders maintained AG within the defect throughout the study. Histomorphometry demonstrated that both AG extenders degraded, however, PEUR-AG extenders degraded more rapidly when compared to PTKUR-AG extenders. The differences in degradation did not have an effect on overall bone formation between the AG extenders. However, compared with AG control, polymer embedded AG within the extenders demonstrated reduced osteoinductivity. These results highlighted the need for more porous scaffolds that allowed for earlier cellular infiltration and the need for utilization of a surface bound osteoinductive component that would not remain encapsulated in polymer.

nHA is osteoinductive and has been extensively utilized in composite bone substitutes, however, the mechanism by which polymer-bound nHA promotes osteogenesis *in vitro* and *in vivo* was poorly understood. In Chapter 5, polymer-bound nHA was evaluated *in vitro*. Human mesenchymal stem cells (hMSCs) were seeded on nHA composite substrates. Matrix staining demonstrated that nHA promoted osteogenic differentiation of hMSCs in a nHA dose-dependent manner. Immunofluorescent staining demonstrated that nHA played a role in both phosphate

transporter 1 (PiT1/SLC20a1) and fibroblast growth factor 2 (FGFR2) signaling. Western blot analysis further confirmed that nHA dispersed in polymeric composites induced osteoblast differentiation and mineralization through Erk1/2 signaling at low loadings. Furthermore, we determined through FRET analysis that PiT1 and FGFR2 do not colocalize suggesting that they are not located in the same subcellular structures and are not simultaneously activated by nHA. These findings underscored the ability of nHA to lead to direct differentiation of hMSCs into osteoblasts.

Given the mechanism by which polymer bound-nHA promoted osteogenesis *in vitro*, 3D nHA- PTKUR scaffolds were implanted in the femoral diaphysis and femoral metaphysis in rats to evaluate the effect of nHA on osteogenesis and the mechanism of bone formation *in vivo* in Chapter 6. Methods previously developed in our lab were utilized to synthesize a nHA-PTKUR 3D tissue engineered composite. Histomorphometric analysis revealed that the presence of nHA in diaphyseal defects impaired endochondral ossification, resulting in less overall bone formation while the addition of nHA within metaphyseal defects promoted intramembranous ossification by directly inducing osteoblast differentiation. Thus, the effects of nHA on the predominant mechanisms of ossification was dependent on the anatomic site where the scaffolds were implanted. Immunohistochemistry (IHC) further demonstrated that nHA did not have an effect on the infiltrating cell populations and that its effects were limited to cellular interactions with the surface of the scaffold. Additionally, IHC revealed that the addition of nHA to PTKUR scaffolds led to slower degradation *in vivo*. These results further highlighted the need to develop tailored materials for bone regeneration that are based on the natural healing response for specific anatomic sites.

# CHAPTER VII

This work demonstrates a better understanding of how osteoinductive composites promote bone formation and how these effects can change based upon skeletal site. Furthermore, anatomic site must not be the only consideration; application must also be considered. For weight bearing applications, slowly degrading PKTKUR may be advantageous while PEUR may be better for rapidly degrading bone void fillers. Collectively, this work suggests that a universal bone substitute is not the solution, but rather materials must consider the anatomic site and application for which they are intended for in the substitute or graft development process.

CHAPTER VIII

# CHAPTER 8: FUTURE DIRECTIONS

Future work will build off of the conclusions found from this work. This chapter will focus on future directions to optimize osteoinductive grafts for bone remodeling to better suit specific skeletal sites and applications.

## 8.1 AG Extenders

In chapter 4, PTKUR-AG and PEUR-AG extenders maintained AG within the defect site. Both AG extenders promoted bone formation, however, bone formation was most evident at the host bone/graft interface rather than within the defect.

Implanted AG-extenders were not highly porous and residual polymer was observed in the defect at 12 weeks. Minimal initial porosity likely inhibited early cellular infiltration, thus less new bone and AG resorption was seen within the AG extenders *in vivo* while the AG control demonstrated full resorption and increased bone formation. Taken together, this suggests that porosity inhibited initial cellular infiltration while AG remained embedded within residual polymer. Although AG within the extenders maintained some level of osteoinductivity, it was reduced with that of the AG control. Future studies will determine the optimal porosity of AG extenders to promote early osteoinductive effects. Increased initial porosity in an rhBMP-2 carrier allowed for ample bone formation via direct osteogenic differentiation of infiltrating cells[1], thus it is anticipated that increasing porosity in AG extenders would allow for early cellular infiltration and osteoinductive factors released from the AG would better promote osteogenic differentiation. However, the rate of porosity will need to be balanced such that graft resorption does not occur too quickly. Additionally, AG volume must be optimized to both maintain porosity and promote enhanced bone formation.

Decreased cellular infiltration was observed within the PTKUR-AG extenders. Despite the

use of a hydrophilic lysine-triisocyanate poly (ethylene glycol) (LTI-PEG) prepolymer in the formulation of PTKUR-AG extenders, poly (thioketal) (PTK) is inherently hydrophobic.[2] Therefore, we hypothesize that using a more hydrophilic PTK to formulate the PTKUR-AG extender may lead to increased graft remodeling and cellular infiltration. Thus, future work will focus on the formulation of more hydrophilic PTKUR-AG extenders. Lead candidates will then be tested *in vivo* although, cellular activity varies by animal and model.[3–5]

## 8.2 nHA composites *in vitro*

As demonstrated in Chapter 5, nanocrystalline hydroxyapatite (nHA) dispersed in polymeric composites promoted osteogenesis via PiT1 and downstream Erk1/2 signaling and did not have an effect on chondrogenesis. However, fractures typically heal through a combination of both intramembranous ossification and endochondral ossification.[6,7] Therefore, future work will aim to incorporate polyphosphate nanoparticles to promote cartilage formation. Polyphosphates are biopolymers composed of phosphate groups ($n$=10-300 Pi units) linked by phosphoanhydride bonds.[8] Polyphosphate nanoparticles (nPPi, 50-100 nm)degrade via enzymatic hydrolysis in the presence of alkaline phosphatase (ALP) [8–10] and the bioactivity of nPPi depends on the cation used for salt formation.[8,11] Mesenchymal stem cells (MSCs) cultured on Ca-nPPi and Mg-nPPi expressed both osteogenic and chondrogenic markers,[11–15] thus we hypothesize that structural nPPi- PTKUR grafts will potentially increase osseointegration by inducing chondrogenic differentiation of endogenous MSCs and subsequent endochondral ossification.

Preliminary studies in which human MSCs (hMSCs) were cultured on fabricated Ca-nPPi-PTKUR composites were performed. Minimal Alizarin red staining, a marker of mineralization, was observed on nPPi-PTKUR until day 21 (**Figure 8.1A**) while Ca-nPPi induced chondrocyte differentiation in the early timepoints (**Figure 8.1B**). These data suggest bone formation through

a chondrogenic pathway occurs in hMSCs seeded on nPPi composites. Furthermore, no positive phosphate transporter-1 (PiT1) staining was observed in hMSCs cultured on nPPi-PTKUR. Thus, while nHA induces osteoblast differentiation through PiT1, Ca-nPPi does not, instead potentially proceeding through a cartilage intermediate.

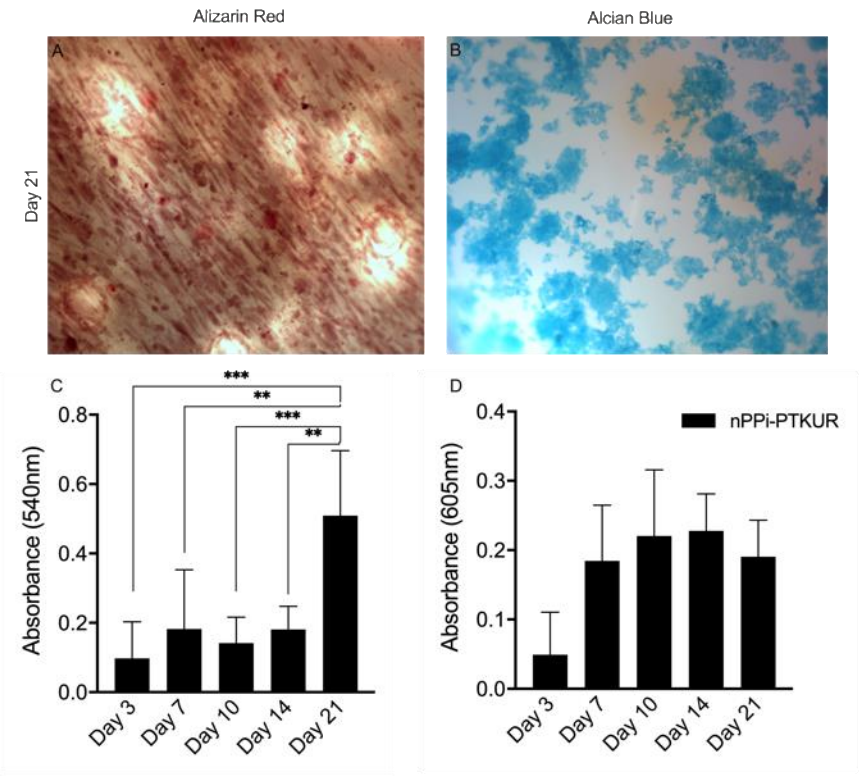


**Figure 8.1.** Differentiation of hMSCs cultured on nPPi- PTKUR polymers. Representative images of (A) Alizarin red-and (B) Alcian blue stained cells cultured on nPPi-PTKUR at day 21. Quantification of (C) Alizarin red and (D) Alcian Blue staining on nPPi composites. Statistical significance determined via one-way ANOVA ** $p<0.01$; *** $p<0.001$.

Future *in vitro* work will aim to confirm the chondrogenic potential of nPPi-PTKUR hybrid polymers using a Dimethyl methylene Blue (DMMB) assay and to identify membrane receptors that mediate intracellular signal transduction important in chondrocyte differentiation in response to nPPi utilizing a cell surface biotinylation assay. Additionally, optimal nPPi concentrations will be determined.

Furthermore, nHA-nPPi hybrid composites have the potential to lead to an osteogenic-

chondrogenic combinatorial response, thus resulting in a more anatomically representative bone substitute. Once the chondrogenic potential of nPPi-PTKUR composites is confirmed, we aim to identify the optimal nHA-nPPi formulation to elicit both an osteogenic and chondrogenic response *in vitro* utilizing von Kossa and Alizarin Red assays, DMMB analysis, and PCR.

## 8.3 nHA composites *in vivo*

In Chapter 6, the effects of nHA on the predominant mechanisms of ossification depended on the anatomic site where the scaffolds were implanted. In the metaphysis, augmentation of PTKUR scaffolds with nHA promoted an intramembranous healing response. Within the diaphysis, nHA impaired endochondral ossification. Utilizing the outcomes from the work described in section 8.1 and similar methods described in Chapter 6, we aim to investigate the effects of nPPi composites endochondral ossification *in vivo*. nPPi- and nHA-PTKUR scaffolds were successfully implanted in the muscle adjacent to the femur of skeletally mice (**Figure 8.2**). 3D μCT reconstructions (**Figure 8.2A, D**) and 2D axial (**Figure 8.2B, E**) and sagittal **(Figure 8.2C, F**) cross sections demonstrated osseointegration of Ca-nPPi-PTKUR (yellow arrows) but not nHA-PTKUR.

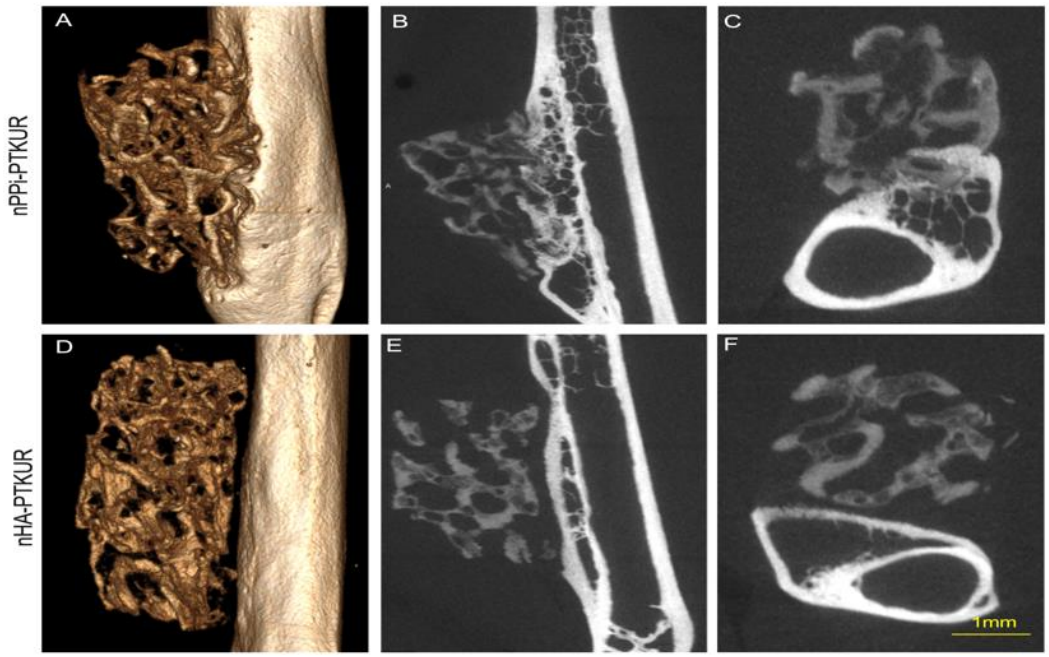


**Figure 8.2.** nPPi-PTKUR scaffolds osseointegrate in unfavorable biological environments. (A) 3D and (B-C) 2D μCT reconstructions of scaffolds implanted in femoral musculature show osseointegration of nPPi-PTKUR but not nHA-PTKUR in (D) 3D μCT reconstruction and 2D 2D (E) axial and (F) sagittal cross sections at 6 weeks. Images used with permission from Satoru 'Eggy' Egawa.

Together with the preliminary *in vitro* results, we hypothesize that nPPi-PTKUR scaffolds will facilitate endochondral ossification. Future work will evaluate nPPi-PTKUR composites in a mouse posterolateral fusion (PLF) model to confirm endochondral ossification. AcanCre$^{+/-}$/Ai9$^{fl/fl}$ mice will be used to evaluate osseointegration of the scaffolds and cartilage formation via fluorescently labeled ACAN expression. Endpoint outcomes will be assessed with μCT, histology, and immunohistochemistry.

Additionally, nHA-nPPi-PTKUR scaffolds will also be evaluated *in vivo* to determine if there is a synergistic effect between the two nanoparticles and bone formation Development of these grafts could potentially lead to solutions for cartilage-bone interface applications.

References


1. Boller, L., Jones, A., Cochran, D. & Guelcher, S. Compression-Resistant Polymer/Ceramic Composite Scaffolds Augmented with rhBMP-2 Promote New Bone Formation in a Nonhuman Primate Mandibular Ridge Augmentation Model. *Int J Oral Maxillofac Implant.* **35**, 616–624 (2020).
2. Martin, J. R. Poly(thioketal) Polymers and Their Use in the Formation of Hydrophobic and Hydrophilic Cell-Degradable Tissue Engineering Materials. (2016).
3. Muschler, G. F., Raut, V. P., Patterson, T. E., Wenke, J. C. & Hollinger, J. O. The design and use of animal models for translational research in bone tissue engineering and regenerative medicine. *Tissue Engineering - Part B: Reviews* (2010). doi:10.1089/ten.teb.2009.0658
4. Bagi, C. M., Berryman, E. & Moalli, M. R. Comparative bone anatomy of commonly used laboratory animals: Implications for drug discovery. *Comp. Med.* **61**, (2011).
5. Pearce, A. I., Richards, R. G., Milz, S., Schneider, E. & Pearce, S. G. Animal models for implant biomaterial research in bone: A review. *European Cells and Materials* **13**, (2007).
6. Einhorn, T. A. & Gerstenfeld, L. C. Fracture healing: Mechanisms and interventions. *Nature Reviews Rheumatology* (2015). doi:10.1038/nrrheum.2014.164
7. Baker, C. E. *et al.* Bone Fracture Acute Phase Response—A Unifying Theory of Fracture Repair: Clinical and Scientific Implications. *Clin. Rev. Bone Miner. Metab.* **16**, 142–158 (2018).
8. Wang, X., Schröder, H. C. & Müller, W. E. G. Amorphous polyphosphate, a smart bioinspired nano-/bio-material for bone and cartilage regeneration: Towards a new paradigm in tissue engineering. *Journal of Materials Chemistry B* **6**, (2018).
9. Wang, Y. *et al.* Progress and Applications of Polyphosphate in Bone and Cartilage Regeneration. *BioMed Research International* **2019**, (2019).
10. Müller, W. E. G. *et al.* A new polyphosphate calcium material with morphogenetic activity. *Mater. Lett.* **148**, (2015).
11. Hu, T., Xu, H., Wang, C., Qin, H. & An, Z. Magnesium enhances the chondrogenic differentiation of mesenchymal stem cells by inhibiting activated macrophage-induced inflammation. *Sci. Rep.* **8**, (2018).
12. Wang, X. *et al.* Artificial cartilage bio-matrix formed of hyaluronic acid and Mg2+-polyphosphate. *Eur. Cell. Mater.* **32**, (2016).
13. Müller, W. E. G. *et al.* A bio-imitating approach to fabricate an artificial matrix for cartilage tissue engineering using magnesium-polyphosphate and hyaluronic acid. *RSC Adv.* **6**, (2016).
14. Kandel, R. A. *et al.* Repair of osteochondral defects with biphasic cartilage-calcium polyphosphate constructs in a Sheep model. *Biomaterials* **27**, (2006).
15. Wang, X. *et al.* Amorphous polyphosphate/amorphous calcium carbonate implant material with enhanced bone healing efficacy in a critical-size defect in rats. *Biomed. Mater.* **11**, (2016).
16. Müller, W. E. G. *et al.* Amorphous, smart, and bioinspired polyphosphate nano/microparticles: A biomaterial for regeneration and repair of osteo-articular impairments in-situ. *Int. J. Mol. Sci.* **19**, (2018).

# APPENDIX

# EXPERIMENTAL PROTOCOLS

## CRYOSECTIONING BONES + BONES WITH SCAFFOLDS

**Reagents:**

- Liquid Nitrogen
- SCEM (Section Lab)

**Materials:**

- Styrofoam/Foam container (for liquid nitrogen)
- Tweezers
- Pliers (depends on sample type)
- Section Lab kit (liquid nitrogen mold and holder, wooden mallet and stand, wooden smoothing piece)
- 50mL conical tubes (1 per sample)
- Aluminum foil
- Paint brush
- Disposable blades for the Cryotome
- Sectioning Tape (Section Lab)
- Slides
- Biohazard bag

*You must be trained on the cryotome prior to cryosectioning. See Joshua Johnson for appropriate training.*

**Procedure:**

Prep samples

1. Retrieve samples from the -80C freezer.
2. If needed, remove any K-wire pins from the bones using the pliers. This will take a significant amount of time. Wire pins will need to be twisted out like a screw. You will need to do one sample at a time to prevent them from thawing out.
3. Orient samples within the appropriately sized mold and holder. Use care here to consider what plane you will want your sections in and make sure that you orient them appropriately.
4. Fill ½ of the mold with SCEM and then place your sample into the mold. Cover the remainder of your sample with SCEM and place into liquid nitrogen. Wait until the sample is completely opaque.
5. Remove the mold from liquid nitrogen and use mallet to hit the mold on the stand. This will release the frozen sample from the mold. Wrap the sample in foil, place into conical tube, and label the conical with the sample number. Place conical into -80C for long term storage.

Cutting Cryosections

1. Remove samples from the -80C (only take a few at a time to prevent the SCEM from thawing and having to re-embed your samples).
2. Place samples into cryotome to keep frozen while you prepare to cryosection.

3. Check the blade and replace with new blade if needed. If there knicks all over, you will need a new blade.
4. Remove a sample from the conical and aluminum foil. Use SCEM to mount onto frozen metal studs. Make sure to mount the sample using the flat side as this will allow better adherence. Wait for the SCEM on the stud to freeze and turn opaque.
5. Orient the stud properly within the cryotome and ensure cryotome is in its starting position. Set the section size to ~20 - 40µm.
6. Use the electronic controls to bring the blade close to, but not touching the sample. This will help to make sure you don't max out the directional capabilities of the cryotome. Use the handlebar on the side to manually move the section closer to the blade until you start shaving off the top layer of SCEM.
7. Continue to shave the SCEM using the dry paint brush to brush off any shavings until you reach the area of interest.
8. Decrease the section size to ~10µm. Cut through your sample until you are at the spot you want to obtain a section of for histology. Once there, change section size to 5µm. Cut one or two 5µm sections to make sure the sample is smooth.
9. Take your appropriately sized tape and remove the backing.
10. Place the sticky side of the tape onto the section and use wooden smoothing piece to ensure there are no bubbles.
11. Using the tweezers to hold the bottom of the tape, rotate the handlebar while simultaneously pulling up on the sample to obtain section.
12. Ensure that section is smooth and does not have any knicks and place the tape sticky side up onto a slide. Label the slide and store in slide box that is safe for -80C freezer. Once finished with sectioning, place slide box into the -80C.
13. Discard of all sample and SCEM shavings into a biohazard bag.

**Clean-up**

1. Discard of all sample and SCEM shavings into a biohazard bag.

## IHC FOR FROZEN SECTIONS

**Reagents:**

- Acetone
- PBS
- $H_2O_2$, Hydrogen Peroxide
- DAB substrate
- Goat serum (or other animal-based serum dependent on antibodies)
- Appropriate primary and secondary antibodies
- SCMM (Section Lab)
- PBS (1X)
- Hemotoxylin

**Materials:**

- Tweezers
- Slides
- Scotch tape
- Hydrophobic Pen
- Slide holders and slide containers
- Humidifying chamber

**Procedure:**

Preparation

1. Put acetone into slide container and allow to sit in the -20C until cold.
2. Get serum from the -20C, PBS, $H_2O_2$, tape, and the hydrophobic pen.
3. Take frozen sections out of the -80C freezer and let thaw.
4. Once samples are thawed and dry, tape the section tape to the slide to keep it in place during washes.

Immunostaining

1. Fix the tissues by placing slides into the slide holder and immerse into the cold acetone for 10 minutes.
2. Remove the slide holder from the acetone and allow the slides to dry at room temp.
3. Wash slides in PBS (1X) for 5 min, 2X.
4. Incubate the slides in 0.3%$H_2O_2$ solution in PBS at RT for 10 min to block endogenous peroxidase activity.
5. Wash slides in PBS (1X) for 5 min, 2X
6. With hydrophobic pen, outline the samples to minimize the amount of solution needed for the following steps.
7. Block the samples by using 10%serum in PBS for 1 hr at RT. Use enough solution to completely cover the sample within the lines of the hydrophobic pen. This will vary based on tissue size and amount.

8. During this waiting time, prepare the primary antibody solution (Primary antibody in a 0.5%serum in PBS solution) You will need to calculate how much solution you will need for each sample. This will be based off the total area within the hydrophobic pen. You want to minimize the amount of antibody needed. I typically will just use water to determine the volume needed for each sample.
9. Drain off the blocking buffer from slides.
10. Take the slides and a humidifying chamber into the cold room. Then pipette the primary antibody solution to the samples and leave in the cold room or at 4°C overnight.
11. Wash slides in PBS (1X) for 5 min, 2X.
12. Apply secondary antibody solution for 1 hr at RT in humidifying chamber (Secondary antibody in a 0.5%serum in PBS solution).
13. Wash slides in PBS(1X) for 5 min, 2X.
14. Apply DAB substrate solution (1:10 DAB: Peroxidase solution) .
15. Wash slides in PBS(1X) for 5 min, 2X.
16. Counterstain slides in Hematoxylin for 30 seconds.
17. Rinse slides in DI water.
18. Let samples dry, remove tape, and then mount to clean slides using SCMM. Use filter paper to remove any residual SCMM. Imaging will be most optimal if you take images shortly after drying.
19. Store slides in 4C for long term storage. Samples will be good for a few months but will dry out with time. Make sure to acquire ample images early on at different magnifications. Once the samples have dried out, they are no longer salvageable.

**Clean Up**

1. Dispose of liquid waste in appropriate waste containers.
2. Dispose of any tissue contaminated supplies in a biohazard waste container.

## IF FOR FROZEN SECTIONS

**Reagents:**

- Formalin
- PBS (1X)
- Permeabilization Buffer: 0.3%Triton-X 100 in PBS
- PBST: 0.05% Triton X-100 in PBS
- Blocking Buffer: 10% serum in PBST
- SCMM (Section Lab)
- Appropriate primary and secondary antibodies

**Materials and Equipment:**

- Tweezers
- Slides
- Scotch tape
- Hydrophobic Pen
- Slide holders and slide containers
- Humidifying chamber

**Procedure:**

Preparation

1. Get serum from the -20°C, tape, and the hydrophobic pen.
2. Take frozen sections out of the -80C freezer and let thaw.
3. Once samples are thawed and dry, tape the section tape to the slide to keep it in place during washes.

Immunofluorescent Staining

1. Fix the tissues by placing slides into the slide holder and immerse into formalin for 30 minutes at RT.
2. Remove the slide holder from formalin and wash slides with PBS (1X) on a shaker (use a slow and gentle speed when staining) for 5 min, 2X.
3. Permeabilize sections in 0.3%Triton X-100 in PBS for 15 minutes at RT on a shaker. **This step is only necessary if you are staining for something located inside of the cell membrane.
4. With hydrophobic pen, outline the samples to minimize the amount of solution needed for the following steps.
5. Blocks samples using Blocking Buffer for 1 hour at RT on a shaker.
6. Add primary antibodies (vortex and spin them down) at desired concentration in a 1:1 Blocking Buffer: PBST. Incubate for 1hr at RT or overnight at 4°C on a shaker.
7. Wash slides with 1% serum in PBST on a shaker for 5min, 2X.
8. Add secondary antibodies at desired concentration (1:200 typically) in 1:1 Blocking Buffer: PBST. Incubate for 1 hour at RT. Make sure to cover plate or dish with foil to minimize exposure to light.
9. Wash slides with 1% serum in PBST on a shaker for 5min, 2X.
10. Wash slides in PBS on a shaker for 5 minutes, 2X.

11. Add DAPI in PBS (1:10,000) for 10 min at RT.
12. Wash slides in PBS on a shaker for 5min, 1X to remove DAPI.
13. Let samples dry, remove tape, and then mount to clean slides using SCMM. Use filter paper to remove any residual SCMM. Imaging will be most optimal if you take images shortly after drying.
14. Store slides in 4C for long term storage. Samples will be good for a few months but will dry out with time. Make sure to acquire ample images early on at different magnifications. Once the samples have dried out, they are no longer salvageable.

**Clean Up**

3. Dispose of liquid waste in appropriate waste containers.
4. Dispose of any tissue contaminated supplies in a biohazard waste container.

## ACCESSING µCT REMOTELY USING A MAC OS

**Materials and equipment:**

- Computer with Pulse Secure, Xquartz, and Fetch Softworks
  - Xquartz is needed to open and view evaluation and local session Windows User
    - Putty will not function without XQuartz running
  - Pulse Secure (VPN) for Windows or Mac is also needed to access CT server
    - Pulse pairs with Duo Mobile on your phone (see video)
    - The secondary password is "push". This will trigger a notification on your phone for you to accept.
  - Fetch softworks program for downloading files off of the CT server
  - Terminal (this should already be on your Mac), search your applications and utilities to find it
- Good Wi-Fi or an ethernet cable connected to your router

**Procedure**

Setting Up

1. Open Xquartz.
   - It will appear in your taskbar, but a window will not open up
2. Open Terminal.
   - Write in/ copy & paste: ssh -oKexAlgorithms=+diffie-hellman-group1-sha1 -oHostKeyAlgorithms=+ssh-dss microct50@10.140.12.232 -Y
   - Ensure proper spacing or else you will get an error
3. When it prompts for "password:", input "made1in2ch".
   - The text will not appear in the window when you type, but the software will register it

Evaluating bone morphometric properties

1. Type "vue" into Terminal.
2. Type "uct_evaluation" into Terminal.
3. Find your sample's .ISQ file (raw scan data) by typing the sample name or number in the filter field. Click on the .ISQ and press OK.
   - If the sample folder/directory isn't listed, the scan has likely been backed up on tape.
4. Contour the sample using the drawing tool
   - Counterclockwise to include the region enclosed within the drawn shape
   - Contour slices at various intervals within your region of interest to better utilize built-in segmentation tools (e.g. iterate forward, etc.)
5. Select the Contour (C…) tab to morph, iterate forward, etc.
6. Select the Threshold (T…) tab to apply thresholds and execute the evaluation script
   - The BV/Density only Bone Eval. script (Script 6) will provide BV, TV, and BV/TV. The Bone Trab. Morphometry script (Script 5) will provide everything.
   - Click on the "Default VOI" button to make sure the white box encompasses all of the green contours

- Select a lower threshold used previously (e.g. the entire trabecular bone region is visible) and toggle between Preview and Grayscale to confirm

Evaluating 2D Histogram

1. Follow steps 1-4 above
2. Click on 'tasks' and then on '2D evaluation'
3. Make sure the ROI is correct and includes all of the slices you have contoured.
4. Set Gauss sigma to 0.5, Gauss support to 1, and threshold to appropriate value
5. Set No. of result sheet copies to 0 and then click on 'print list'. Then click on 'Start Evaluation'.

Viewing files in 3D Viewer (to view .ISQ or .AIM files)

1. Input "uct_3d" into DECterm
2. Click on your file name to open your file. You can slide the options to orient about certain planes or points in your file.
    - To create a 2D cut-planes in 3D Viewer, use the 'Subdim' menu

Downloading Evaluation Data:

1. Log onto Fetch Softworks
    - The 'hostname' is 10.140.12.232 or 10.140.12.228, the 'username' is microCT (for uct40) or microCT50 (for uct50), and the password "made1in2ch".
    - You will need to click on the arrow showing additional information to get into the right folder where the actual data is stored. In the
        1. DK0:[MICROCT50.DATA]
        2. Or DISK1:[MICROCT50.RESULTS.2D]
2. Click on the file and click on the title of the file name to save it directly to your computer.
    - If the title is a .dat file then save it as a .txt file so your MAC can read it

## IMAGING WHOLE SLIDES WITH CYTATION

**Materials:**

- Slides with samples ready to be imaged
- External Hard Drive with ample storage space
- Biotek Cytation (located in the VA or Jim Cassat's lab)

**Procedure:**

Preparation

1. Turn on the Cytation if it is off.
2. Once running, press the circular button on the side to eject the slide holder.
3. Place slides (sample facing down) into the slide holder. Make sure they click into place and lay completely flat before proceeding.
4. Place the slide holder into the slot and press the circular button.
5. Open Gen5 305 Imager software. A pop up will ask you to confirm vessel type. Click on BioTek:4 slide holder and press 'OK'.

Imaging

1. In the top left corner, specify the magnification you would like to use and specify if you will be imaging a fluorescently stained slide (choose appropriate wavelength) or a bright field slide.
2. Select the appropriate well (A1 = slide 1, A2 = slide 2, etc.).
3. Use the coarse and fine focus to bring the slide into focus. Once the slide is mostly in focus, you can use the 'Autofocus' button to obtain the best focus.
4. Edit the Exposure features if necessary.
5. Click on 'Imaging Mode' and click on 'Montage'. Then set your boundaries for the region of your slide you would like to image. The larger the area, the longer it will take to image. Use the directional arrows located underneath the 'Histogram' to move your slide and find your boundaries. Once you are at the right spot, click on either 'Set Top', 'Set left', etc.
6. After setting boundaries, click on 'Edit Imaging Step'. This page will show you the number of images that will be acquired in terms of rows and columns. Click on the 'options' button and switch from 'Autofocus' to 'Fixed focal height'. Press 'OK'.
7. Once your settings are correct, click on the camera icon in the bottom left corner.
8. The software will now acquire images for you. Once it is finished, click on 'Image stitching'.
9. The 'Downsize stitched image' will automatically be turned on. Click on it to turn it off. If you are taking a bright field image, you will need to specify the Registration Channel. Use either Red, Green, or Blue depending on which colors are most present in your image. If H&E staining, it will likely be best to use Red. Click 'OK' and the software will stitch your image. Click 'YES' when it asks if you are okay with a large file size.
10. Once the image is stitched, click on 'Save Image'. Then click 'Save Picture for Presentation'. You will then click on 'Save current display' and save a .png file. Click on 'Save Image' again and repeat the steps above, except click on 'Save Entire Image (1

pixel resolution)' and save as a .png. Repeat one more time and click on 'Save Entire Image (1 pixel resolution)' again except save as a .jpg.

11. Repeat above steps for each slide.

**Clean Up**

1. Make sure to remove your slides from the slide holder and shut down all software